Dissertation
submitted to the

Combined Faculty for the Natural Sciences and for Mathematics
of the Rupertus Carola University of Heidelberg, Germany

for the degree of

Doctor of Natural Sciences

presented by

MS in Physics: Béla Tuzson
born in Saint-George, Romania

Oral examination: 04.05.2005

Symmetry Specific Study of Ozone Isotopomer Formation

Referees: **P.D. Dr. Christof Janssen**

Prof. Dr. Ulrich Platt

Symmetriespezifische Untersuchung der Bildung von Ozonisotopomeren. Der ungewöhnliche Sauerstoffisotopeneffekt bei der Bildung des Ozonmoleküls ist 25 Jahre nach seiner Entdeckung noch immer nicht abschließend verstanden. Die experimentelle Datenlage, gerade bezüglich der Anwendung des schweren Sauerstoffs aus dem Ozon als eine atmosphärische Tracer-Substanz, ist gegenwärtig noch unbefriedigend. Mit der Weiterentwicklung eines hochauflösenden diodenlasergestützten Absorptions-Spektrometers, was im Wesentlichen den Einsatz einer goldbeschichteten astigmatischen Vielfachreflexionszelle und eines kalibrierten konfokalen Fabry-Perot Etalon umfasst, konnte eine wichtige Lücke im bestehenden Datensatz geschlossen werden. Alle atmosphärisch relevanten, d.h. die einfach ^{17}O oder ^{18}O substituierten Ozonmoleküle, konnten damit symmetriespezifisch aufgelöst werden. Dabei wurde nicht nur die Präzision in der Messung des Isotopengehalts von 0.3 % entscheidend verbessert, vielmehr wurden auch systematische Fehler früherer Messungen lokalisiert und eingegrenzt. Relativ zur Reaktion $^{16}O + {}^{16}O^{16}O \rightarrow {}^{16}O^{16}O^{16}O$ wurden damit die Ratenkoeffizienten der Reaktionskanäle $^{16}O + {}^{16}O^{17}O \rightarrow {}^{16}O^{16}O^{17}O$ und $^{16}O + {}^{17}O^{16}O \rightarrow {}^{16}O^{17}O^{16}O$ zum ersten Mal zu 1.292 ± 0.019 und 1.005 ± 0.010 sowie die der Kanäle $^{16}O + {}^{16}O^{18}O \rightarrow {}^{16}O^{16}O^{18}O$ und $^{16}O + {}^{18}O^{16}O \rightarrow {}^{16}O^{18}O^{16}O$ zu 1.426 ± 0.034 und 1.007 ± 0.013 bestimmt. Damit wird der direkte Zusammenhang zwischen Ozonbildungsgeschwindigkeit und der Reaktionsenthalpie der Isotopenaustauschreaktion bestätigt. Die Analyse einer Ozonprobe aus einer Laborsimulation zeigt weiterhin, daß der Isotopentransfer von Ozon in Kohlendioxid entgegen früheren Vermutungen zumindest unter Laborbedingungen keine Isotopenanomalie aufweist. Dies scheint den singulären Charakter des Ozonmoleküls zu bestätigen.

Symmetry Specific Study of Ozone Isotopomer Formation. The unusual isotope effect in the formation of the ozone molecule is not yet understood, even 25 years after its discovery. Furthermore, the experimental database is still unsatisfactory, particularly with regard to application of the heavy oxygen from ozone as an atmospheric tracer. To close a gap in the existing record, a high-resolution diode laser based absorption spectrometer was improved, essentially by the use of a gold-coated astigmatic mirror multipass cell and a calibrated confocal Fabry-Perot etalon. All atmospherically relevant, *i.e.* the simply ^{17}O or ^{18}O substituted ozone isotopomers could thereby be quantified. Precision in the measurement of the isotope abundance was improved to 0.3 %. Systematic errors in earlier investigations were identified and minimized in the present measurements. Relative to the reaction $^{16}O + {}^{16}O^{16}O \rightarrow {}^{16}O^{16}O^{16}O$, the rate coefficients of the channels $^{16}O + {}^{16}O^{17}O \rightarrow {}^{16}O^{16}O^{17}O$ and $^{16}O + {}^{17}O^{16}O \rightarrow {}^{16}O^{17}O^{16}O$ were determined to be 1.292 ± 0.019 and 1.005 ± 0.010, and those of the channels $^{16}O + {}^{16}O^{18}O \rightarrow {}^{16}O^{16}O^{18}O$ and $^{16}O + {}^{18}O^{16}O \rightarrow {}^{16}O^{18}O^{16}O$ were found to be 1.426 ± 0.034 and 1.007 ± 0.013. Thus, the direct connection between the rate of ozone formation and the enthalpy of the isotope exchange reaction is confirmed. Contrary to earlier assumptions, the analysis of a sample from a laboratory simulation further shows that the isotope transfer from ozone into carbon dioxide does not exhibit an isotope anomaly, at least under laboratory conditions. This apparently confirms the unique character of the ozone molecule.

"A theory is something nobody believes, except the person who made it. An experiment is something everybody believes, except the person who made it."

Albert Einstein

Contents

1. Introduction

1.1. Oxygen and Its Isotopes

Carbon, nitrogen, and oxygen, the "CNO elements", are among the most abundant species in the Universe. They are subsequently formed by p- and α-capture reactions in the interior of stars and partially released by means of stellar winds, planetary nebula ejecta, and supernova explosions into the interstellar medium [*Burbidge et al.*, 1957; *Woosley and Heger*, 2003].

It is commonly accepted that the various isotopes of an element require different nucleosynthetic processes, occurring under different conditions, on different time scales and in different parts of a star, so that stellar nucleosynthesis can produce isotopic heterogeneity. The abundant isotope, ^{16}O, is produced in stellar nucleosynthesis by helium burning, and is returned to the interstellar medium in supernova explosions. The rare stable isotopes, ^{17}O and ^{18}O, are produced by hot CNO cycles in zones rich in H and He, respectively, in both novae and supernovae [*Alexander and Nittler*, 1999; *Clayton*, 1993].

The relative isotopic abundances we observe in our solar system are established by a mixing of materials derived from a variety of sites [*Wasson*, 2000, and references therein]. The planetary materials and atmospheres derive from this reservoir of primordial solar system volatiles via physical and chemical processes. Thus, the present-day Earth atmosphere has some of the characteristics (chemical and isotopic composition) of the primordial source reservoir. In Table 1.1 the isotopic composition of oxygen in the terrestrial standard material, which is a mixture of distilled ocean waters referred to as VSMOW,[1] is shown.

Table 1.1.: The isotopic composition of the oxygen according to CAWIA[a]

Isotope	Atomic Mass (amu)	Representative isotopic composition	Available reference material
^{16}O	15.9949146223(25)	0.99757(16)	VSMOW
^{17}O	16.99913150(22)	0.00038(10)	
^{18}O	17.9991604(9)	0.00205(14)	

[a] Commission on Atomic Weights and Isotopic Abundances [*De Laeter et al.*, 2003].

[1] Vienna Standard Mean Ocean Water, distributed by IAEA (International Atomic Energy Agency) and NIST (National Institute of Standards and Technology)

Basic Concepts and Definitions

Molecules that differ in their isotopic composition have slightly different physical and chemical properties. This gives rise to the partitioning of isotopes (isotope fractionation) during physical or chemical processes, and these fractionations commonly are proportional to differences in the relevant isotope masses. Processes that differentiate on mass, yielding measurable changes in isotopic composition, include phase changes (*e.g.*, evaporation, condensation, crystallization, melting, and sublimation), ion exchange, sorption and desorption, diffusion and ultra-filtration. Chemical isotope-fractionation processes involve the redistribution of isotopes of an element among phases, molecules, or chemical species. On Earth, a variety of biological processes including photosynthesis, assimilation, respiration, and dissimilatory oxidation-reduction reactions contribute to isotopic fractionation.

Since natural variations in the isotopic compositions of the elements usually are small, the importance of an isotope fractionation is in its deviation from unity rather than in the fractionation factor itself. Thus, isotopic measurements of elements exhibiting isotope fractionation are given with respect to a δ(delta) scale defined by:

$$\delta = \frac{R_S}{R_{RM}} - 1 \tag{1.1}$$

where R_S and R_{RM}, refer to the isotope-abundance ratios of an element (e.g., $R = {}^{i}\mathrm{O}/{}^{16}\mathrm{O}$, where $i = 17$ or 18, respectively) in a sample, S, and a reference material, RM, respectively. Delta values are generally reported in parts per thousand, or per mill, and measured by comparing the apparent isotope-abundance ratio in a sample with that of a reference material measured under precisely the same conditions, without any attempt to determine the "absolute" isotope abundance ratios of either material. The fact that oxygen has three stable isotopes implies that two independent δ-values can be measured: $\delta^{18}\mathrm{O}$ and $\delta^{17}\mathrm{O}$, respectively.

Isotope fractionation can originate from both equilibrium effects and kinetic effects.

Equilibrium isotope fractionation results when the forward and backward reaction rates are the same between multiple coexisting phases or species with a common element. The equilibrium isotope fractionation factor (α) is given by:

$$\alpha_{a/b} = \frac{R_a}{R_b} \tag{1.2}$$

where a and b are two chemical species in isotopic equilibrium and R is the abundance ratio of two isotopes. The factor α is related to the thermodynamic equilibrium constant for the isotope exchange reaction between two isotopes of the element.

Kinetic isotope fractionations are normally associated with fast, incomplete, or unidirectional processes like evaporation, diffusion, dissociation reactions, and biologically mediated reactions. For kinetic fractionations, the fractionation factor can be expressed as the ratio of the reaction rates of the two isotopically different molecules undergoing the reaction: $\alpha_{kin} = k_i/k_j$ where k_i and k_j refer to the reaction rates

of molecules containing the heavier and lighter isotopes of the element in question. The rate of a reaction can be modified by isotopic substitution in a variety of ways. In the case of a dissociation reaction, the rate difference can be rationalized by noting that the mass of an atom affects the vibrational frequencies of the molecule, even if the electron configuration is identical. Heavier atoms will lead to lower vibrational frequencies, and viewed quantum mechanically, thus to a lower zero-point energy. With a lower zero-point energy, more energy must be supplied to break the bond, resulting in a higher activation energy for bond cleavage, which in turn lowers the measured rate.

The magnitude of equilibrium isotope fractionation depends in part on state variables, temperature being the most important, whereas the magnitude of kinetic fractionation commonly varies with the overall reaction rate and mechanism. For almost all of the previously discussed fractionation processes the partitioning of isotopes is governed by the relative mass differences, such that

$$\left(\frac{^{17}\mathrm{O}}{^{16}\mathrm{O}}\right)_S \Big/ \left(\frac{^{17}\mathrm{O}}{^{16}\mathrm{O}}\right)_{RM} = \left\{\left(\frac{^{18}\mathrm{O}}{^{16}\mathrm{O}}\right)_S \Big/ \left(\frac{^{18}\mathrm{O}}{^{16}\mathrm{O}}\right)_{RM}\right\}^n \tag{1.3}$$

where S and RM refer to the sample and reference material, respectively.[1] The exponent n is approximately equal to the ratio of the relative mass differences, *i.e.*,

$$n = [m(^{16}\mathrm{O})^{-1} - m(^{17}\mathrm{O})^{-1}]/[m(^{16}\mathrm{O})^{-1} - m(^{18}\mathrm{O})^{-1}] \simeq 0.5281 \tag{1.4}$$

though it may differ slightly for different materials and processes.[2] The exact value of n depends on the process involved ($n \in [0.50, 0.53]$). It should further be mentioned that virtually all terrestrial rock samples have a very restricted oxygen-isotopic composition in that they fall on one particular mass-fractionation line, which is known as the terrestrial fractionation line (TFL).[3]

1.2. The Ozone Isotope Effect

In the previous section it was pointed out that variations in the isotopic compositions of terrestrial samples arise from mass-dependent differences in the rates and equilibria of chemical and physical processes operating on Earth. Chemical isotope effects, whether kinetic or equilibrium, are on the order of few percent at most and show an almost linear proportionality to the relative mass difference of the isotopes, $\Delta m/m$. However, recent investigations[4] of isotopic processes in atmospheric trace gases, lead to the recognition that few reactions among atmospheric compounds can cause isotope

[1] For small isotope effects this lead to a linear correlation: $\delta^{17}\mathrm{O} = n\,\delta^{18}\mathrm{O}$.

[2] Actually the mass fractionation law differs for equilibrium and kinetic processes because kinetic fractionation results from motions that can often be described classically using effective masses whereas equilibrium exchange is purely a quantum phenomenon that depends on the atomic masses alone. [*Young et al.*, 2002]

[3] When plotted on a 3-isotope plot ($\delta^{17}\mathrm{O}$ versus $\delta^{18}\mathrm{O}$), a line with a slope of ca. 0.52 is observed.

[4] For an extensive review see *Brenninkmeijer et al.* [2003] and references therein.

fractionation which cannot be approximated by the mass-dependent fractionation equation and is very large. For example, ozone (O_3) and stratospheric carbon dioxide (CO_2) exhibit variations in the relative abundances of ^{16}O, ^{17}O, and ^{18}O in which the exponent n is significantly larger than 1/2. The cause of this unusual oxygen isotope effect in the atmosphere is still subject of debate. As we will see later, the gas-phase reaction that leads to the formation of the ozone molecule shows a large and unique kinetic isotope effect. Most likely this isotope signature can be transferred into other atmospheric species via bimolecular collisions with O_3 or isotopic exchange reactions with excited O atoms generated in photodissociation of O_3.

The purpose of this section is to provide some background information on the anomalous ozone isotope effect. The reader should not expect to find a complete overview of the literature regarding this topic, since there are almost 25 years of measurements (in the atmosphere as well as in the laboratory) and theoretical investigations. For detailed overviews see the reviews by *Mauersberger et al.* [2003]; *Thiemens* [1999] and *Weston* [1999].

This section is organized as follows: First, a brief review of the atmospheric ozone measurements is given, followed by the description of benchmark laboratory experiments that provided some insights into the mechanism of the unusual isotopic effect. Then, various proposed theoretical explanations for the observed effects are discussed. Finally, a summarizing section including the motivation of the thesis closes the chapter.

1.2.1. Ozone in the Atmosphere

The ozone molecule in the atmosphere is naturally formed in chemical reactions involving UV solar radiation ($\lambda \leq 240\,\text{nm}$) and oxygen molecules. In the stratosphere ozone forms a layer where more than 90 % of Earth's ozone resides. Despite its relatively low abundance, the ozone molecule (up to 10 ppm around 25 km) serves as an effective shield (for radiation with wavelengths between 240 and 320 nm) against biologically harmful solar UV radiations. Moreover, because O_3 also absorbs radiation in the visible and infrared region, atmospheric O_3 significantly affects the Earth's energy budget and temperature. Finally, the photolysis of O_3 initiates much of stratospheric chemistry and plays a controlling role in tropospheric oxidation processes.

Due to the fact that the photodissociation of O_2 is the dominant source of upper atmospheric O_3, efforts to understand the oxygen photolysis started as soon as the spectroscopic data became available. A first estimation of the photodissociation rate of the second most abundant isotopic form of O_2, the $^{16}O^{18}O$, together with a study of its significance as an odd-oxygen source was given by *Cicerone and McCrumb* [1980]. Based on a preferential dissociation of $^{34}O_2$ in the upper atmosphere, the possibility of isotope enrichment in heavy ozone ($^{50}O_3$) was mentioned. One year later, an *in-situ* balloon borne mass spectrometric measurement, revealed an unexpected enhancement of the $^{50}O_3$ isotopologue near 32 km [*Mauersberger*, 1981]. Additional measurements in 1987 showed that levels of $^{49}O_3$ were likewise increased above the statistically expectation almost as much as for $^{50}O_3$ [*Mauersberger*, 1987].

Interestingly, an extensive theoretical analysis of isotopically specific photochemistry of ozone in the stratosphere pointed out that O atom exchange reactions

$$^{18}O + {}^{16}O{}^{16}O \rightleftharpoons {}^{18}O{}^{16}O + {}^{16}O \tag{1.5}$$

should be sufficiently fast in the upper atmosphere that any additional ^{18}O produced by the preferential photolysis of $^{34}O_2$ would be redistributed and the $^{18}O/^{16}O$ ratio would be determined by the equilibrium constant for the exchange reactions [*Kaye and Strobel*, 1983]. Moreover, detailed calculations [*Blake et al.*, 1984; *Omidvar and Frederick*, 1987] of the absorption cross-section in the Schumann-Runge bands resulted in a production rate of ^{18}O an order of magnitude less than originally proposed by *Cicerone and McCrumb*, and thus eliminated an enhancement of ^{18}O as the source of heavy ozone.

Also spectroscopic remote sensing seemed nevertheless to support the mass spectrometer measurements of heavy ozone, although with large uncertainty in the measurements [*Abbas et al.*, 1987; *Rinsland et al.*, 1985]. In the following years several stratospheric ozone measurements including balloon-borne cryogenic collector system combined with mass spectrometer measurements [*Schueler et al.*, 1990] and various techniques of infrared remote sensing (ground-based or balloon-borne as well as spaceborne spectrometers) were employed [*Goldman et al.*, 1989; *Irion et al.*, 1996; *Johnson et al.*, 2000; *Meier and Notholt*, 1996].

Most recently, stratospheric ozone samples collected with a cryogenic collector system during four balloon flights were analyzed in laboratory with a mass spectrometer [*Krankowsky et al.*, 2000]. In an altitude range between 22 and 33 km all ratios show enrichments, which range from 7 to 9 % for $^{49}O_3$ and from 7 to 11 % for $^{50}O_3$. The most recent remote sensing experiments (enrichments $\sim$ 14 %) are in agreement with the mass spectrometer measurements. Finally, measurements of tropospheric ozone [*Johnston and Thiemens*, 1997; *Krankowsky et al.*, 1995] revealed that the ozone isotope effect is also present in tropospheric ozone. Average values of $\delta^{17}O$ = 6.6 - 7.8 % and $\delta^{18}O$ = 8.2 - 9.1 % were reported.

1.2.2. Laboratory Investigations

The discovery of unusually high enrichments in stratospheric ozone has resulted in an extensive effort to simulate and understand the effect under controlled laboratory conditions. The chemically produced anomalous ozone isotope fractionation was discovered in a simple experiment by generating ozone in an electric discharge [*Thiemens and Heidenreich*, 1983]. The degree of fractionation for ^{17}O did not obey the mass-dependent fractionation rule. Rather it was found that $\delta^{17}O \approx \delta^{18}O$. In a follow-up experiment it is shown that at very low oxygen pressures ($<$ 3 Torr) the ozone is depleted both in ^{17}O and ^{18}O and showed deviations from the 1:1 correlation [*Heidenreich and Thiemens*, 1986]. After these findings a series of other experiments followed [*Bains-Sahota and Thiemens*, 1987; *Bhattacharya and Thiemens*, 1988; *Thiemens and Jackson*, 1987, 1988, 1990; *Wen and Thiemens*, 1990], and the ozone isotope ratios have been studied at a variety of temperatures and pressures. Ozone has been

generated in these experiments using high-frequency electric discharge, microwave discharge (static and flow reactors) and UV photolysis of O_2. These experiments led to the suggestion that the observed isotopic fractionation derives from the symmetry of the different isotopomeric[1] species. Thus, the isotopic fractionation would not derive from a property of mass, but rather symmetry, *i.e.* the location of the heavy atom within the ozone molecule.

The first experimental check of the role of molecular symmetry in the isotopic fractionation of ozone was performed by *Morton et al.* [1989], followed by *Mauersberger et al.* [1993], using statistically mixed (scrambled via isotopic exchange reactions) enriched O_2 gas to form different ozone isotopologues in the mass range 48 through 54. The products were measured directly using a molecular beam mass spectrometer. The results of this experiment were consistent with a symmetry dependent fractionation mechanism, although it proved that the formation mechanism is not just a simple symmetry effect. Purely symmetric molecules ($^{17}O^{17}O^{17}O$ and $^{18}O^{18}O^{18}O$) appeared to be formed according to the conventional theory [*Kaye and Strobel*, 1983], while the molecular combination of mass 51 that contains only asymmetric molecules showed the highest enrichment and thus the largest isotope effect. Interestingly both $^{49}O_3$ and $^{50}O_3$ had about the same enhancements of 11 and 13 % respectively, even when produced in highly enriched mixtures. Thus, the ozone isotope effect does not depend on the isotope composition of the O_2 gas. It is an intrinsic molecular effect.

In a novel experiment reported by *Morton et al.* [1990], ozone was formed from O and O_2 in their electronic ground-states by visible light photolysis. The major goal of this experiment was the investigation of the temperature and pressure dependence of the isotope ratios produced in the gas phase $O(^3P) + O_2(^3\Sigma_g^-)$ recombination reaction. Interestingly, the recombination reaction alone produces the large, anomalous isotope effect, without excited states being involved. Thus, the effect must be attributed to the elementary kinetic process of ozone formation. At a constant oxygen pressure of 50 Torr, the δ values increased from 3.6 % for ^{17}O and 2.6 % for ^{18}O at 130 K to 11.7 % and 14.6 % at 361 K. The pressure dependence has been characterized at 321 K between 5 and 1000 Torr. Enrichment values of $\delta^{17}O = 7.5\,\%$ and $\delta^{18}O = 7.9\,\%$ have been found at 1000 Torr. These data sets are a useful reference for atmospheric and laboratory studies, because the physical parameters like temperature and pressure are well characterized.

In an experiment designed to investigate the pressure dependency of the ^{18}O enrichment at even higher pressures, *Thiemens and Jackson* [1990] demonstrate that the enrichment decreases in the 8 to 45 bar region by 8.4 % and is absent at $\sim$ 56 bar. This clearly demonstrates that the behavior of the ^{18}O enrichment in ozone formation does not coherently follow the observed kinetic falloff curves [*Hippler et al.*, 1990; *Morton et al.*, 1990]. Therefore, it is unlikely that theories involving differential lifetimes of the metastable state are the source of the observed mass independent fractionations.

[1] Following IUPAC recommendations, *isotopologues* are molecular entities that differ in isotopic composition, whereas *isotopomers* designate isomers which have the same number of each isotopic atom but differ in their intramolecular position.

Ozone isotope research progressed from two heavy isotopologues in natural oxygen to a detailed study of all molecular combinations. Their isotopic fractionation is shown in Figure 1.1. These enrichments or depletions represent final products with contributions from different specific ozone formation channels. It was recognized that the rate coefficients for individual ozone formation channels would provide important information about processes that may control the observed ozone fractionations [*Sehested et al.*, 1995].

The first experiment investigating individual reaction channels led to the discovery of the kinetic origin of the isotope effect in ozone formation [*Anderson et al.*, 1997]. The rate coefficients of the following four ozone formation channels were measured:

$$^{16}O + {}^{16}O^{16}O + M \rightarrow {}^{16}O^{16}O^{16}O + M \tag{1.6}$$

$$^{18}O + {}^{16}O^{16}O + M \rightarrow {}^{18}O^{16}O^{16}O + M \tag{1.7}$$

$$^{16}O + {}^{18}O^{18}O + M \rightarrow {}^{16}O^{18}O^{18}O + M \tag{1.8}$$

$$^{18}O + {}^{18}O^{18}O + M \rightarrow {}^{18}O^{18}O^{18}O + M \tag{1.9}$$

Reaction (1.7) and (1.8) mainly produce asymmetric ozone molecules (with the colliding atom becoming the end member of the ozone molecule), while reaction (1.6) and (1.9) will form symmetric molecules. Thus, if symmetry would play the dominant role in the isotope enrichment process, then one should expect similar (or even equal) rate coefficients for these reaction pairs. However, the experiment showed that reaction (1.7) had a rate coefficient of 0.92, while reaction (1.8) had a rate coefficient of 1.53 when compared to the rate of the standard reaction (1.6). The conclusion is that the formation of asymmetric ozone molecules does not guarantee a rate coefficient advantage over the reaction (1.6).

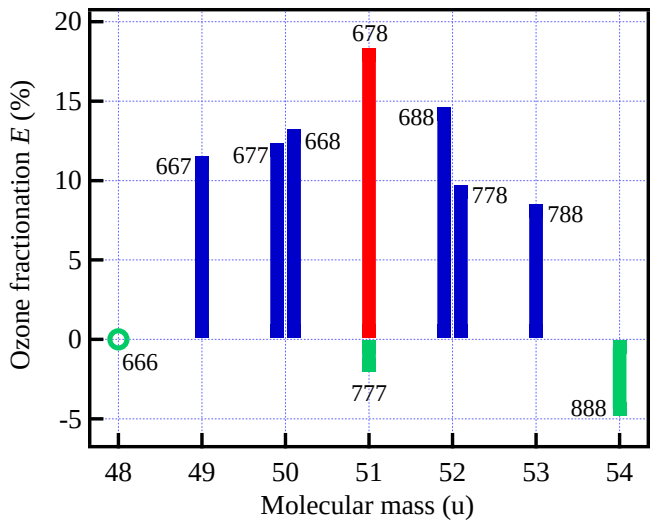

Figure 1.1.: Measured enrichment or depletion of all possible ozone isotopologues adapted from *Mauersberger et al.* [1993]. The labels 6, 7 and 8 stand for ^{16}O, ^{17}O and ^{18}O, respectively. Ozone was produced in two isotopically enriched oxygen mixtures of well-known composition at 70 Torr and room temperature. The statistical abundance of each isotopologue was calculated and used to derive from the measured values the isotopic fractionation. The values in the graph are normalized so that $^{48}O_3$ has zero enrichment.

In follow up laboratory investigations the number of formation rates has been expanded considerably and all rates with homonuclear oxygen molecules were determined [*Mauersberger et al.*, 1999]. Some crucial coefficients, however, were still

missing: those which involve the ozone formation with heteronuclear molecular oxygen. *Janssen et al.* [1999] developed a tunable diode laser experiment in combination with mass spectrometer analysis to measure the missing relative rates for the ^{16}O-^{18}O system. The spectroscopic method allowed symmetry-specific detection of ozone molecules. In particular the branching ratios of the $^{16}O + {}^{16}O^{18}O$ reaction (see Table 1.2), which leads to two different product channels, could be determined. Furthermore, the assumption that the ozone formation reaction is exclusively end-on was verified by quantitative analysis of symmetric molecules resulting from a reaction like $^{18}O + {}^{16}O^{16}O$.

Table 1.2.: Summary of previously obtained data [*Janssen et al.*, 1999; *Mauersberger et al.*, 1999], including measured isotopologue enrichment as well as measured and derived rate coefficients of $^{49}O_3$ and $^{50}O_3$ produced in ^{16}O-^{17}O and ^{16}O-^{18}O mixtures, respectively.

Molecular mass	Enrichment[a] (%)	Relative rate coefficient[b] Reaction		Value
48	0.0	(R1)	$^{16}O + {}^{16}O^{16}O \longrightarrow {}^{16}O^{16}O^{16}O$	1.00
49	11.3	(R2a)	$^{17}O + {}^{16}O^{16}O \longrightarrow {}^{16}O^{17}O^{16}O$	1.03[c]
		(R2b)	$^{17}O + {}^{16}O^{16}O \longrightarrow {}^{17}O^{16}O^{16}O$	
		(R2c)	$^{16}O + {}^{16}O^{17}O \longrightarrow {}^{16}O^{16}O^{17}O$	1.17[d]
		(R2d)	$^{16}O + {}^{17}O^{16}O \longrightarrow {}^{16}O^{17}O^{16}O$	
50	13.0	(R3a)	$^{18}O + {}^{16}O^{16}O \longrightarrow {}^{16}O^{18}O^{16}O$	0.006
		(R3b)	$^{18}O + {}^{16}O^{16}O \longrightarrow {}^{18}O^{16}O^{16}O$	0.92
		(R3c)	$^{16}O + {}^{16}O^{18}O \longrightarrow {}^{16}O^{16}O^{18}O$	1.45
		(R3d)	$^{16}O + {}^{18}O^{16}O \longrightarrow {}^{16}O^{18}O^{16}O$	1.08

For reactions involving heteronuclear oxygen molecules the relative reaction probability is shown while relative rate coefficients are obtained by dividing the quoted numbers by two.

[a] Values at $\approx 320\,\mathrm{K}$

[b] The rate coefficients are relative to the standard rate for $^{16}O + {}^{16}O^{16}O + M$ of $6 \times 10^{-34}\,\mathrm{cm^6 s^{-1}}$ [*Anderson et al.*, 1997].

[c] This rate may contain small contribution from the subsequent symmetric molecules.

[d] Derived rate coefficient representing the sum of two reaction channels that result in symmetric and asymmetric molecules, respectively.

The discovery of the high variability in the rate coefficients required additional studies regarding their pressure and temperature dependence. For two reactions, (1.7) and (1.8), the pressure dependence of the relative rate coefficients and its third body dependence has been experimentally investigated [*Günther et al.*, 1999, 2000]. While the rate coefficient for reaction (1.8) compared to reaction (1.6) decreases as the total pressure increases, the rate coefficient of reaction (1.7) compared to reaction (1.9) remains unchanged. Whereas absolute rate coefficients for ozone differ by a factor of four between Ar and CO_2 as third-body, the relative rate coefficients remain the same. *Janssen et al.* [2003] determined over a large temperature range the change of rate coefficients of the ^{16}O-^{18}O system. The temperature dependence of the four isotopologues $^{48}O_3$, $^{50}O_3$, $^{52}O_3$ and $^{54}O_3$ was studied, too. The fractionation of the $^{54}O_3$ isotopologue could be explained entirely with the change in the $^{16}O/^{18}O$

atom density in the gas. Large formation rate coefficient ratios of 1.5 like (1.8) *vs.* (1.6) show no temperature dependence while small ratios such as (1.7) *vs.* (1.6) with a value of 0.92 decrease with decreasing temperatures. Temperature-related changes of isotopologue fractionation values for $^{50}O_3$ and $^{52}O_3$ were explained in terms of changes in rate coefficient ratios and contributions from isotope exchange reactions.

1.2.3. Theoretical Approaches

The first models [*Bates*, 1986, 1988, 1990; *Gellene*, 1996; *Valentini*, 1987] to explain the anomalous isotope effect in ozone appeared shortly after the discovery of the enrichments of the heavy ozone isotopologues. However, they were made before the relative rate coefficients for the ozone formation became available. New laboratory measurements, showed the deficiencies of these early explanations, therefore, they will be not discussed here.

By now it has been experimentally established that collisions to form ozone are end-on reactions, and that molecular symmetry plays no apparent role in the ozone isotope enrichment process, regardless on whether or not ozone is produced in collisions with homo- or heteronuclear molecular oxygen. There is also some evidence that the energy transfer mechanism is more appropriate to depict the termolecular association reaction with respect to its isotope effect [*Günther et al.*, 2000]. This is mainly due to the fact that the interaction potential between reactants is much more crucial than the one between the reactants and the third body.

Within the energy transfer (Lindemann-Hinshelwood) mechanism, the ozone formation is divided into two consecutive bimolecular steps

$$O + O_2 \rightleftharpoons O_3^* \tag{1.10}$$

$$O_3^* + M \rightarrow O_3 + M \tag{1.11}$$

where O_3^* is a metastable complex. The first step (1.10) describes the bimolecular association together with the reverse unimolecular redissociation reactions. The second step (1.11) depicts the stabilization or deactivation process in which the vibrationally excited molecule O_3^*, by collision with an inert molecule M, is stabilized into ozone through energy transfer. In order to calculate the reaction rate via (1.10) and (1.11) one first must know the energies, lifetimes and rates of formation and dissociation of the metastable O_3^* states. Secondly, one has to know the rates of the stabilization step (1.11) for different metastable states and isotopic combinations. Therefore, knowledge about the dynamics of ozone near its dissociation threshold is a requirement. Dynamics calculations, in turn, necessitate a realistic and global potential energy surface (PES). A quantitative theoretical treatment has also to start from a three-dimensional potential energy surface for the ground electronic state of O_3 ($\tilde{X}^1A_1$). This PES must describe the three[1] equivalent O_3 potential wells and the three $O(^3P) + O_2(^3\Sigma_g^-)$ asymptotic channels.[2]

[1] Due to nuclear permutation symmetry, there exist three such equivalent potential minima.

[2] An excited XYZ^* molecule may decompose into several product channels, such as $XY + Z$, $X + YZ$, and $Y + XZ$.

Many authors [*Müller et al.*, 1998; *Tyuterev et al.*, 1999; *Xie et al.*, 2000; *Yamashita et al.*, 1992] have investigated the electronic structure of the low-lying states of ozone, but until recently there was only one global PES [*Yamashita et al.*, 1992], which has been calculated by *ab initio* methods. A very precise PES has been constructed by *Tyuterev et al.* [1999] by fitting experimental transition energies up to 5800 cm^{-1} above the ground vibrational level. However, the part of the PES which is most essential to kinetic studies is not reliably described by this potential.

With argon as a buffer gas, a quasi-classical trajectory study of the ozone formation process and its isotope dependence has been performed by *Gross and Billing* [1997]. The energy-transfer mechanism was simulated on a modified *ab initio* ground-state PES calculated by *Yamashita et al.* [1992]. The calculated O_3 formation rates showed only a marginal dependence on the isotope composition.

Based on the RRKM theory, an extensive treatment of the isotope effect in ozone has been performed. [*Gao and Marcus*, 2001, 2002; *Gao et al.*, 2002; *Hathorn and Marcus*, 1999, 2000]. The exchange reaction rate coefficient and relative formation rate coefficients for the 15 known rates were calculated and other rates were predicted. The pressure dependent absolute formation rate coefficient and enrichment factors were also derived. In the RRKM treatment there are two parameters, in addition to those used to adjust the PESs, the ΔE and η which were tuned properly to reproduce the experimental data for the two extreme cases: 0.92 for reaction (1.7) and 1.53 for reaction (1.8). The first parameter enters in the description of the stabilization process and it was set to 210 cm^{-1}. It represents the average energy transfer per collision. With the second parameter (a non-statistical factor) η = 1.18, the densities of states of the symmetric molecules XYX are lowered and thus their relative formation rates are reduced. They demonstrated that this η-effect is dominant in determining the anomalous mass-independent isotope enrichments in stratospheric conditions. However, these factors are empirical parameters that do not follow from the theory and especially the first one does not agree with other studies [*Babikov et al.*, 2003b; *Baker and Gellene*, 2002; *Ivanov et al.*, 2004] . The authors have also recognized that rigorous detailed quantum mechanical calculations for various isotopologues of ozone are needed in order to accurately describe the isotope effects.

About the same time, *Janssen et al.* [1999] found that the formation rates for different isotopic compositions of ozone do not correlate with the masses of the oxygen atoms involved, but with the difference in the zero-point energies (ΔZPE) of the two possible fragment channels to which O_3, excited above its threshold, can dissociate.

$$X + YZ \rightleftharpoons (XYZ)^* \rightleftharpoons XY + Z \tag{1.12}$$

Here, the metastable state $(XYZ)^*$ can be formed from both sides of this reaction and can decay either to the right or left. Reaction (1.10) is part of this reaction. When different isotopes of oxygen (X, Y, and Z) are involved, the ZPE of the O_2 molecules on the right- and left-hand sides may be different, and reaction (1.5) can thus be slightly exothermic or endothermic. The correlation between the relative rate coefficients of the asymmetric molecules and the zero-point energy change of the

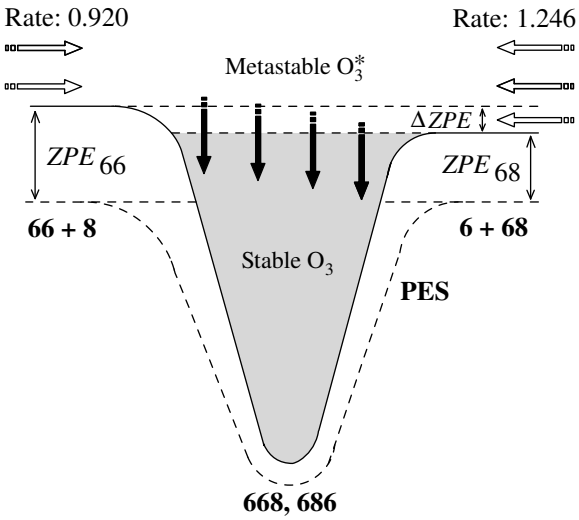

Figure 1.2.: Principle energetics of isotope exchange and ozone formation. The PES (dotted line), the ZPE for two channels, and the ΔZPE are shown (not to scale). Stable ozone molecules are formed in the 1 eV potential well (shaded part) as a result of collisional stabilization with inert bath gas molecules M. Metastable states above the ΔZPE energy ($\sim 23\,\mathrm{cm}^{-1}$) can be formed from both entrance channels: $^{18}O + {}^{16}O_2$ or $^{16}O^{18}O + {}^{16}O$, while in the ΔZPE part of spectrum are formed exclusively from the $^{16}O^{18}O + {}^{16}O$ entrance channel. Experimental relative rates of ozone formation for the two channels are given at the top. Figure adopted from *Babikov et al.* [2003b].

O_2 molecule in the corresponding atom exchange reaction is approximately linear. This suggests that large rate coefficients are associated with endothermic exchange processes and the small ones with exothermic exchange reactions.

Most recently, *Schinke and co-workers* in a series of theoretical studies presented an accurate and global PES for the electronic ground-state of ozone [*Siebert et al.*, 2001, 2002], revisited the exchange reaction using classical trajectories [*Fleurat-Lessard et al.*, 2003] and performed the first full quantum mechanical calculations of the O_3^* ro-vibrational resonances for several ozone isotopologues based on the new PES [*Babikov et al.*, 2003a,b]. The calculations reveal an increased number of long-lived metastable vibrational states of ozone just at the dissociation threshold of asymmetric ozone species. The increased number of scattering resonances is attributed to the ZPE differences (see Figure 1.2) of the possible dissociation pathways of the asymmetric molecule. It is further suggested that the energy transfer could be symmetry-selective. It was quantitatively shown that this feature of metastable states is responsible for the anomalous isotope effect in ozone formation. The direction of the isotope effect and its order of magnitude are obtained correctly; the absolute value of the effect obtained for $J = 0$ is about a factor of 2 larger than experimental. For $J > 0$, which was not calculated, however, centrifugal barriers appear that are expected to prevent population of resonances in the ΔZPE part of the spectrum, because tunnelling of oxygen through the barrier is slow. In order to make a quantitative comparison between experiment and theory, however, the lifetimes have to be used in a kinetic model for the recombination of ozone including thermal averaging over energy and rotational state. This work too has to be performed.

The further development of these different theoretical approaches may finally lead to a complete understanding of the ozone isotope effect. The effect may then be identified either as a general model case for other molecular systems, or as being in fact exotic and peculiar.

1.3. Motivation of the Thesis

In summarizing the previous sections, considerable progress has been made in unravelling the complexity of the ozone isotope effect. Laboratory studies have shown that an important aspect of the ozone isotope anomaly is its dependence on pressure and temperature of the gas in which ozone is formed. The temperature dependent isotope exchange reactions also contribute to the observed isotope enrichments in ozone. They determine the relative abundance of O atoms with ^{17}O and ^{18}O being always lower than statistically expected. The observed independence of the ozone isotope effect on the third-body supports that the O – O_2 interaction is important rather than interaction between one of the reactants and the third body. Hence, the isotope selectivity in ozone formation arises primarily from the transfer of the excess kinetic energy of the relative motion into the O_2 vibration which produces a vibrationally excited O_3^*, and not from the subsequent collisional deactivation and stabilization through the bath gas. Furthermore, the observed enhancements do not depend on the isotopic composition of the oxygen gas in which ozone is formed. This clearly demonstrates that the isotope anomaly in the ozone formation is an intrinsic kinetic feature, not covered by equilibrium thermodynamics. Therefore, a kinetic description of the ozone isotope effect is required. Additionally, the enrichments (depletions) in the different ozone isotopologues measured with mass-spectrometer represent final products with contributions from isotope exchange reactions and particularly from different specific ozone formation channels. These enrichments can now be traced to specific reaction channels. The large variability of isotope-specific coefficients of the ozone formation reactions proves the fact that symmetry cannot be the driving factor in the search for a fundamental explanation of the ozone isotope anomaly. Instead, the difference of the zero-point energies, ΔZPE, of the fragmentation channels of O_3 are of substantial importance. This concept is supported also by quantum mechanical calculations, which lead to the discovery of a strong nonstatistical feature of O_3^* lifetime spectrum. This resonance spectrum is explained by the difference in ZPE of two formation/dissociation channels. Qualitatively this feature is responsible for the anomalous rates of ozone formation.

Although, the substantial number of known relative rate coefficients, which has grown up to 15, allows to draw a consistent picture about the origin of the isotope effect in ozone, the knowledge of further rate coefficient values would provide a solid basis for the above mentioned concept. For example, though the overall rates for the different reaction channels leading to the formation of $^{49}O_3$ isotopologue are known, the partitioning in symmetric or asymmetric molecules on the product side of the reactions is not. Furthermore, the knowledge of the symmetry specific enrichments in $^{16}O_2{}^{17}O$ and $^{16}O_2{}^{18}O$ has immediate application in the atmosphere, because it provides a starting point for understanding the transfer mechanisms of the anomalous isotope signature to other atmospheric species.

At the moment, there is only a single study of rate coefficients for the reactions involving heteronuclear oxygen molecules [*Janssen et al.*, 1999]. The ozone samples in this study were generated by an electric discharge in O_2. Unfortunately, the chemistry in an electric discharge is complex due to the presence of excited electronic states as

well as ionized and metastable species. The increased number of side reactions, that lead to secondary chemistry, obviously adds unwanted complication to the ozone reaction kinetics. Furthermore, the temperature where the ozone is formed is not well defined. These short-comings motivate a new analysis, in which the experimental parameters are more adequately controlled.

Furthermore, there are still open questions in experimental ozone isotope research. An additional isotope effect, though much smaller than that in ozone formation, has been identified in UV and visible light dissociation of ozone [*Chakraborty and Bhattacharya*, 2003; *Wen and Thiemens*, 1991]. Given the scarcity of experimental data, the knowledge of the effect in photoinduced dissociation of ozone is presently inadequate.

The main goals of the present thesis can be summarized as follows:

- Develop and improve a technique to assure simultaneous and symmetry selective detection of $^{49}O_3$ and $^{50}O_3$ isotopologues.
- Set up an experiment in which the ozone gas formation reaction can be investigated under well defined conditions, and where the influence of secondary isotopic effects and side reactions can be quantified.
- Apply the technique to investigate isotope transfer mechanisms relevant in the atmosphere.

2. Infrared Laser Absorption Spectroscopy

Most molecules exhibit characteristic ro-vibrational transitions in the infrared (IR), which are influenced by isotopic substitution. The frequency shift [*Herzberg*, 1991] in the molecular ro-vibrational spectra due to isotopic substitution serves as the basis of isotopic analysis. Laser absorption spectroscopy [*Demtröder*, 1996; *Mantz*, 1995; *Werle*, 1996, 1998; *Werle et al.*, 2002] already has demonstrated the high sensitivity needed for such isotopic measurements [*Kerstel et al.*, 2002; *McManus et al.*, 2002; *Uehara et al.*, 2001, 2003; *Yamamoto and Yoshida*, 2002]. The use of tunable diode lasers is particularly attractive, because their high spectral resolution allows to isolate spectral features for each isotopomer of interest.

In this chapter the theoretical background of ro-vibrational laser absorption spectroscopy is briefly presented. First, the general spectroscopic properties of the ozone molecule are reviewed. Then the basis of the direct absorption technique, including discussions about the origin of the spectral absorption features and their dependence on different physical parameters, like temperature and broadening mechanisms is considered. A short description of the methodology used for isotopic fractionation analysis as well as the line selection procedure will be given in the last section of this chapter.

2.1. IR Spectroscopy of the Ozone Molecule

The ozone molecule, composed from three oxygen atoms, in its electronic ground state[1] has an open isosceles triangular geometry with apex angle $\alpha_e = 116.7542\,^\circ$ and two equal bonds with a length of $r_e = 1.27173$ Å [*Bacis et al.*, 1998; *Tanaka and Morino*, 1970]. The three normal modes of vibration ($\nu_1\nu_2\nu_3$) are all IR active.

The combination of the three stable oxygen isotopes – ^{16}O, ^{17}O, and ^{18}O – permits the formation of a large variety of ozone isotopologues from mass 48 through 54. Furthermore, for a given combination of oxygen isotopes, there may be two (*e.g.*, $^{16}O^{18}O^{16}O$ and $^{16}O^{16}O^{18}O$) or even three (*e.g.*, $^{16}O^{17}O^{18}O$, $^{17}O^{16}O^{18}O$ and $^{16}O^{18}O^{17}O$) isotopomers depending on whether a given isotope is in the apex or in the end position of the open isosceles triangle. Symmetric species ($^{16}O_3$, $^{16}O^{18}O^{16}O$,

[1] The ground state of ozone can be viewed, to a good approximation, as two single O-O bonds plus two π- electrons, one near each terminal atom, which are singlet-coupled together. To obtain such a description, one must go beyond the Hartree-Fock level. Indeed, the generalized valence-bond (GVB) description of ozone was an early example showing the importance of electron correlation beyond the Hartree-Fock approximation [*Hay et al.*, 1975].

$^{16}O^{17}O^{16}O$, ...) of the ozone molecule belong to the C_{2v} point group, while the asymmetric species ($^{16}O^{16}O^{18}O$, $^{16}O^{16}O^{17}O$, ...) belong to the C_s point group. The molecular axes and symmetry elements of ozone in its electronic ground state for the C_{2v} point group are schematically shown in Figure 2.1.

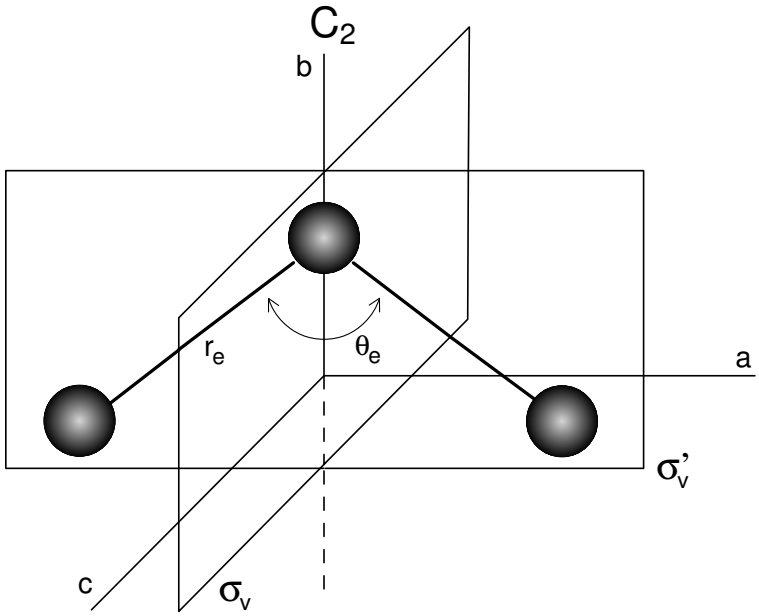

Figure 2.1.: The molecular axes and symmetry elements of O_3 in the electronic ground state. The axis labelling corresponds to that commonly used for a prolate symmetric top, where a is the axis of smallest moment of inertia.

An asymmetric rotor can exhibit three types of pure rotational transitions if the molecule has nonzero components of the electric dipole moment in the direction of the a, b and c principal axes. Since triatomic molecules are planar, the ozone molecule's dipole moment components can only occur in the a- and b-axis directions. The energy level formulation for a rigid asymmetric top is considerably more complex than that of symmetric-tops (see Eq.(2.3)) or linear molecules. With the exception of low rotational levels, the rotational energy and transitions cannot be conveniently expressed in simple algebraic terms.

A ro-vibrational energy level of the ozone molecule is characterized by a set of three rotational quantum numbers (JK_aK_c) with K_a and K_c taking all values 0, 1, ..., which are subject to the conditions $K_a \leq J, K_c \leq J$ and $K_a + K_c = J$ or $J + 1$ [*Flaud and Bacis*, 1998]. There are thus $2J + 1$ levels of a given J (each again with a rotational weight of $2J+1$). In addition, one has to consider the symmetry of the total wavefunction, which has to be symmetrical or antisymmetrical with respect to the exchange of the two identical nuclei depending on their nuclear spin I. The numbers of symmetrical and antisymmetrical spin functions are $(2I + 1)(I + 1)$ and $(2I + 1)I$, respectively. An important point to remember is that the nuclear spin for ^{16}O and ^{18}O is 0, so only the symmetrical levels of ozone species such as $^{16}O_3$, $^{16}O^{18}O^{16}O$, $^{18}O^{16}O^{18}O$, etc. will be populated. For the ^{17}O containing ozone isotopologue the

situation is different, because ^{17}O has a nuclear spin of 5/2. This will cause a nuclear spin degeneracy of 15 and 21, respectively. For the asymmetrical species all the levels are populated with the same nuclear spin statistical weight.

The general spacing of the rotational levels is governed by the parameter

$$\kappa = \frac{2B - A - C}{A - C} \tag{2.1}$$

where

$$A = \frac{h}{8\pi^2 c I_a} \tag{2.2}$$

is the rotational constant, with I_a representing the principal moment of the inertia (see Figure 2.1) of the molecule about the axis a. The same expression holds for B and C with the corresponding I_b and I_c.

As the parameter κ approaches -1, the energy level formula approaches that of the symmetric top with $A > B = C$ namely,

$$E_r = \frac{B+C}{2} J(J+1) + \left(A - \frac{B+C}{2} \right) K_a^2 - D_J J^2 (J+1)^2 - D_{JK} J(J+1) K^2 - D_K K^4 \tag{2.3}$$

where the D's are centrifugal stretching constants, and where additional terms of powers higher in J^2, K^2 are often required. For the asymmetric top molecules with $\kappa \neq -1$, the calculation of the rotational energy requires the construction and diagonalization of matrices whose diagonal elements are given by Eq. (2.3), whose off-diagonal elements involve $B - C$ and two additional centrifugal stretching constants of the power of 4. The eigenvalues of these matrices are the rotational energy. From the eigenvectors of the diagonalization, one obtains effective angular momenta about each axis, $\langle P_a^2 \rangle$, $\langle P_b^2 \rangle$, $\langle P_c^2 \rangle$, with $P^2 = J(J+1)$.

Because the ν_1 and ν_3 normal modes of the ozone molecule are close to each other a Coriolis type resonance between $(\nu_1 \nu_2 \nu_3)$ and $(\nu_1 \pm 1 \ \nu_2 \ \nu_3 \mp 1)$ and a Darling-Dennison type resonance between $(\nu_1 \nu_2 \nu_3)$ and $(\nu_1 \pm 2 \ \nu_2 \ \nu_3 \mp 2)$ states will affect the line positions and intensities.

Finally, it should be mentioned that the ozone molecule has a pronounced absorption at around $1000\,\mathrm{cm}^{-1}$ due to its strong ν_3 asymmetric stretching mode. Interaction of infrared radiation with ozone molecules results in ro-vibrational transitions that produce bands of absorption lines.

2.2. Direct Absorption Spectroscopy

Gas phase direct absorption laser spectroscopy is based on the Beer-Lambert absorption law, which states that in the absence of optical saturation (*i.e.*, the absorption of radiation does not perturb the population distribution of the levels), the intensity of light $I(\nu)$ with a given wavenumber ν propagating through a homogeneous gas decreases along the distance $\mathrm{d}x$ by

$$\mathrm{d}I(\nu) = -\alpha_{ik} I(\nu) \mathrm{d}x \tag{2.4}$$

Here α_{ik} represents the absorption coefficient [cm^{-1}] for a transition $|i\rangle \rightarrow |k\rangle$ and depends on the population densities N_i, N_k of lower and upper level[1] with the associated g_i and g_k statistical weights and on the optical absorption cross section σ_{ik} [cm^2] of each absorbing molecule

$$\alpha_{ik}(\nu) = \sigma_{ik}(\nu)\left[N_i - \frac{g_i}{g_k}N_k\right] \tag{2.5}$$

which reduces to

$$\alpha_{ik} = \sigma_{ik}N_i \quad \text{for} \quad N_k \ll N_i. \tag{2.6}$$

The population density N_i is independent of I if the intensity is small enough (linear absorption). By integrating (2.4) and substituting (2.6) one obtains

$$I(\nu) = I_0(\nu)\exp[-\sigma(\nu)NL]. \tag{2.7}$$

The absorption coefficient is strongly frequency dependent around an absorbing feature. The peak absorption coefficient at line center ν_0 [cm^{-1}] can be written as a product between the integrated linestrength S and a peak-normalized lineshape function $f(\nu)$, which carries the entire frequency dependence of the absorption coefficient

$$\alpha(\nu) = Sf(\nu - \nu_0), \tag{2.8}$$

where the function $f(\nu - \nu_0)$ is normalized to unity so that

$$\int_{-\infty}^{+\infty} f(\nu - \nu_0)d\nu = 1. \tag{2.9}$$

Hence, a given molecular absorption line is characterized by its integrated line strength S, which is independent of pressure, while the lineshape function $f(\nu)$ has the same analytical form for all transitions, but its exact form depends on the line broadening mechanism.

Finally, it is practical to use the (dimensionless) sample optical density, denoted as τ, for the product of the three entities in the exponent of Eq.(2.7), *i.e.* the number density of the gas sample, the absorption cross section and the length of the interaction region

$$\tau(\nu) = \sigma(\nu)NL. \tag{2.10}$$

2.3. Spectral Line Intensity

The integrated absorption coefficient over a line is related to the Einstein coefficients for absorption and stimulated emission between the levels i and k by

$$\int_{\substack{over\ the\\ line}} \alpha_{ik}(\nu)\mathrm{d}\nu = \frac{h\nu_{ik}}{c}\frac{N_i}{g_i}\left(1 - \frac{g_i\,N_k}{g_k\,N_i}\right)B_{ik} \tag{2.11}$$

[1] In general, these states may have several types of degeneracy, which can be due to coupling of the nuclear spins with the rotational angular momentum, the product of state-independent nuclear spin factors, the spatial degeneracy, the spin degeneracy, lambda doubling degeneracy, etc.

where N_i and N_k are again the populations of the lower and upper states, respectively. The quantity in parentheses accounts for a reduction in the net absorption due to stimulated emission.

The most probable interaction of an isolated molecule with electromagnetic radiation is absorption via coupling between the radiation's electric field and the electric dipole moment of the molecule. Transitions related to higher electric multipole moments, or to interaction of magnetic dipole moment with the magnetic field are also possible, but they are comparatively weak. They may be of interest in the case of molecules for which the electric dipole transitions are forbidden, for example by symmetry. Assuming that the interaction of matter and radiation is only via an electric-dipole interaction, the Einstein coefficient B_{ik} is related to the weighted transition-moment squared $\mathfrak{R}_{ik}$ by

$$\mathfrak{R}_{ik} = \frac{3h^2}{8\pi^3} B_{ik} \tag{2.12}$$

The fundamental Eq.(2.11) does not depend on temperature since no equilibrium assumption has been made yet. In the case of local thermodynamic equilibrium, the number of molecules per unit volume in quantum state $|i\rangle$ at temperature T is given by the Boltzmann statistics. This allows to write

$$\frac{g_i N_k}{g_k N_i} = \exp\left(-\frac{c_2\,\nu_{ik}}{T}\right) \quad \text{and} \quad \frac{N_i}{g_i} = \exp\left(-\frac{c_2 E_i}{T}\right)\frac{N}{Q(T)} \tag{2.13}$$

where E_i [cm^{-1}] is the lower state energy, N is the molecular number density and c_2 the second radiation constant ($c_2 = hc/k = 1.438769$ cm K). The total internal partition function $Q(T)$ is given by

$$Q(T) = \sum_i g_i \exp(-\,c_2 E_i/T) \tag{2.14}$$

Substituting Eqs.(2.12) and (2.13) in Eq.(2.11), yields the integrated linestrength S

$$S = \frac{8\pi^3}{3hc}\frac{N}{Q(T)}\,\nu_{ik}\,\exp\left(-\frac{c_2 E_i}{T}\right)\left[1-\exp\left(-\frac{c_2\,\nu_{ik}}{T}\right)\right]\mathfrak{R}_{ik}. \tag{2.15}$$

If the molecule's linestrength at some reference temperature (T_{ref}) is known then the linestrength S for a transition at some temperature T can be determined as

$$S(T) = S(T_{ref})\frac{Q(T_{ref})}{Q(T)}\frac{\exp(-\,c_2 E_i/T)}{\exp(-\,c_2 E_i/T_{ref})}\frac{[1-\exp(-\,c_2\nu_{ik}/T)]}{[1-\exp(-\,c_2\nu_{ik}/T_{ref})]} \tag{2.16}$$

The third term on the right in Eq.(2.16) accounts for the ratio of Boltzmann populations, and the fourth term for the effect of stimulated emission, which only becomes significant in the far infrared and at high temperatures.

It should be emphasized that even though S describes the transition between two discrete energy levels $|i\rangle \rightarrow |k\rangle$, the absorption feature is not strictly monochromatic. There is always a spectral distribution around the central frequency $\nu_0 = (E_i - E_k)/h$ corresponding to a molecular transition with the energy difference $\Delta E = E_i - E_k$ between upper and lower levels. This phenomenon is due to several broadening mechanisms discussed in the following section.

2.4. Spectral Line Shapes

Broadening of an absorption feature occurs due to the phenomena in the medium that perturb the transition's energy levels or the way in which individual atoms and molecules interact with light.

2.4.1. Natural Broadening

Natural broadening arises because of an uncertainty in the energy of the states involved. Since natural broadening is the same for each molecule in an ensemble it is said to be a homogeneous broadening mechanism. In the near infrared region, the natural linewidth, associated with the finite lifetimes of the quantum states, is negligibly small compared to other lineshape effects [*Davis*, 1996]. For the measurement conditions that were present in this thesis (sample gas pressure $\ll 1$ atm, room temperature, 296 K) the dominant broadening mechanism was the inhomogeneous Doppler broadening due to the random thermal motion of the molecules.

2.4.2. Doppler Broadening

The major contribution to the spectral linewidth in a gas at low pressure is the Doppler width, which is due to the thermal motion of the absorbing molecules. At thermal equilibrium, the molecules follow a Maxwellian velocity distribution. Therefore, the distribution $f_G(\nu)$ of the emitted frequencies is[1]

$$f_G(\nu) = \frac{c}{\nu_0}\sqrt{\frac{m}{2\pi kT}}\exp\left[-\left(\frac{m}{2kT}\right)\left(\frac{c^2}{\nu_0^2}\right)(\nu-\nu_0)^2\right] \tag{2.17}$$

where k is the Boltzman's constant, m represents the mass of a molecule and T the absolute temperature (K). This is the so called normalized Doppler-broadened lineshape function, which covers a range of frequencies because many molecules having different velocities are being observed. Its FWHM is

$$\Delta\nu_D = \frac{\nu_0}{c}\sqrt{\frac{8kT\ln 2}{m}} \tag{2.18}$$

[1] For a detailed treatment see *Davis* [1996]; *Demtröder* [1996]

for which a more convenient form can be given

$$\Delta\nu_D = 7.1623 \times 10^{-7}\nu_0\sqrt{\frac{T}{M}} \tag{2.19}$$

where ν_0 is the absorption line center frequency [cm^{-1}], T the gas temperature in K and $M = N_A\, m$ is the molar mass (g). In terms of the Doppler-broadened linewidth $\Delta\nu_D$, the normalized Doppler lineshape function is

$$f_G(\nu) = \frac{2}{\Delta\nu_D}\sqrt{\frac{\ln 2}{\pi}}\exp\left[-4\ln 2\left(\frac{\nu-\nu_0}{\Delta\nu_D}\right)^2\right] \tag{2.20}$$

Considering the experimental conditions ($T \simeq 296\,\mathrm{K}$, $M_{\mathrm{O}_3} = 48\,g, \nu_0 \simeq 1040\ \mathrm{cm}^{-1}$), an approximative Doppler width for the ozone molecule can be obtained from Eq.(2.19)

$$\Delta\nu_D = 7.1623 \cdot 10^{-7}\ 1040\ \sqrt{\frac{296}{48}}\ \mathrm{cm}^{-1} = 1.85 \cdot 10^{-3}\mathrm{cm}^{-1}. \tag{2.21}$$

2.5. Isotope Fractionation for an Ozone Isotopomer

The following procedure can be used to obtain accurate isotope fractionation values from the spectroscopic measurements:

- Record two spectra (reference and sample) with spectral features of which one belongs to the most abundant isotopic species a ($^{48}\mathrm{O}_3$) and the other to the less abundant species x (*e.g.* $^{16}\mathrm{O}^{16}\mathrm{O}^{17}\mathrm{O}$).

- Convert both spectra from transmittance to optical density by application of Eqs.(2.7) and (2.10)

$$\ln[I(\nu)] = \ln[I_0(\nu)] - \tau(\nu) = P(\nu) - \sum_{i=1}^{n}\tau_i(\nu_{i0})f_i(\nu) \tag{2.22}$$

  where $P(\nu)$ is a quadratic polynomial for the baseline, which describes the intensity variation of the reference intensity as a function of frequency, $\tau_i(\nu_{i0})$ is the optical density of the i^{th} line at center frequency ν_{i0}, and $f_i(\nu)$ is the line-shape function (see Eq.(2.20))

- Perform a proper fit on the spectral features of both isotopic species to obtain precise values for $\tau(\nu_0)$.

- The isotope fractionation expressed by its δ-value can be determined from the isotopic ratio of the sample[1] and reference, respectively. Combining Eqs.(1.1) and (2.10), the isotope fractionation can be written as

$$\delta_S\,(x/a) = \frac{R_S}{R_{RM}} - 1 = \frac{\left(\frac{\tau_x}{\sigma_x L}\Big/\frac{\tau_a}{\sigma_a L}\right)_S}{\left(\frac{\tau_x}{\sigma_x L}\Big/\frac{\tau_a}{\sigma_a L}\right)_{RM}} - 1 = \frac{(\tau_x/\tau_a)_S}{(\tau_x/\tau_a)_{RM}} - 1 \tag{2.23}$$

  where it was implicitly assumed that the line-shape functions, and therefore the cross sections are the same for sample and reference, and can be eliminated from Eq.(2.23). Because the optical path length is the same for the two isotopic species, it cancels identically. Hence, for determination of the isotope fractionation a precise measurement of the optical density at the absorption line center for both isotopic species suffices.

Realization of the aforementioned spectroscopic measurement of isotope fractionation, thus, is conceptually straightforward, but still can result in significant experimental challenges. These challenges may be grouped into four categories: 1) control of the light source, 2) generation of sufficient absorbance, 3) suppression of noise and 4) locating suitable absorption lines. The last category is presented in the next section, while the first three will be described in Chapter 3.

2.6. Selection of Absorption Lines

The first challenge in the spectrometric isotope measurement is to identify a section of spectral ranges in which all of the isotopomers of interest have transitions that are

1. of comparable intensities (thus a weak absorption line for the most abundant, relative to the absorption strengths of the other isotopomers) in order to achieve similar signal levels.

2. within a small spectral range (smaller than the tuning range of the laser)

3. without interference from other strong lines.

Furthermore, to avoid saturation of the signal, the peak absorption should preferably be less than 50 %.

Ozone produced from molecular oxygen of natural isotopic composition results mainly in 5 different ozone species: $^{16}O^{16}O^{16}O$, $^{16}O^{16}O^{18}O$, $^{16}O^{18}O^{16}O$, $^{16}O^{16}O^{17}O$ and $^{16}O^{17}O^{16}O$. Because of the spin statistics, the number of ro-vibrational levels are twice for the asymmetric than that for the symmetric species. The absorption bands present a hybrid character that leads to a very crowded spectrum with line densities of approximately a few hundred transitions within $1\,\mathrm{cm}^{-1}$. An overview of the ν_3 ro-vibrational band of ozone isotopomers is shown in Figure 2.2.

[1] given by $R_S = N_x/N_a$

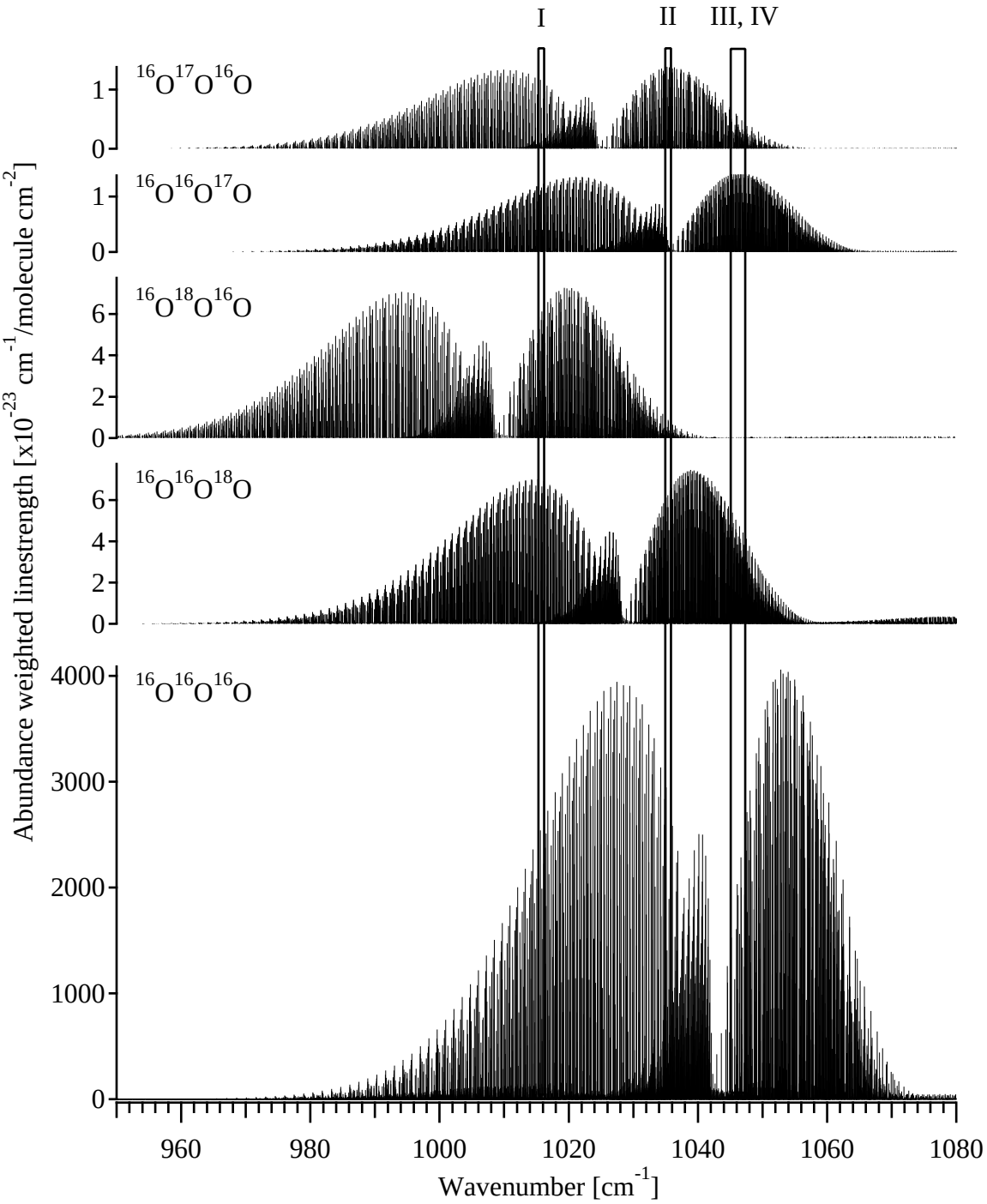

Figure 2.2.: Overview of the ν_3 ro-vibrational band of ozone isotopomers. For the sake of clarity, the different ozone species are displayed separately and on different scales. This way the isotopic shift of the ro-vibrational band centers can easily be observed. Furthermore, to better simulate the natural ozone absorption spectrum, the linestrengths of different isotopologues have been multiplied by their natural abundance. The spectral regions in which the individual absorption lines were found for isotope ratio measurement are indicated by narrow rectangles. The plot has been created using the ozone line intensities taken from HITRAN.

Comparing the abundance weighted line intensities of different isotopologues, it is obviously difficult to find spectral regions which satisfy all three conditions mentioned above. Moreover, an additional constraint is imposed by the laser diode itself. As we will see in the next chapter, the laser diode can be linearly frequency tuned only in its active modes, which are around $1\,\mathrm{cm}^{-1}$. Between two active modes there always is a frequency gap of about $3\,\mathrm{cm}^{-1}$ that cannot be accessed. Hence, only about 25 % of the full frequency range can be studied. Therefore, two different laser diodes have been investigated by tuning them over the entire frequency range ($\sim 70\,\mathrm{cm}^{-1}$). Finally, the diode which had more active modes in spectral ranges where the above mentioned selection criteria were fulfilled, has been chosen.

The selected spectral regions are indicated in Figure 2.2. In the frequency range of $1042 - 1044\,\mathrm{cm}^{-1}$ (regions III and IV) the $^{49}O_3$ absorption lines are relatively strong and, secondly, the Q-branch of the the main $^{48}O_3$ contains only few and weak lines. Hence, the first and the third selection criteria are fulfilled.

This also holds for the two other spectral regions (the range $1015.1 - 1015.9\,\mathrm{cm}^{-1}$ – region I and $1034.8 - 1035.6\,\mathrm{cm}^{-1}$ – region II). They are located in the P-branch of the main $^{48}O_3$, which is less dense than the R-branch (favors the third selection criteria), and where most of the ozone isotopologues with strong absorption lines are accessible (first selection criteria).

More details about the selected spectral regions will be given in Chapter 5, where individual micro windows that contain the selected absorption lines of the investigated isotopomers are discussed.

3. Description and Characterization of the Laser System

This chapter consecutively describes the principles, the optical set-up and the operation of the laser system used for the ozone isotope measurements. In section 3.3 some developments and improvements of the apparatus as well as the characterization of the system will be presented.

3.1. Optical Setup

The tunable diode laser absorption spectrometer (TDLAS) consists out of the following main parts: (The schematic layout of the optical set-up is shown in Figure 3.1.)

- a monochromatic light source,
- a cell containing the absorbing gas sample,
- and a detector with the associated electronics for detecting, amplifying and recording the transmission signal.

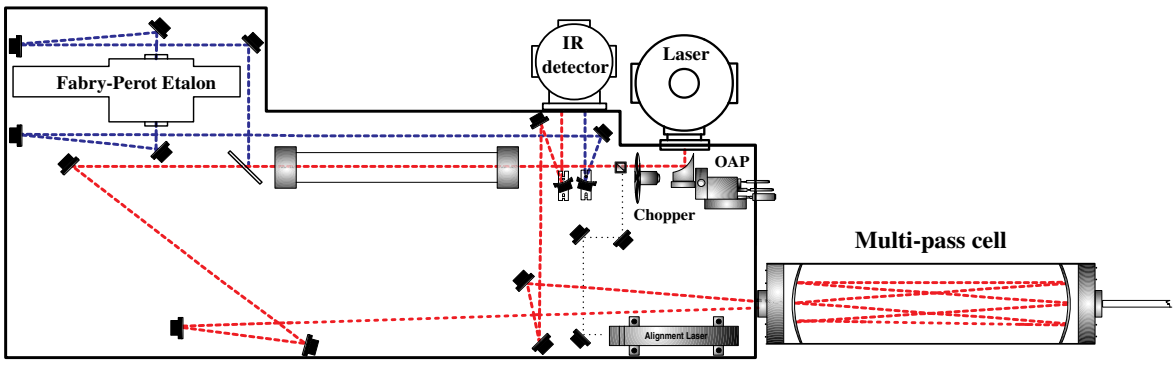

Figure 3.1.: The overall TDLAS instrument layout. The description of the main parts is given in the text.

The IR beam, emitted by the laser diode, is after collimation by an 90° off-axis parabola (OAP) mirror[1] divided by a wedged BaF_2 beamsplitter. The reflected beam

[1] Lead-salt diode lasers exhibit large beam divergence and astigmatism, which places critical and stringent alignment requirements on the collection optics, particularly to the first optical element, which is the off-axis parabola mirror.

is sent to an internally coupled confocal Fabry-Perot etalon (FPE), which serves as a relative frequency scale. After passing through the beamsplitter the IR laser beam is directed to a gold layered concave mirror (F/# 60), which then focuses the beam roughly to the center of a multipass cell (MPC). The narrow laser beam that enters through a BaF_2 window into the cell is reflected back and forth between the mirrors a large number of times before finally leaving through the central coupling hole (5.3 mm diameter) of the front mirror. The cell mirrors are spaced so that the beam exits after N passes at an angle from the input direction. After passing through the MPC or FPE the laser beam is focused into the IR detectors.

3.1.1. The Diode Laser

The light source used by the TDLAS is a semiconductor diode laser. This diode laser consists of a small, single crystal chip made from IV-VI group of semiconductor materials (lead-salt). Electronically, it functions like a diode. When a forward bias current is sent through the diode, the n-type semiconductor injects electrons into the junction region, while the p-type injects holes. Electrons and holes recombine and release a photon. The photon energy[1] is determined by the band gap of the material. At a particular drive current, the cavity mode spacing is given by $\Delta\nu = 1/2nL\,[\mathrm{cm}^{-1}]$, where $n \in (5-6)$ is the refractive index of the active layer and $L \simeq 250\,\mu$m the cavity length, respectively.

The refractive index of the laser diode depends on temperature. The diode current changes the junction temperature by ohmic heating and allows to tune the laser over a maximum range of about $1\,\mathrm{cm}^{-1}$. Varying the base temperature will tune the laser over its entire range (50 – $100\,\mathrm{cm}^{-1}$) but is slow, while variation of the drive current gives a faster modulation of the laser frequency. Both methods of frequency tuning are used in combination, but gaps are still remaining in the frequency coverage. These frequency gaps, the intrinsic line width (~ 30 MHz) as well as the frequency fluctuations of the diode laser and the cryogenic temperatures[2] required for operation constitute the major drawback of infrared diode lasers.

3.1.2. The Multipass Cell

According to Beer-Lambert's law, a direct and obvious approach for increasing the absorption signal is to increase the sample density. This, however, may be limited by the pressure broadening effect. Therefore, increasing the optical path length is a convenient means for enhancing infrared absorbance. The near-diffraction limited beam characteristics of lead-salt diode lasers allow beam shaping and propagation over long distances. This allows to use multipass cells that provide long optical absorption path lengths in a compact volume.

[1] Typical single mode powers are about 0.1 mW in continuous wave (cw) operation.

[2] The laser diode is mounted in a liquid nitrogen dewar that provides precise temperature controlled operation between 80 K and 120 K.

For the measurements a commercially available multipass cell ([*New Focus, Inc.*, 1995], Model 5612) has been used, which is a variation on the Herriott cell [*Herriott et al.*, 1964]. Astigmatic mirrors are employed to minimize the cell volume (3.2 liters) for a given path length (50 or 100 m). The cell body material is made from nickel plated aluminum, stainless steel end flanges and a Pyrex tube. The mirrors are made from nickel plated aluminum with broad-band dielectric coating providing a reflectivity of about 99.2 % in the 10 μm region.

The astigmatic multipass cell continuously refocuses the beams propagating through it and produce an output beam which is narrow and nearly collimated. The different radii of curvature along the two orthogonal axes produce beam spots on the mirrors which form a Lissajous pattern (see Figure 3.4) with a rectangular outer boundary. The spot pattern, therefore, almost fills the mirror area. This allows the cell volume to be uniformly sampled and not biased by a given sample geometry.

3.1.3. The Fabry-Perot Etalon

The etalon is used to produce a precise, relative frequency scale for the absorption spectra. The optical coupling to the etalon cavity is accomplished by means of a high transmission nitrocellulose pellicle beamsplitter mounted within the cavity. The entrance and exit beams pass through IR transmissive windows on either side of the resonator cavity, defining an axis normal to the resonator axis. The incident laser radiation undergoes multiple reflections between the mirrors and produces a transmission peak when an integer number of its wavelengths fit into one round trip of the cavity (ignoring the phase change on reflection). In the case of the confocal system the round trip distance is four times the cavity spacing, d, so transmission peaks occur when

$$d = m\lambda_1/4 \tag{3.1}$$

where m is an integer, defining the order of interference. The next resonant mode must fulfill the condition

$$d = (m+1)\lambda_2/4 \tag{3.2}$$

Adjacent fringe orders, therefore, are separated by the free spectral range (FSR), which is given by the frequency ($\nu = c/\lambda$) difference between the two adjacent maxima

$$FSR = c\left(\frac{1}{\lambda_2} - \frac{1}{\lambda_1}\right) = \frac{c}{4d} \tag{3.3}$$

and is independent of frequency.

The intensity of the multi-beam interference which is transmitted through the etalon is described by the Airy-function

$$I = I_0 \frac{(1-R)^2}{(1-R)^2 + 4 \cdot R \cdot \sin^2\left(\frac{\delta}{2}\right)} \tag{3.4}$$

where δ is the phase shift between successive transmitted rays, R is the reflectivity of the mirror surfaces and I_0 is the incident intensity. If we take into account the

losses due to absorption A by the mirror material then instead of Eq.(3.4) we have

$$I = \frac{4(1-A)(1-R-A)^2}{(2-2R-A)^2} \frac{I_0}{1+F_A \sin^2\left(\frac{\delta}{2}\right)} \tag{3.5}$$

where

$$F_A = \frac{4R\sqrt{1-A}}{(1-R\sqrt{1-A})^2} \tag{3.6}$$

is called the generalized *finesse coefficient*.

3.2. Control System and Data Acquisition

The infrared detectors (*Laser Photonics Inc.*) provide IR signal detection, using photoconductive mercury cadmium telluride (HgCdTe) elements, throughout the 1 to 20 μm spectral region. Both detector elements are mounted onto a LN_2 dewar and have matched low noise preamplifiers. The preamplified signals (max. 10 V) are fed to digital signal processing (DSP) lock-in amplifiers (LIAs, SRS 540, *Stanford Research Systems Inc.*). Hence, the need for amplitude modulation of the IR laser signal, which is accomplished by a mechanical wheel chopper. This chopper has a modulation frequency of $\simeq 1$ kHz to which the LIAs are locked. The usual LIA settings are 100 – 500 mV full scale, 3 ms time constant and a dynamic reserve of 24 dB/octave. The amplified and filtered output electrical signals are digitized by a fast (20 kHz/s), 16-Bit resolution multifunction data acquisition board - DAQ (PCI-MIO-16XE-50, *National Instruments*) on a PC, where they are stored for further analysis. A software, based on LabVIEW 5.0 graphical programming (*National Instruments*) permits full automated data acquisition and system control.

Absorption spectra are obtained in the following way. First, the basis current and temperature of the laser diode is set to the desired value via a tunable diode laser controller (*Laser Photonics, Inc.*, Model L5830). The injection current (0–500 mA range) is supplied by a precision analog circuit, which is controlled by 16-bit digital-to-analog converter (DAC). Then, the software creates a digital waveform that is converted to an analog voltage ramp signal at a rate of 20 kHz by a 12-bit DAC[1] ($\pm$ 10 V) and converted into a current signal by the laser controller (modulation transfer function: 20 mA/V), is added. This serves for a continuous frequency tuning (typically 24 mA in 40 s divided in 3000 steps) of the laser light that the diode emits. Finally, the signal that reaches the detector is processed as it has been described above.

[1] In the present situation the resolution of the basis current and of the ramp signal of the laser controller are different (7.6 μA and 97.7 μA, respectively). Hence, the use of external modulation and also the inclusion of a voltage-divider that reduces the DAC generated voltage (10 V) by a factor of 16.19. This way the current resolution is set to 6 μA. With the laser diode's tuning rate of $\simeq 3.4 \cdot 10^{-2}\,\mathrm{cm}^{-1}/\mathrm{mA}$, the limit for TDLAS frequency precision is $\sim 1.8 \cdot 10^{-4}\,\mathrm{cm}^{-1}$.

3.3. Characterization of the TDLAS

3.3.1. Laser Diode Characteristics

The selection of a proper laser diode, which emits in spectral regions where the ro-vibrational transitions of the different isotopomers of the studied molecule take place, is crucial for isotope ratio measurements. This was done by taking different laser diodes, tuning over their entire range and analyzing the recorded absorption spectra. The decision was made based on the criteria already discussed in subsection 2.6 (page 22).

An individual mode continuously tunes over about $1\,\mathrm{cm}^{-1}$ with increasing drive current. However, when the drive current reaches a given value mode hopping occurs. This mode hopping characteristics, which leads to inaccessible gaps in the frequency range is shown in Figure 3.2.

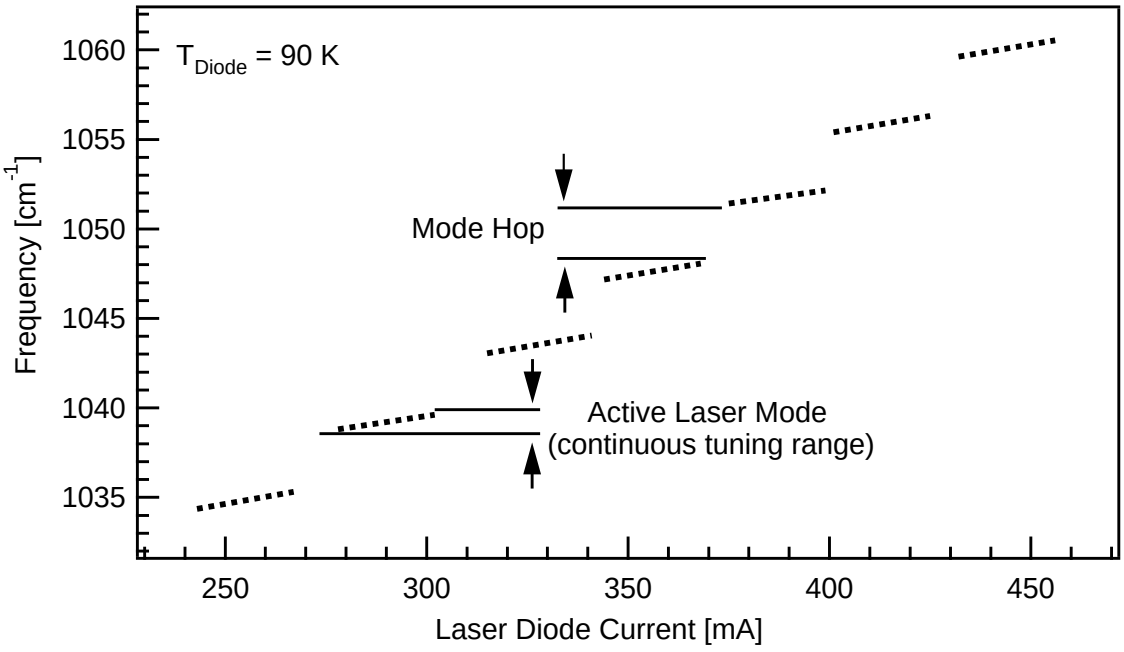

Figure 3.2.: Tuning the laser diode by changing the drive current at fixed temperature. The frequency range of the active modes of the laser diode are presented by dots. In these ranges the laser diode can be continuously tuned, by changing the drive current, with a tuning rate of $\mathrm{d}\nu/\mathrm{d}I \simeq 3.4 \cdot 10^{-2}\,\mathrm{cm}^{-1}/\mathrm{mA}$. When the drive current reaches a given value a mode hop occurs. The frequency jumps can be explained by the fact that the oscillating mode does not fit the resonator length anymore and the oscillation of another better conditioned mode starts.

The temperature tuning characteristics of the laser diode at constant drive current is shown in the Figure 3.3.

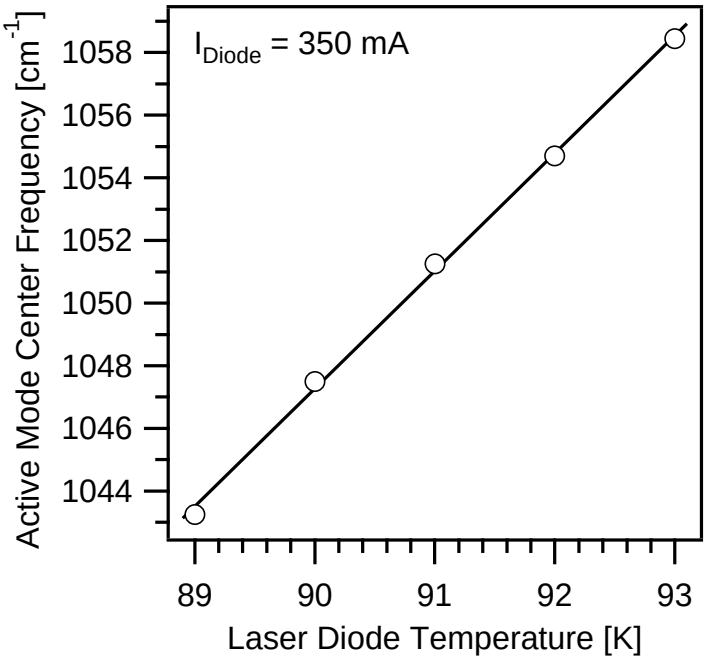

Figure 3.3.: Tuning the laser diode by changing its heat sink temperature at fixed drive current of 350 mA. The central frequencies (○) of the laser diode's active modes are plotted as a function of temperature. A linear fit performed through these points defines the laser diode temperature tuning rate $\mathrm{d}\nu/\mathrm{d}T$. For this laser diode a value of $3.76 \pm 0.08\,\mathrm{cm}^{-1}/\mathrm{K}$ was found.

3.3.2. Reduction of Optical Noise in the MPC

When an optical absorption cell with many reflections is used in the observation of weak molecular absorption lines, interference fringes can be the most important effect limiting sensitivity. These fringes can be due to

- spillover of light from the beam spots on the cell mirrors
- surface quality of the optical elements (scattering effects)

In the following, the individual steps for improving the signal to noise ratio in the TDLAS optical system are described.

According to *McManus and Kebabian* [1990] the most important source of fringes is the spillover of light from the beam spots which neighbor the coupling hole on the cell's front mirror so that light leaking out is captured by the collecting optics and focused on the detector. In order to reduce this source of fringes one can try to space the spots widely enough on the mirrors so that such spillover effects are reduced.

In the standard arrangement, the spot pattern is highly rectangular, although *Zahniser* [priv. comm.] pointed out that this can be changed to a square pattern, which has several advantages: i) the distance from the nearest neighbor spots to the coupling hole increases, ii) the scattered light intensity is distributed more uniformly over the mirror surface, and iii) the spot pattern is easier to recognize during alignment.

For investigation of different mirror configurations that may have the above listed advantages, a program has been written, which simulates the ray propagation in the multipass cell (For more details consult the Appendix). This way, a number of

configurations have been studied by taking different combinations of input parameters (separation distance between mirrors, mirror rotation angles and the entrance beam slope in both directions). The selected configuration can be accomplished in the cell by adjusting the distance between the mirrors and by changing their rotation angle. The agreement between calculated and practically realized configurations can be easily seen by comparing the spot patterns of the two (Figure 3.4).

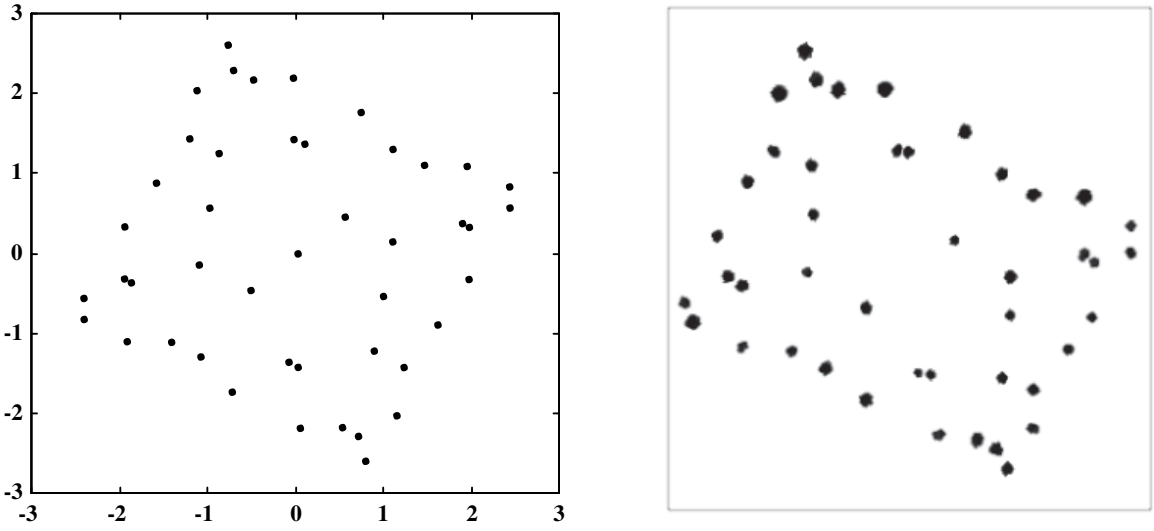

Figure 3.4.: Comparison of calculated (left) and observed (right) front mirror spot patterns. The calculated beam spot pattern was simulated using the parameters given in the Appendix, while the observed spot pattern was taken by a digital camera in dark room using the HeNe laser beam. The picture was converted to grey scale and then to its negative image.

Another source of fringes is the scattering of coherent laser light from optical surfaces. The reflections occur mainly on the multipass cell mirrors, thus, a very good quality of the optical reflective coatings is needed. The standard mirrors (*New Focus*), which due to the fabrication procedure that allows mass production, had inferior surface quality and, therefore, they were replaced by a new pair of hand polished, high surface quality mirrors from *Aerodyne Research Inc.*

An additional problem arises from the instability of the overall multipass cell against pressure changes. The original housing design does not keep the mirrors fixed when the cell is evacuated. Significant changes in the HeNe laser beam spot pattern could be observed when the cell was brought from atmospheric pressure down to a few Torr pressure due to pressure induced displacements of the mirrors. The mirror alignment can be performed only at atmospheric pressure because in order to move the mirror tilt/translation set screws, the cell back plate must be removed. The only way to keep the mirror positions fixed was to add some more stability to the housing part. Therefore, two "horse-shoe" shape aluminium profiles, connected with two adjustable steel bares, have been designed. This construction fits to the top side of both mirror housings and provides very good stability.

Finally, the fringe amplitudes were suppressed to the range of about one to five $\times 10^{-4}$ absorption equivalent. This is close to the limit that can be obtained using this type of multipass cells [*McManus et al.*, 2002; *Richard et al.*, 2002; *Worsnop et al.*, 1993]. The net result of the improvements presented above is shown in Figure 3.5, where the relative deviation of the background signal, taken with empty cell, from its channel sliding averaged value (over 110 channels) is presented.

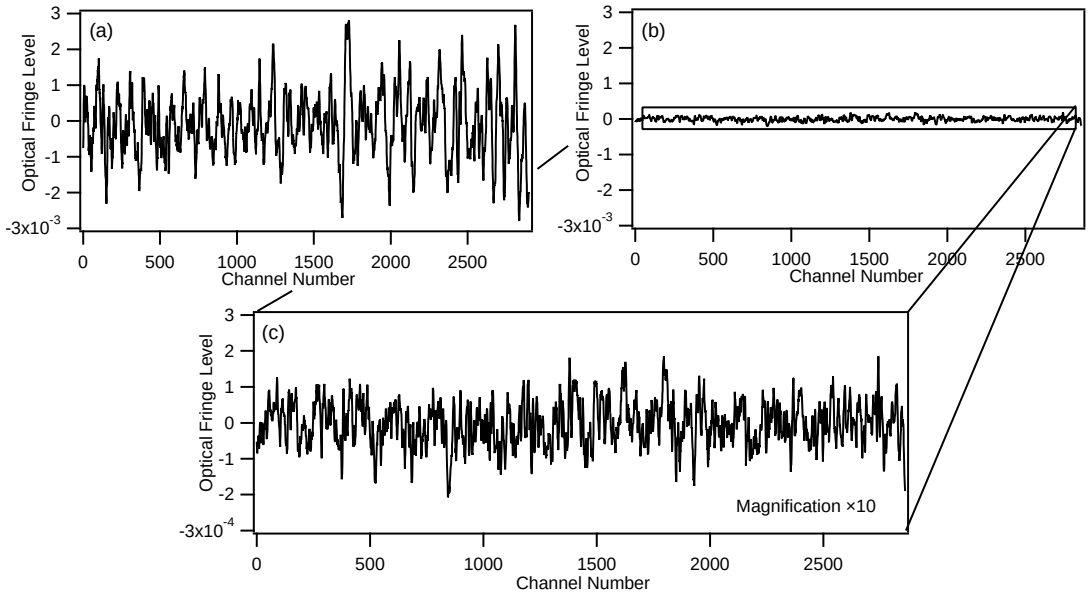

Figure 3.5.: Interference fringes generated by the multipass absorption cell. Figure (a) shows the fringe level observed using the multipass cell without any improvements. These fringes were high enough to obscure spectral features of interest. In Figure (b) the same multipass cell with similar optical alignment is presented, but after a number of changes (for more details see text). Figure (c) is the same as (b), but magnified. Here, the optical interference fringes with the magnitude of $\sim 10^{-4}$ absorption units can clearly be observed.

3.3.2.1. Ozone Lifetime in the MPC

The instability of the ozone molecule places another important constraints on the spectroscopic measurements of the isotopic fractionation. As it was discussed in Chapter 2, for an accurate determination of the isotope fractionation a precise measurement of the optical thickness of the main and rare isotopic species is needed (see Eq. 2.23). However, there is little chance to find two adjacent absorption lines of different ozone isotopologues, which fulfill the selection criteria presented on page 22. Therefore, one needs to tune the laser diode over a wider frequency range (*e.g.* $1\,\mathrm{cm}^{-1}$). This, however, requires some time (about 48 seconds/scan) and – for a better statistics – one should also perform repeated scans (*e.g.* from 10 up to 20 scans). Hence, in order to accurately measure absorption linestrengths, the recording time for a given spectral range will be about 16 minutes. This implies that the ozone concentration in the multipass cell should not change during the that time.

But ozone is a powerful oxidizing agent and it spontaneously decomposes under all ordinary conditions. The decomposition is speeded up by solid surfaces [*Horváth et al.*, 1985]. Therefore, it may be easily destroyed on the multipass cell's internal metal walls, too.

To experimentally investigate the ozone stability in the multipass cell, O_3 has been introduced into the cell, and repeated scans have been performed. After evaluating the linestrength of an individual, well separated ozone absorption line for all the consecutive scans, and plotting them in function of time at which the spectra were recorded, an exponential fit has been performed. According to the fit, the ozone sample in the multipass cell has a lifetime of about 8 minutes (see Figure 3.6). This rapid ozone decomposition could only be due to some catalytic reaction with the inner metal surface of the multipass cell. After demounting the cell, it was found that the nickel coating from the anodized aluminium surface begun to peel off, and thus, to act as a catalyst. Therefore, a new coating of the whole cell's metal surfaces was needed.

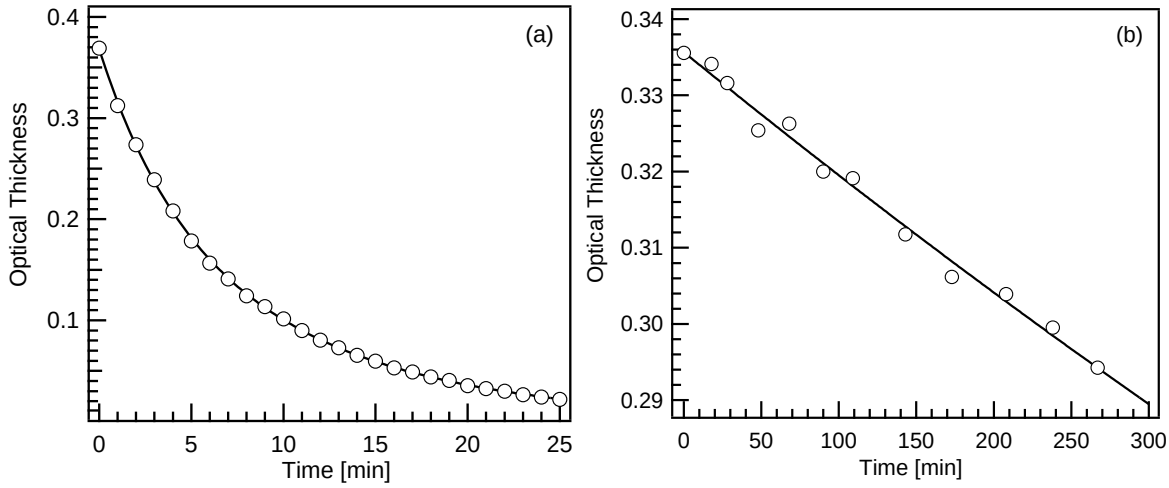

Figure 3.6.: Ozone number density evolution in the multipass cell. Panel (left) Standard cell. Catalytic ozone decomposition, which takes place on the cell internal metal surfaces, results in an almost instant decrease in ozone concentration ($t_{1/e} \simeq 8$ minutes). Panel (right) Gold coated cell: Increased ozone lifetime to 33 ± 1 hour. $t_{1/e}$ was calculated using an exponential decay model to fit the experimental data. Note the different scales in both panels.

There are only very few metals which are not oxidized by ozone: gold, platinum and iridium. After removing the astigmatic mirrors from their mount, the cell metal parts have been coated with a thin layer of gold.

When the multipass cell with the gold coated metal surfaces has been placed back to its proper position, another experimental check, similar to the one described above, was performed. The results of the measurement are presented in Figure 3.6, and can be compared with the previous one. The ozone lifetime was extended by a factor of 250.

3.3.3. Frequency Calibration of the FP Etalon

A typical scan produces two sets, ozone and etalon spectrum, of 3000 digitized data points covering a spectral range of $\sim 1\,\mathrm{cm}^{-1}$. During the scan, the etalon produces optical interference fringes[1] shown in Figure 3.7. These fringes can be used as frequency markers to generate a relative frequency scale. The position of each transmission peak is calculated by a fit procedure that uses the parameterization of the Airy function.

$$f(x) = \frac{A}{1 + F \cdot \sin^2\left(T \cdot \frac{x - x_0}{2}\right)} \times P(x) \tag{3.7}$$

where A is the amplitude, T a factor to adjust periodicity, x_0 one etalon-fringe position, F the finesse coefficient and $P(x)$ a quadratic polynomial to account for the baseline variation, which is due to the frequency dependent emission power of the laser diode.

Choosing A, $P(x)$, F, x_0 and T as free parameters, a non-linear least square fit is performed on the etalon transmission spectra. One such fit result is shown in Figure 3.7.

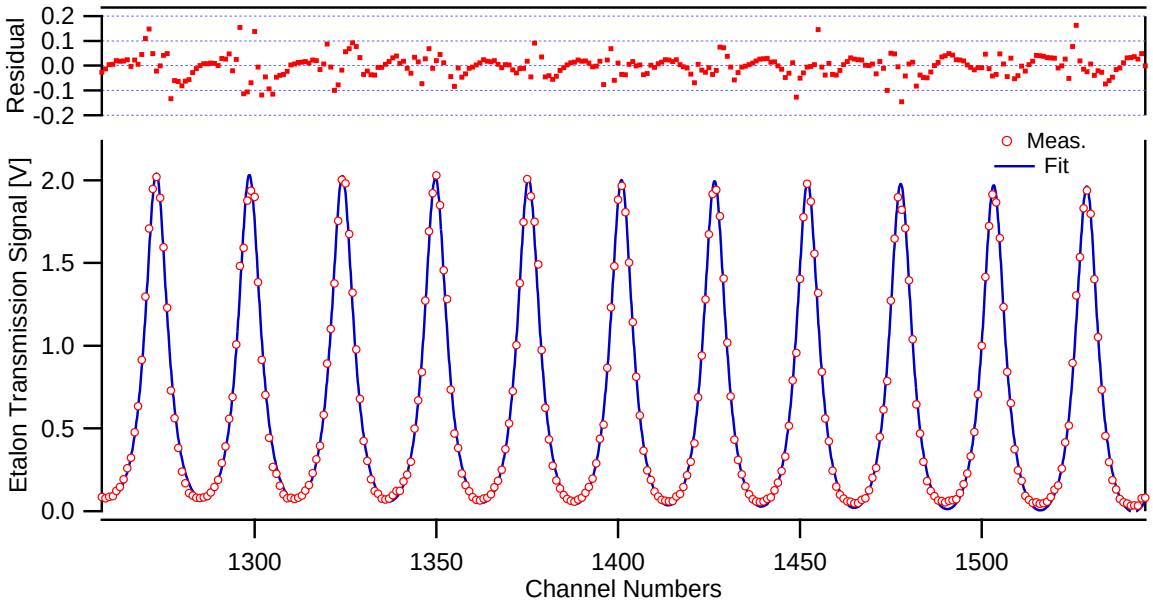

Figure 3.7.: Transmission signal of the Fabry-Perot etalon. Comparison of measured and fit model data. The noise character of the residual plot suggests that the fit model properly describes the experimental data.

A plot of etalon-fringe order *vs.* fringe position in channel numbers shows that the emission frequency of the laser diode varies slightly nonlinear with the injection current (Figure 3.8). Hence, a higher order polynomial dependency is more appropriate to use.

[1] A confocal cavity has the advantage that resonances occur at the same spacing of the mirrors for all optical modes.

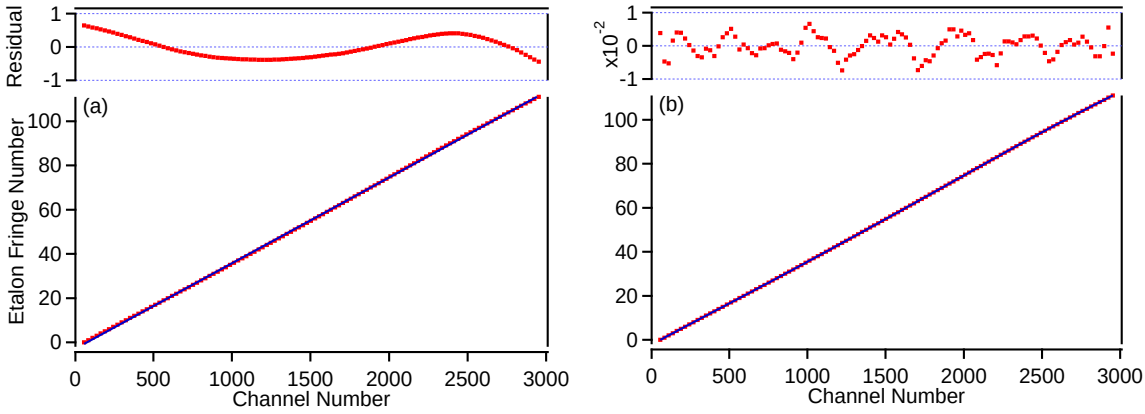

Figure 3.8.: Etalon fringe order *vs.* channel numbers. Panel (a): The residual of a linear fit through the data points clearly shows that the emission frequency of the laser diode does not follow the injection current ramp in a strictly linear manner. Panel (b) presents the case when a high order polynomial is used for the fit. Evidently, a linearization of the relative frequency scale is necessary.

For an exact frequency calibration the etalon transmission signal is used to obtain spectra with a linearized, relative frequency scale. The absolute frequency scaling in the measurements is achieved by comparison with accurately known ozone absorption line positions.

The calibration procedure is as follows: First, the ozone absorption spectrum is plotted against the linearized relative frequency scale. A multi-peak fit with a gaussian line shape model is used to determine the initially selected ozone absorption line positions. Second, these relative line positions are plotted against the transition frequencies of the same lines taken from the HITRAN database. Generally, 4 to 7 such lines are used in a spectroscopic window. A linear fit through these points gives us the correlation between the two scales, thus providing the absolute frequency scale. The accuracy of this procedure was tested by comparing simultaneously recorded etalon, CO_2 and O_3 spectra (for more details see Appendix). When the absolute frequency scale is generated from very accurately known CO_2 absorption lines, then the ozone absorption line positions can be determined independently. These measured values have been compared with the values from the HITRAN database. The agreement has been found to be $\simeq 6 \cdot 10^{-5}\,\mathrm{cm}^{-1}$. The accuracy of the frequency scale, which is in the percent range of the Doppler line width, already indicates that a percent scale accuracy may be achieved in the linestrength measurements, too.

However, there are several potential sources of errors that limit the precision of the frequency scale, and consequently the linestrength measurements, in TDL spectroscopy. Laser diode frequency noise, optical feedback and data-reduction errors are random in origin [*Avetisov et al.*, 1993]. Other phenomena produce systematic errors related to laser diode internal features.

4. Ozone Generation and Mass Spectrometric Analysis

This chapter is concerned with generation of different ozone samples and their mass spectrometric characterization. After a general presentation of the ultra high vacuum (UHV) system in which the gas handling and the ozone sample generation has been performed, the mass spectrometer employed for isotopic composition analysis is described. Then various methods used for the preparation of ozone samples are individually discussed in terms of their associated physical background and technical details. Finally, the isotopic composition of the different ozone samples are characterized mass spectrometrically.

4.1. The Experimental Setup

4.1.1. Gas Handling System

A layout of the gas handling system is presented in Figure 4.1.

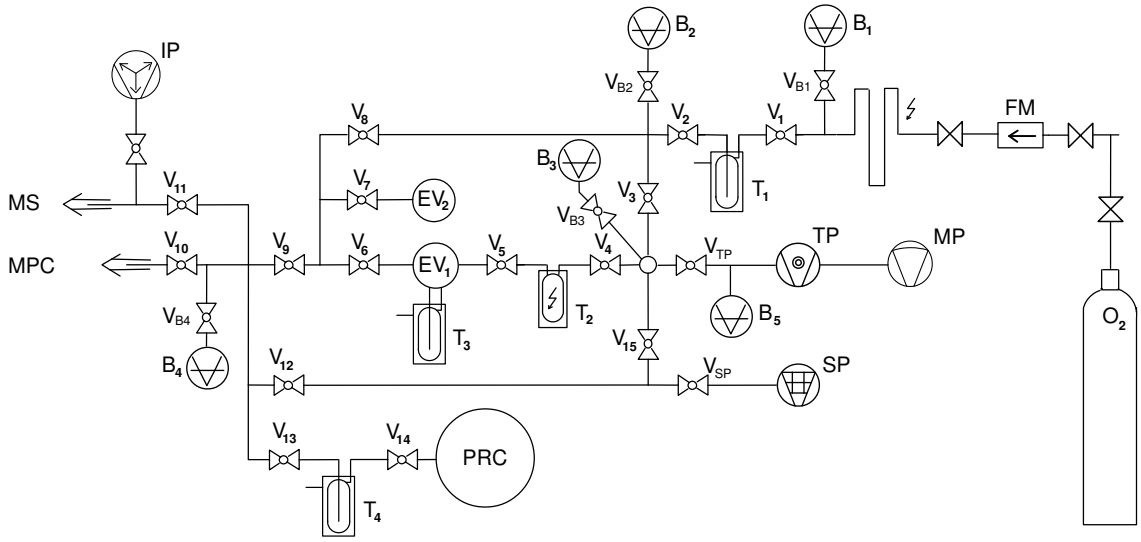

Figure 4.1.: Vacuum system employed for gas handling and ozone sample generation.

The all glass (*Duran, Schott Co.*) vacuum system permits several operations: controlled ozone generation in various environments (electric discharge, visible light photolysis) and at different physical parameters (temperature, pressure, flow-rate),

as well as gas sample separation (*e.g.* ozone from molecular oxygen) and sample transfer to the TDLAS or/and to MS.

The abbreviations used in Figure 4.1 are:

V - teflon sealed glass valves (*Glass Expansion*, Australia),

MV - metal valves (Type 4BRG, *Nupro*, USA)

FM - flow meter (Type 179A, MKS, USA)

T - temperature controlled cold trap. The attached LN_2 dewar can be pumped, thus allowing to control the LN_2-temperature by maintaining selected vapor pressures.

B - capacitance manometers (Type MKS-Baratron, USA and type *Edwards*, England, respectively.),

TP - turbomolecular pump (V70LP, *Varian*, Italy),

SP - sorption pump (MDC, USA),

IP - ion pump (*Starcell* 30, *Varian*, Italy),

PRC - reactor for visible light photolysis

MS - mass spectrometer

MPC - multipass cell

Further components, not shown in Figure 4.1, are a tesla coil connected to a high-frequency voltage generator (15 kV, 20 kHz) for electric discharge generation, and a 150 W tungsten lamp (*Osram* HLX64633 filament), mounted into an *Oriel* (Type 60125) lamp housing. At this point it should be mentioned that in the present work two different methods were employed to study ozone formation: electric discharge and photolytic recycling. Both methods are discussed in detail in the following sections.

The cold trap (T_2), which also functions as a discharge cell, is a glass cylinder with a diameter of 5 cm and 16 cm long. On its outer surface two copper electrodes are mounted. The photolysis reaction cell (PRC) is a 2 l glass sphere, which is silver coated to increase the number of reflections, and thus, to provide an efficient photolysis. An evacuated cylindrical cuvette is attached to the top of the glass sphere. The cuvette dimensions are 60 mm in diameter and length. It allows the visible light beam to enter into the PRC, and at the same time thermally decouples the sphere from the heat of the tungsten lamp (For a detailed scheme see Figure 4.3).

4.1.2. Mass Spectrometer

The mass spectrometer as well as the analysis method has been described in detail elsewhere [*Janssen*, 1999; *Krohn*, 1998; *Schellenbach*, 1995]. Briefly, a homemade (University of Minnesota), double focusing (Mattauch-Herzog geometry) mass spectrometer with a mass resolution of $(M/\Delta M)_{1\,\%} = 55.7$ and a sensitivity of $\eta = 9 \cdot 10^{-7}$ A/Torr is employed. The gas is introduced to the mass spectrometer ion-source through a manually operated variable leak valve (*Granville-Phillips*, USA). The analysis takes place in a "peak-jump-modus", where only the signals from the mass-peaks 32, 33 and 34 u are measured. For a better statistics the integration time for the less abundant isotopologues is increased. The analysis cycle is repeated about 100-200 times. First, a background spectrum is recorded and the median of the count-rates for individual isotopologues is calculated. Then the spectrum of the molecular oxygen sample is measured and properly background corrected. Finally, the isotope ratios ^{33}X and ^{34}X are determined. Figure 4.2 shows these ratios over time. There is no trend, and the fluctuations in the measured isotopic values of the standard O_2 can be attributed to the stability of the measurements, to the statistical errors or to errors due to the gas handling procedures.

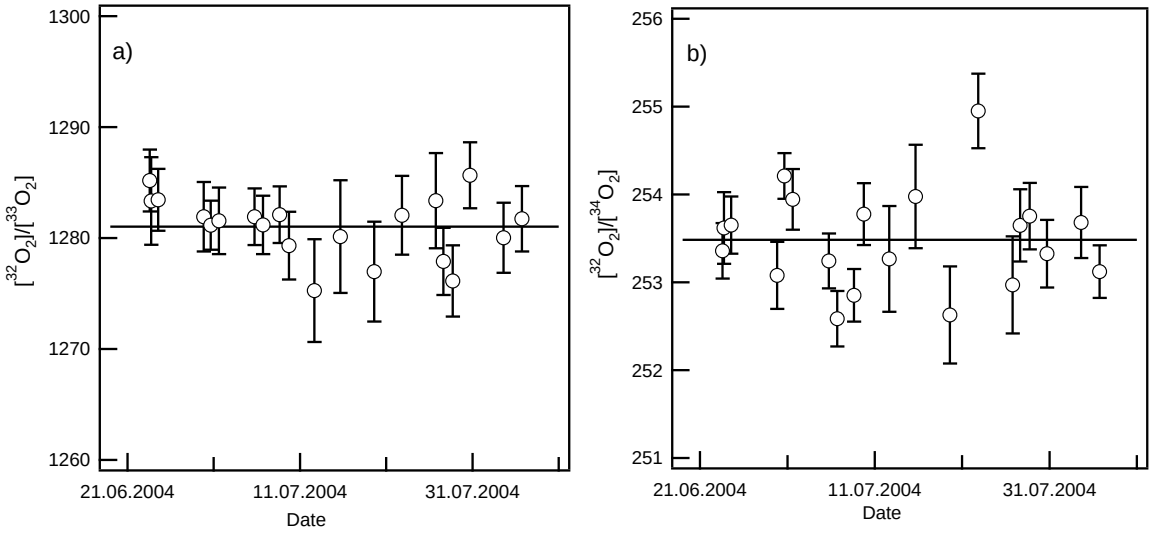

Figure 4.2.: The isotopic composition of the molecular oxygen used for ozone sample generation. The average value presented as a line is 1281.02 ± 0.62 for ^{33}X and 253.31 ± 0.12 for ^{34}X, respectively. Here we adopt the reciprocal of the isotope ratio $X = 1/R$, which has an "easy-to-use" value ($^iX = [^{32}O_2]/[^iO_2] \gg 1, i = 33, 34$)

The precision of the mass spectrometer has been determined by repeatedly measuring the oxygen gas used for sample preparation. From the scatter of these measurements an uncertainty of 0.3 % and 0.4 % for the $^{50}O_3$ and $^{49}O_3$, respectively, was estimated. In addition, the mass spectrometer accuracy has been checked by comparing the repeatedly measured ozone fractionation values of oxygen gases that had about the same isotopic composition as the ozone samples, with those of a commercial high precision isotope ratio mass spectrometer (Delta^{XL}Plus *ThermoQuest*

Table 4.1.: Comparison of the measured enrichments E_u of the mass spectrometer (MS) employed in this work with the high precision isotope ratio mass spectrometer (IRMS). In the last lines the average values $\bar{E}_u$ followed by their standard deviations ΔE_u that refer to the scatter of the independent measurements, and the difference (Diff $= \bar{E}_{u(IRMS)} - \bar{E}_{u(MS)}$) are shown.

	$E_{49}(\%)$		$E_{50}(\%)$	
#	MS	IRMS	MS	IRMS
1.	13.70	14.640	18.99	19.147
2.	13.74	14.648	18.44	19.158
3.	14.17	14.637	19.03	19.156
4.	-	14.634	-	19.157
$\bar{E}_u$	**13.87**	**14.640**	**18.82**	**19.155**
ΔE_u	0.21	0.005	0.27	0.004
Diff	**0.77**		**0.34**	

Finnigan). The comparison of the two mass spectrometers is given in Table 4.1. The discrepancy between the two mass spectrometers reveals a reduced dynamic range of the small MS when compared to the large instrument. Although it is difficult to identify the real source of this effect, most likely the small size (increased gas-wall interactions) of the employed mass spectrometer and the large differences between the isotopic signatures of the sample and reference gases give rise to a pronounced cross contamination via ad- and desorption effects in the inlet system and ion source of the MS [*Gonfiantini et al.*, 1997]. Such cross contamination effects always lead to scale contraction [*Meijer et al.*, 2000]. Therefore, a scale expansion factor was applied to the mass spectrometer values that resulted in a correction of 0.77 ‰ and 0.34 ‰ for the ^{17}O and ^{18}O containing isotopologues, respectively.

The oxygen gas used for ozone sample generation is of high purity O_2 (5.5, *Messer Griesheim*, 200 bar in 10 l). Its ^{17}O and ^{18}O isotopic composition has been determined with the mass spectrometer several times.

4.2. Ozone Sample Generation

4.2.1. Visible Light Photodissociation of Ozone

Photodissociation is the breaking of one or several bonds in a molecule through the absorption of light. Dissociation by a single photon – usually in the optical or the ultraviolet region – promotes the molecule from the ground electronic state to an excited electronic state with a repulsive potential energy surface (direct) or with a surface that crosses such a repulsive surface (indirect). Because of the weak O_2-O bond, for which the dissociation energy is $D_e = 1.06 \pm 0.04$ eV [*Allan et al.*, 1996], absorption of light at wavelengths as long as 1181 nm can lead to the dissociation of ozone. The photodissociation of ozone in the spectral region 410–720 nm, (the Chappuis band)

shows a large continuum with two maximum absorptions ($\sigma = 4.8 \cdot 10^{-21}\,\mathrm{cm}^2$ at 575 nm and $\sigma = 5.2 \cdot 10^{-21}\,\mathrm{cm}^2$ at 603 nm) overlapped by diffuse vibrational structure.

Absorption of light in the Chappuis band implies the primary photodissociation process

$$O_3(^1A_1) + h\nu \rightarrow O_3^* \rightarrow O_2(^3\Sigma_g^-) + O(^3P) \tag{4.1}$$

Although production of $O_2(^1\Delta_g)$ is energetically possible below 611 nm via the spin forbidden process

$$O_3(^1A_1) + h\nu \rightarrow O_3^* \rightarrow O_2(^1\Delta_g) + O(^3P) \tag{4.2}$$

there is no experimental evidence that this channel is operative.

The product state distribution of reaction (4.1) has been studied [*Levene et al.*, 1987]. Since the dissociation dynamics is both vibrationally adiabatic and rotationally impulsive, the ozone photodissociation in the Chappuis band is an attractive source of translationally hot $O(^3P)$ atoms with accessible energies of 0.4 to 0.7 eV.

The large scale *ab initio* calculations [*Braunstein et al.*, 1991] suggest that the oscillator strength in the Chappuis band comes from the dipole allowed transition $(^1B_1) \leftarrow (^1A_1)$. A conical intersection which couples the bound $^1B_1$ to a "dark" dissociative $^1A_2$ state is responsible for the diffusive nature[1] of the absorption band. The existence of a conical intersection near to the Franck-Condon region accounts for the mechanism whereby only ground electronic state products are observed for excitation to the Chappuis band. The excited molecule leaks from the upper adiabatic surface to the lower adiabatic surface where it then can dissociate to $O_2(^3\Sigma_g^-) + O(^3P)$.[2]

4.2.2. Ozone Photolysis Recycling

Ozone photodissociation in the Chappuis band has been utilized by *Morton et al.* [1990] to form ozone from O and O_2 in their electronic ground-states. It was found that without excited states being involved the $O(^3P) + O_2(^3\Sigma_g^-)$ recombination reaction alone produces the large, anomalous isotope effect.

Since other methods used for ozone production, such as UV-photolysis and electric discharge, generally involve secondary chemistry with excited electronic states and charged particles, the visible light photolysis recycling provides the most simple and cleanest method to study the ozone isotope effect. Furthermore, the physical parameters like gas temperature and pressure can be accurately measured and monitored during the experiment. These parameters have been identified as very important factors that influence the ozone isotopic fractionation.

[1] Despite considerable progress with accurate ab initio electronic-structure calculations for excited states of ozone in recent years, the interpretation of the irregular and diffuse vibronic features of the Wulf-Chappuis bands and their assignment to electronic states is still not clear.

[2] According to several recent *ab initio* studies [*Flöthmann et al.*, 1997; *Woywod et al.*, 1997] it is now established that the Chappuis band system is the result of excitation of the two lowest excited singlet states. In C_{2v} symmetry they have $^1A_2$ and $^1B_2$ electronic character whereas in C_s nuclear symmetry they both have $^1A''$ electronic symmetry.

Briefly, ozone photolysis recycling is characterized by:

- Absorption of visible light by O_3 in the Chappuis band, which leads to dissociation of ozone. The resulting photofragments $O(^3P)$ and $O_2(^3\Sigma_g^-)$ are exclusively in their electronic ground states. Thus, ozone can be used as a source of atomic oxygen that is in its electronic ground state.

- When a small amount of ozone is placed in a much larger bath of O_2 molecules, the oxygen atoms participate in fast isotope exchange reactions and isotopically equilibrate with the molecular oxygen. They also reform ozone molecules such that essentially no net destruction of ozone occurs.

- The isotopic composition of the newly formed ozone will be completely determined by the surrounding O_2 bath composition and by the isotope fractionation mechanisms in the formation and in the photolytic destruction of ozone.

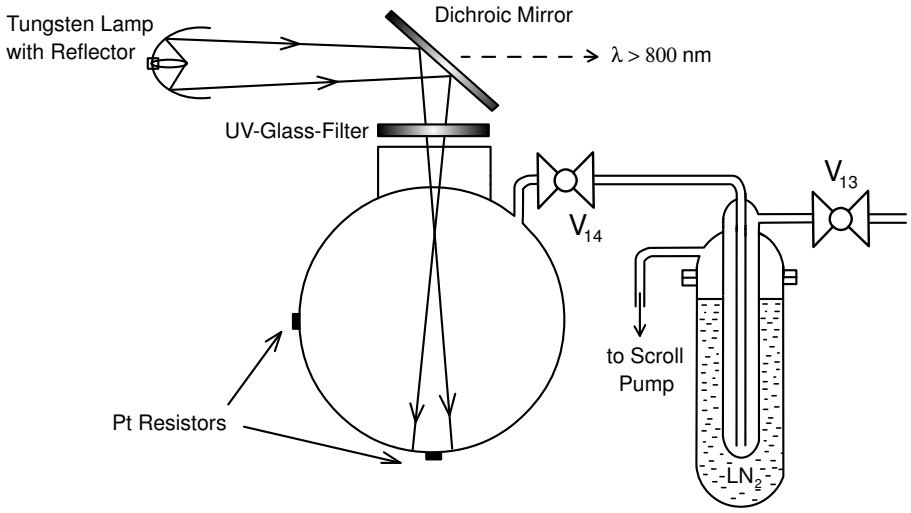

Figure 4.3.: Scheme of the photolysis reaction cell (PRC). The tungsten filament is mounted into an Oriel (Type 60125) lamp housing, which can be cooled by circulating water around the mount. The space between the parabolic reflector and the dichroic mirror is ventilated by a fan. Switching on the tungsten lamp about 2 minutes before the recycling experiment assured a stable light intensity during the photolysis recycling. During the lamp warming time the PRC entrance window was covered by a shutter to avoid unwanted illumination of the O_2-O_3 mixture. Typical lamp power supply settings were: $I = 10\,\mathrm{A}$ and $U = 13.3 \pm 0.3\,\mathrm{V}$.

Small amounts of ozone (up to $40\,\mu$mol) were produced from natural molecular oxygen using silent electric discharge. This took place in the cold trap T_2 that was immersed in liquid nitrogen to a level of about 2 cm above the electrodes. During the discharge, the oxygen gas pressure is monitored with a 10 Torr Baratron pressure gauge (B_3). As ozone forms in the electric discharge it freezes out and the gas

pressure decreases. When about 80 % of the initial O_2 is converted[1] to ozone the electric discharge is turned off and the residual O_2 is pumped away.

The condensed ozone is then brought to room temperature and transferred to the photolysis reaction cell (PRC), which is placed into a dewar filled with destillated water to maintain a stable temperature. The temperature is monitored with two self calibrated platinum resistors mounted on the outside wall of the PRC. One sensor is attached to the bottom of the sphere at which point the incident light power is expected to be at its maximum. The second sensor is placed about half way between the bottom of the glass sphere and the point where the light enters. Great care was taken to estimate gas phase temperatures. It was verified that there was no temperature gradient across the walls of the glass sphere during VIS light illumination. To that purpose the pressure in the sphere was monitored before and after the light source has been switched on and off in a series of control experiments. The associated pressure changes agreed well with the temperature changes of about 0.1 K measured at the outside with the middle position sensor, and thus demonstrated that the thermometers recorded meaningful measures of the bath gas temperature. A small flow of nitrogen gas was used to stir the water bath and minimize temperature gradients in the bath.

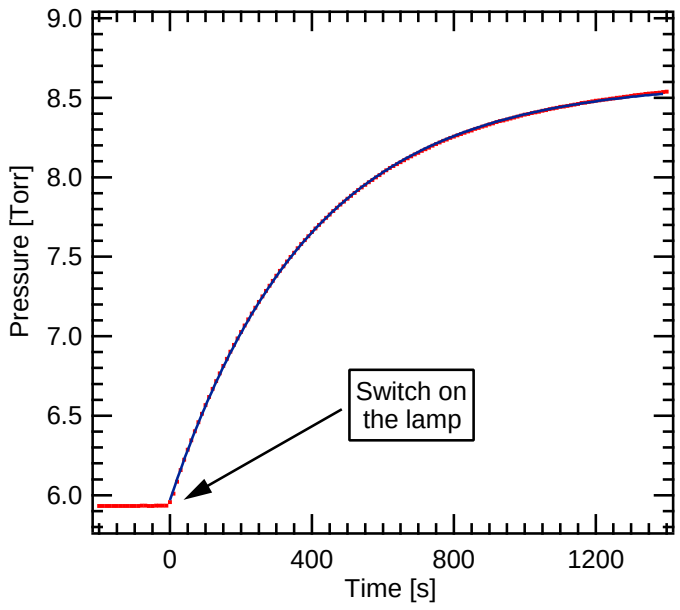

Figure 4.4.: Experimental determination of the ozone photolysis rate. The pressure increase due to the photolytic dissociation of ozone is plotted as a function of time. Note that the time constant for the observed pressure change actually reflects the contribution of two different ozone destruction processes: $O_3 + h\nu \rightarrow O_2 + O$ followed by $O_3 + O \rightarrow 2O_2$. Therefore, the 1/e time of 5.7 min resulting from the exponential fit performed on the data points represents twice the photolysis rate: $2J = 1/t_{1/e}$. Hence, a photolysis rate of $J = 1.46 \times 10^{-3}\,s^{-1}$ is derived.

Ozone pressure in the PRC is up to 350 mTorr. This amount of ozone is diluted in natural molecular oxygen (the same used to produce ozone) of about 40 - 70 Torr (see Table 4.4). After closing the PRC, the tungsten lamp is switched on. A UV-glass-filter (*Schott*, GG420) in combination with a dichroic mirror (transmittance higher

[1] The extent of reaction was calculated from the pressure change in the reaction volume by $C(\%) = [(P_i - P_f)/P_i] \times 100$, where P_i represents the initial O_2 pressure and P_f the final pressure at which the discharge was stopped.

than 97 % at 400-700 nm and less than 10 % at $\lambda > 800$ nm) is used to filter out the UV radiation and to reduce heating from IR (see Figure 4.3).

The temperature was stable over the whole photolytic recycling process of typical 6-7 recycling times. The recycling time[1] was determined in repeated "blank" experiments, where an amount of $\sim$ 6 Torr pure ozone was introduced into the PRC and photolyzed. The ozone pressure was monitored with a 10 Torr Baratron pressure gauge (B_4) and the values were recorded at 1 s time interval. After the tungsten lamp is switched on, the pressure increases in an exponential fashion, as shown in Figure 4.4.

The complete scheme of reactions in the PRC is summarized and listed in Table 4.2. Photolysis of ozone (R1)[2] leads to formation of oxygen atoms and molecules, both in their electronic ground states. Reaction between oxygen atoms and molecules can result either in a new ozone molecule (R2) or in isotope exchange products (R3a, R3b). Ozone from (R2) may react with atomic oxygen to form O_2 in reaction (R4).

Under the experimental conditions, oxygen wall reactions (R6) are much slower than the gas phase reactions (R2) - (R4). The oxygen isotope exchange reactions (R3a, R3b) are at least 10^4 times faster than the formation of ozone molecules (R2). Therefore, the rate at which atoms are recycled through molecular oxygen is at least 10^4 times the rate at which atoms actually react to form ozone. The different time scales for isotope exchange and ozone formation reflect that the atom-diatom recombination to form ozone occurs in its low pressure regime. In terms of the energy transfer mechanism a dynamic equilibrium between association, exchange and redissociation of the excited molecule is reached.

Atomic oxygen formed in reaction (R1) is mostly consumed in the reactions (R2) and (R4). While in the first reaction the odd oxygen concentration is preserved, reaction (R4) implies a loss channel for atomic oxygen. Combining reaction (R1) with (R4), it is easy to see that the net result is conversion of ozone to molecular oxygen: $2O_3 \rightarrow 3O_2$. Therefore, long photolysis times result in a decrease of the initial O_3. Under the experimental conditions the atomic oxygen that will be lost in reaction (R4) relative to reaction (R2) is small:

$$\frac{k_{O+O_3}[O][O_3]}{k_{O+O_2}[O][O_2]^2} \approx 0.023 \tag{4.3}$$

Blank experiments assured that other possible interfering reactions had negligible effects. Before the experiments, the PRC internal walls were repeatedly conditioned with pure ozone at pressures up to 20 Torr.

Following the photolytic recycling process, the gas mixture of molecular oxygen and ozone flew slowly trough the pyrex cryo-trap (T_4) that had a temperature of about 63 K. This temperature was achieved by pumping on the closed dewar, which contains the LN_2 bath. A pressure regulator adjusts the N_2 gas pressure above the liquid until the trap temperature is close to the triple point of N_2, *i.e.* 63.15 K. At this temperature the ozone vapor pressure is less than 10^{-5} Torr.

[1] Defined as the time needed for reforming (1 - 1/e) of the original O_3

[2] For the numbering of reactions see Table 4.2

Table 4.2.: Kinetic and diffusional timescales of ground state oxygen chemistry. Table adopted from *Janssen* [2004]

		Reaction	Coefficient[a]	Lifetime of atoms (s)[b,c,d]	Ref.
(R1)	$O_3 + h\nu$	$\longrightarrow O + O_2$	$1.46 \cdot 10^{-3}\,s^{-1}$		*e*
(R2)	$O + O_2 + M$	$\longrightarrow O_3 + M$	$6.0 \cdot 10^{-34}\,cm^6\,s^{-1}$	$2.0 \cdot 10^{-2}$	*f*
(R3a)	$^{18}O + {}^{16}O_2$	$\longrightarrow {}^{16}O^{18}O + {}^{16}O$	$2.9 \cdot 10^{-12}\,cm^3\,s^{-1}$	$1.2 \cdot 10^{-6}$	*g*
(R3b)	$^{17}O + {}^{16}O_2$	$\longrightarrow {}^{16}O^{17}O + {}^{16}O$			
(R4)	$O + O_3$	$\longrightarrow 2\,O_2$	$8.0 \cdot 10^{-15}\,cm^3\,s^{-1}$	$1.1 \cdot 10^{-1}$	*f*
(R5)	O + wall	$\longrightarrow$ products	$220\,cm^2\,s^{-1}\,(p/\mathrm{Torr})^{-1}$	$8.2 \cdot 10^{0}$	*h*
(R6)	O_3 + wall	$\longrightarrow$ products			*i*

[a] Rate (k, J) or diffusion (D) coefficient at 300 K
[b] Chemical lifetimes are defined as time constants of pseudo first order decay.
[c] Diffusional lifetimes are approximated by $4R^2/(\pi^2 D)$. They place a lower limit on the characteristic time scale for heterogenic loss.
[d] Typical parameters: $[O_2] = 2.9 \cdot 10^{17}\,cm^{-3}$, $[O_3] = 1.1 \cdot 10^{15}\,cm^{-3}$, spherical volume, $R = 8\,cm$.
[e] Experimentally determined
[f] *DeMore et al.* [1997]
[g] *Anderson et al.* [1985]
[h] *Morgan and Schiff* [1964]
[i] Dark experiments resulted in ozone wall lifetimes of about one day, rending these process negligible.

Therefore, final ozone pressures in the PRC of as little as 0.1 mTorr can be collected with 95 % efficiency. This is sufficient to make errors due to isotope effects in the collection process negligible. Thus, ozone is completely collected, while the molecular oxygen is pumped away. Immediately after the pressure in the vacuum system drops below 10^{-5} Torr, the pumping is stopped and the ozone is evaporated by replacing the cold trap with a water bath. The evaporating ozone then expands into the multipass cell. Enough time is given for diffusion to isotopically homogenize the ozone sample within these volumes. After closing the valve in front of the multipass cell, the remaining ozone is completely frozen back into a steel cold finger (not shown in Figure 4.1) immersed in liquid helium. This part of the ozone sample is left to decompose into molecular oxygen. By measuring the isotope composition of this O_2 with the mass spectrometer, the isotopologue fractionation values of the original ozone samples are determined. Mass balance requires that the isotope fractionation signature of ozone isotopologues with a natural isotopic abundance is conserved in the molecular oxygen to which the ozone has decomposed [*Klees*, 1994]. Explicitly,

$$^{49}E \approx {}^{33}E \qquad \text{and} \qquad {}^{50}E \approx {}^{34}E \tag{4.4}$$

where

$${}^{i}E(\%) = \left(\frac{{}^{i}X_{SM}}{{}^{i}X_{S}} - 1 \right) \times 100 \qquad i = 33, 34 \tag{4.5}$$

are the isotopic enrichments of the molecular oxygen resulted from ozone decomposition. This way, the determination of the ozone isotopologue fractionation is reduced

to the measurement of the isotopic composition of an O_2 gas that can be performed with relatively high precision. This approach is sufficient and accurate when using natural oxygen for ozone production. The small abundance of the heavy isotopes ^{17}O and ^{18}O in natural O_2 ensures that only the molecules $^{16}O^{16}O^{17}O$, $^{16}O^{17}O^{16}O$, $^{16}O^{16}O^{18}O$ and $^{16}O^{18}O^{16}O$ will contribute significantly to masses 33 and 34 u.

4.2.3. Ozone Photolytic Dissociation

Though in the first photolytic recycling experiments [*Morton et al.*, 1990] no evidence of additional isotopic fractionation during the ozone VIS photolysis has been found, later experiments [*Chakraborty and Bhattacharya*, 2003; *Wen and Thiemens*, 1991] indicate that photodissociation of ozone may produce isotopically light oxygen with respect to the initial ozone. The possibility of a photodissociation effect on the isotopic composition of ozone and the obviously conflicting literature data motivated a set of four control experiments, in which ozone was photodissociated by visible light.

In these experiments ozone of about 127 μmol was prepared from molecular oxygen in a silent electric discharge. The generated ozone was introduced into the PRC, the valve V_{14} was closed, and the left over ozone was pumped away. When the pressure level in the vacuum system dropped below 10^{-7} Torr, the ozone from the PRC was expanded into the volume EV_2 that served as an aliquot of the initial ozone. After 1-2 minutes, EV_2 and the PRC were closed and the vacuum system evacuated.[1] Following the procedure already described in the previous section, the pure ozone sample in the temperature stabilized PRC has been photolyzed for up to 12 minutes. The photolysis was kept short enough to assure, on one hand, that ozone photodissociation (R1) together with the subsequent ozone destroying reaction (R4) are the dominating reactions, and, on the other hand, that the amount of left over ozone was still large enough for spectroscopic investigation.

4.2.4. Ozone Formation by Electric Discharge

As early as 1845, *de la Rive and de Marignac* observed ozone formation from pure O_2 due to the effect of an electric discharge [*Horváth et al.*, 1985]. The first demonstration of a chemically produced mass independent isotopic fractionation has also been performed using ozone generated from molecular oxygen in an electric discharge (details already presented in the introductory part of this work).

In spite of the fact that oxygen being a frequently studied medium in gas discharges, the complete scenario of the physico-chemical processes, which take place in the discharge volume remains still a complicated issue. A simplified list of the main reactions that govern the ozone formation in a silent discharge is given in Table 4.3, where the reactions with charged- as well as with the large number of excited state species were not considered.

[1] Several blank experiments assured that no change in the isotopic composition of the ozone sample took place during these gas handling procedures. Mass spectrometric measurements showed the same isotopic ratios for the samples taken from EV_2 and PRC.

Table 4.3.: Reactions that govern the ozone formation in a silent discharge. Only neutral species are considered.

	Reaction			Rate coefficient [a]
(R1a)	$e + O_2$	$\rightarrow$	$O + O + e$	$f(E/N)$ [b]
(R1b)		$\rightarrow$	$O + O(^1D) + e$	$f(E/N)$
(R1c)		$\rightarrow$	$O_2(^1\Delta_g) + e$	$f(E/N)$
(R2)	$O + 2O_2$	$\rightarrow$	$O_3 + O_2$	$6 \times 10^{-34} \exp(300/T)$
(R3)	$O + O + M$	$\rightarrow$	$O_2 + M$	
(R4a)	$O + O_3$	$\rightarrow$	$2O_2$	$1.8 \times 10^{-11} \exp(-2300/T)$
(R4b)		$\rightarrow$	$O_2 + O_2(^1\Delta_g)$	$10^{-11} \exp(-2300/T)$
(R5)	$O_2(^1\Delta_g) + O_3$	$\rightarrow$	$2O_2 + O(^1D)$	10^{-11}
(R6a)	$O(^1D) + O_3$	$\rightarrow$	$O_2(^1\Delta_g) + O_2$	2.7×10^{-10}
(R6b)		$\rightarrow$	$O_2 + 2O$	1.2×10^{-10}
(R6c)		$\rightarrow$	$2O_2(^1\Delta_g)$	
(R7a)	$O_2(^1\Sigma_g^+) + O_3$	$\rightarrow$	$2O_2 + O$	1.5×10^{-11}
(R7b)		$\rightarrow$	$O_2 + O_3$	2.2×10^{-11}
(R8a)	$e + O_3$	$\rightarrow$	$O(^1D) + O_2(^1\Delta_g) + e$	$f(E/N)$
(R8b)		$\rightarrow$	$O + O_2 + e$	$f(E/N)$
(R9)	$O_2(^1\Delta_g) + e$	$\rightarrow$	$O_2 + e$	$f(E/N)$
(R10)	$O_2(^1\Delta_g) + \text{Wall}$	$\rightarrow$	$O_2 + \text{Wall}$	$(R^2/8D) + (2R/\gamma v)$ [c]
(R11)	$2O_2(^1\Delta_g) + O_2$	$\rightarrow$	$2O_3$	10^{-31}
(R12)	$O(^1D) + O_2$	$\rightarrow$	$O + O_2$	$7.0 \times 10^{-12} \exp(67/T)$
(R13)	$O + \text{Wall}$	$\rightarrow$	$\frac{1}{2}O_2 + \text{Wall}$	$(R^2/8D) + (2R/\gamma v)$
(R14)	$Q + O_2$	$\rightarrow$	$OQ + O$	$2.9 \times 10^{-12} \exp(300/T)$

[a] The reaction rate constants are expressed in cm^3s^{-1} for two-body reactions, and in cm^6s^{-1} for three-body reactions.

[b] These rate constants are a function of electric field/reactant concentration (E/N).

[c] Here a cylindrical geometry for the discharge tube has been considered, R is the radius of the discharge tube, D is the diffusion coefficient, γ the recombination coefficient and v the mean velocity of the species.

Typically, the first step in the discharge kinetics is the dissociation of molecular oxygen by electron collisions. Starting from electron impact on ground state O_2 molecules two reaction paths leading to dissociation are available: via excitation of the $A^3\Sigma_u^+$ state with an energy threshold of about 6 eV (R1a) and via excitation of the $B^3\Sigma_u^-$ state at 8.4 eV (R1b). Direct ionization of O_2 also takes place. Ozone is mainly formed in the three-body reaction (R2), involving O and O_2. Side reactions (R3), (R4a,b) and (R12) of O atoms compete with ozone formation . The main contributions to ozone decomposition are collisions with atomic oxygen like in (R5), (R6a,b,c) and (R7a,b) or with electrons (R8a,b). Electrons with energies of 1.2 to 2 eV can lead to the production of O and vibrationally excited O_2^- by attachment to ozone [*Allan et al.*, 1996].

Also, self-emitted light (200-300 nm) in the oxygen discharge can cause ozone to be dissociated through two significant photodissociation reactions [*Slanger et al.*, 1988]

$$\begin{aligned} O_3 + h\nu &\rightarrow O(^1D) + O_2(A^1\Delta_g) \\ &\rightarrow O(^3P) + O_2(X^3\Sigma_g) \end{aligned}$$

The density of oxygen atoms produced in the discharge decreases due to the recombination processes. There are two main possible channels: three-body collisions (R2) in the volume or surface recombination (R13). Note that at low pressures (few Torr), the rate for three-body recombination is small compared to that for surface recombination. The surface recombination probability of oxygen atoms as a function of wall temperature has been studied by *Macko et al.* [2004] using a double pulse discharge technique. They found that the wall recombination probability γ on a Pyrex surface ranges from 4.0×10^{-4} to 1.6×10^{-2} for wall temperatures from 77 to 460 K. (At 300 K, the recombination probability is $\gamma = (2.0 \pm 0.5) \times 10^{-3}$.)

The heat source is mainly due to the O_2 dissociation that can be expressed as

$$Q_e^{diss} = [(6 - 5.1)k_{diss(6\,eV)} + (8.4 - 5.1 - 1.98)k_{diss(8.4\,eV)}][O_2]n_e \qquad (4.6)$$

in the units eV cm^{-3} s^{-1}, where $k_{diss(6\,eV)}$ and $k_{diss(8.4\,eV)}$ are the rate constants for dissociation through the 6 eV and the 8.4 eV channels, respectively. The numerical factors multiplying these rate constants are the kinetic energies acquired by the atoms after the corresponding dissociation process. Note that the dissociation energy of O_2 is 5.1 eV, while 1.98 eV is the energy of the electronic state $O(^1D)$ produced in the 8.4 eV dissociation channel. Both of these channels contribute directly to gas heating due to the production of hot atoms with kinetic energies of 1.3 eV and 0.9 eV, respectively.

The atom's thermal velocity can be ten to a hundred times smaller than the electron's velocity (20.000 m/s for a 1 eV electron). This translates into atom temperatures of several hundred °C. Generally, in low pressure discharges, the neutral atoms and ions are not in equilibrium with the electrons, and the rates for collisional energy transfer between the two groups depends on the electron density and the electron energy distribution.

Long living active species (metastable states, radicals, atoms of molecular gases) do not lose their internal energy by radiative emission in a few nanoseconds, so they can diffuse and react in the volume and on walls. Exothermic reactions at the wall such as recombination of oxygen atoms and quenching of $O_2(^1\Delta_g)$ molecules may contribute appreciably to gas heating. Thus, the temperature where the ozone is formed is not well defined.[1]

Clearly, the investigation of the isotope fractionation of ozone that is generated in electric discharge has several drawbacks. First of all, the reaction kinetics in which the ozone molecules are involved is very complex due to the large number of different species (charged, excited- and metastable states, etc.) and, therefore, a molecular level assignment of the observed isotopic fractionation is difficult. The second limitation is in the determination of the temperature itself. Due to the presence of several heat sources the temperature at which the ozone is formed cannot accurately be determined.

[1] Instantaneous local temperature rise may also cause a significant dissociation of ozone molecules.

4.2.4.1. Heterogeneous Ozone Formation

It has been observed in natural oxygen that depending on discharge chamber dimensions, the isotope enrichments may diminish toward lower pressures [*Bains-Sahota and Thiemens*, 1987; *Morton et al.*, 1990]. Past studies [*Janssen*, 1999; *Krohn*, 1998] have explained the observed pressure dependence by diffusional processes in combination with an isotope neutral ozone formation reaction at the surface. The key assumptions in the Monte-Carlo simulations [*Krohn*, 1998] as well as in the analytical calculations [*Janssen*, 1999] are that ozone formation occurs by oxygen ground state chemistry only and that the rate limiting step is in the transport of atomic oxygen to the walls. Nevertheless, the atomic oxygen can be fractionated by isotope exchange reactions and isotope dependent diffusion rates. These isotope effects actually result in a mass-dependent ($\delta^{17}O = 0.5\ \delta^{18}O$) depletion of the heavy ozone isotopologues. Furthermore, because the fractionation exclusively occurs in the atoms, it is expected that the observed depletion completely resides in the asymmetric molecules.[1]

Therefore, the total depletion $E_{u(w)}$ measured with the mass spectrometer

$$3E_{u(w)} = 2E^a_{u(w)} + E^s_{u(w)} \tag{4.7}$$

is completely due to the depletion of the asymmetric species, which implies

$$E^a_{u(w)} = \frac{3}{2}E_{u(w)} \tag{4.8a}$$

$$E^s_{u(w)} = 0 \tag{4.8b}$$

with $E_{u(w)}$, $E^a_{u(w)}$ and $E^s_{u(w)}$ defined as:

$$E_{u(w)} = \frac{([{}^{u}O_3]/[{}^{48}O_3])_{obs}}{([{}^{u}O_3]/[{}^{48}O_3])_{stat}} - 1\,, \tag{4.9a}$$

$$E^a_{u(w)} = \frac{([{}^{16}O{}^{16}O{}^{x}O]/[{}^{16}O_3])_{obs}}{([{}^{16}O{}^{16}O{}^{x}O]/[{}^{16}O_3])_{stat}} - 1\,, \tag{4.9b}$$

$$E^s_{u(w)} = \frac{([{}^{16}O{}^{x}O{}^{16}O]/[{}^{16}O_3])_{obs}}{([{}^{16}O{}^{x}O{}^{16}O]/[{}^{16}O_3])_{stat}} - 1 \tag{4.9c}$$

where ${}^{x}O$ can be ${}^{17}O$ or ${}^{18}O$, and ${}^{u}O_3$ represents the ${}^{49}O_3$ and ${}^{50}O_3$ isotopologues, respectively. The index "obs" stands for the observed isotopologue ratio in ozone, in the present case ozone produced in low-pressure electric discharge (w), and "stat" means the same ratio as statistically calculated from the composition of the scrambled oxygen gas. Denoting the atomic ratio by $r = {}^{x}O/{}^{16}O$, the statistical expectation is simply given by $([{}^{u}O_3]\,/\,[{}^{16}O_3])_{stat} = 3r$, $([{}^{16}O{}^{16}O{}^{x}O]\,/\,[{}^{16}O_3])_{stat} = 2r$ and $([{}^{16}O{}^{x}O{}^{16}O]\,/\,[{}^{16}O_3])_{stat} = r$, respectively.

[1] It was experimentally demonstrated that ozone formation in homogeneous [*Janssen et al.*, 1999] and heterogeneous reactions proceeds end-on [*Bahou et al.*, 1997], *i.e.* only the asymmetric molecules ${}^{16}O{}^{16}O{}^{18}O$ and ${}^{16}O{}^{16}O{}^{17}O$ will be influenced by the fractionation of atomic oxygen.

In the context of the present work, heterogeneously formed ozone gains its special importance from the lack of an available standard with quantified amounts of symmetric and asymmetric molecules. Such a standard is, however, required when the isotopomeric composition of ozone is to be investigated by a spectroscopic technique. Only if the line strengths of these species are known to within about 1 % accuracy – which requires the preparation of a calibration mixture, because theoretical calculations cannot yet reach this level of accuracy for ro-vibrational transitions – the relative amounts of the two symmetry species can be determined with the same accuracy by using the Beer-Lambert law. Therefore, preparation of ozone under low pressure conditions with relatively small and supposedly well-known isotopic effects offers a convenient way of preparing a calibration mixture, where the relative amounts of asymmetric and symmetric molecules are known with sufficient precision.

4.2.4.2. Ozone Formation in High Pressure Electric Discharge

Laboratory measurements [*Bains-Sahota and Thiemens*, 1987; *Morton et al.*, 1990] have shown that the anomalous isotopic fractionation of ozone, independently whether it is formed in photolytic recycling or in electric discharge, is pressure dependent. Oxygen photolysis carried out at pressures between 0.8 and 87 atm led to the key observation that the isotope enrichment disappears at pressures around 55 atm [*Thiemens and Jackson*, 1990]. But there is clearly a plateau at some pressure range[1] where the enhancement of $^{49}O_3$ and $^{50}O_3$ has a constant value. Above and below this plateau region, the enhancements decrease. The reproducibility of enrichments when ozone samples are produced in high-pressure electric discharge requires the selection of adequate pressure values in the above mentioned plateau region.

4.2.4.3. Experimental Procedure

The experimental apparatus employed for ozone generation in an electric discharge is schematically shown in Figure 4.5. Ozone is prepared in a glass tube using a silent electric discharge in a molecular oxygen flow. The flow into the system is maintained at a constant rate by adjusting either the O_2 flux with the metal valve (MV_2) or by varying the pump rate of the sorption pump. The two possibilities have been combined to assure a maximum flow rate in the discharge volume for a given pressure. The gas flow rate is monitored by an MKS flow-meter (100 sccm full scale). When the desired O_2 gas pressure at a stable flow rate is achieved, the high voltage generator is switched on and the voltage is slowly increased until an electric discharge between the two ring-electrodes (see Figure 4.5) is ignited. The discharge[2] takes place in the space between the electrodes.

[1] The exact pressure region of this plateau will depend on temperature and the geometry of the discharge chamber.

[2] Depending on the gas pressure in the glass tube one can have diffuse glow discharges referred to as RF glow discharges (for pressures typically below 1 Torr) or filamentary plasma formation at higher pressures.

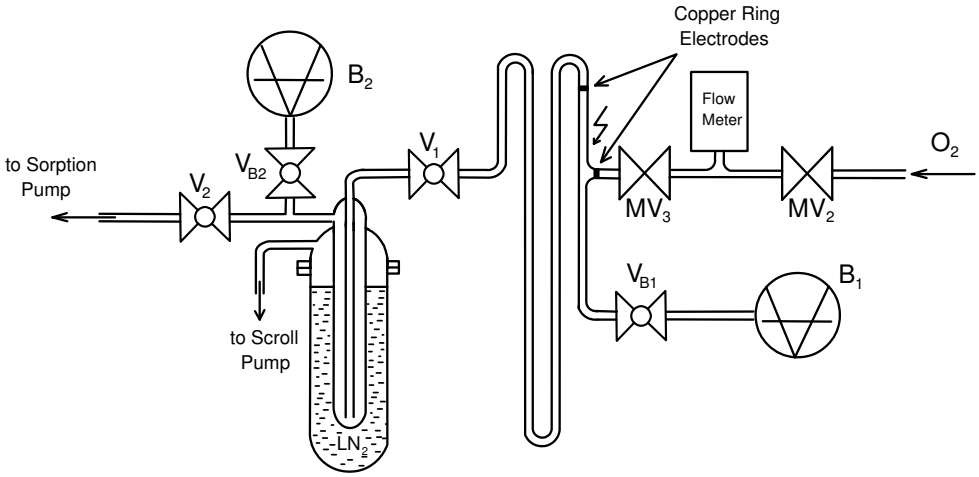

Figure 4.5.: Flow reactor used for ozone generation in electric discharge. The "U-shape" glass tube is about 75 cm long. The copper ring electrodes are fixed on the exterior walls of the tube at 6 cm (for high-pressure discharge) or 12 cm (for low-pressure discharge) apart from each other.

Oxygen atoms generated by the discharge can, among other side reactions, recombine with O_2 molecules, producing ozone that is removed from the discharge volume by the background oxygen flow. The long (about 75 cm) "U-shape" glass tube assures that any such kind of recombination takes place at temperatures higher (in the discharge) or close to the room temperature (glass walls). Thus, the uncertainty in the temperature at which ozone is formed can be shrunk to much narrow limits. The ozone formation at room or higher temperatures will lead to higher enrichments of the ozone isotopologues in the high pressure regime, and to smaller depletions of the asymmetric ozone isotopologues in the low pressure regime, respectively.

A series of runs were performed in order to clearly identify for the existing reactor geometries those pressure ranges where 1) ozone is formed exclusively in heterogeneous reactions (low-pressure), *i.e.* where the mass-dependent depletions of the heavy ozone isotopologues take place, and 2) the ozone gas phase formation happens right at the pressure where the enrichments of the ozone isotopologues have a constant value.

For the first case a pressure range between 650–800 mTorr, while for the second a pressure of about 110 Torr has been experimentally determined. The lower value of the low-pressure regime was limited by the fact that for the TDLAS measurements, regarding the rare $^{16}O^{16}O^{17}O$ and $^{16}O^{17}O^{16}O$ isotopomers, a minimum amount of ~ 80 mTorr ozone in the 3.2 l multipass cell is necessary to obtain accurate ($< 1\,\%$) linestrength values. But a low O_2 pressure automatically means low amounts of generated ozone, *i.e.* longer sampling time. The hold time of LN_2 in the cold trap is limited to about 4 hours, *i.e.* the lowest pressure for O_2 should be at least 650 mTorr to allow for the necessary amount of ozone to be generated.

4.3. Mass Spectrometric Analysis

Eight ozone samples, mostly generated under the same conditions, have been prepared in photolytic recycling, four experiments were dedicated to the investigation of the isotope effects in the photodissociation of ozone and finally, five and eighteen ozone samples were prepared in electric discharge at high and low pressure, respectively. Here, the results of the mass spectrometric investigation of these samples are presented. First, the ozone samples produced in the photolytic recycling are considered.

Table 4.4.: Experimental conditions in the photolytic recycling experiment.

Sample Date / #	P_{O_3} in PRC (Torr)	P_{O_2} in PRC (Torr)	Photolysis Time (min)	Temperature (K)	P_{O_3} in MPC (Torr)
14.06.04 / 1.	0.334	52.7	60	-	0.124
15.06.04 / 2.	0.250	49.5	90	-	0.087
18.06.04 / 3.	0.249	49.8	75	292.8 ± 0.7	0.089
20.07.04 / 4.	0.280	46.3	80	298.9 ± 0.3	0.091
23.07.04 / 5.	0.273	45.1	80	294.5 ± 0.6	0.089
29.07.04 / 6.	0.329	64.4	90	293.9 ± 0.8	0.123
02.08.04 / 7.	0.352	69.5	90	296.8 ± 0.4	0.130
28.10.04 / 8.	0.312	69.4	75	292.2 ± 0.1	0.121

Besides the controlling parameters like O_2 pressure and bath temperature, the photolysis time, initial- and final ozone concentration are listed in Table 4.4.

Table 4.5.: Measured $^{49}O_3$ and $^{50}O_3$ fractionations and comparison with available data. In the last line the average values $\bar{E}$ together with their standard deviations are given.

Sample #.	Present work ^{49}E (%)	Present work ^{50}E (%)	Experimental values ^{49}E (%)	Experimental values ^{50}E (%)	Ref.
1.	10.3	11.6	11.3 ± 1.0	13.0 ± 1.0	*a*
2.	9.8	11.1	10.4 ± 0.6	12.3 ± 0.6	*b*
3.	10.0	11.2	10.6 ± 0.4	13.0 ± 0.3	*c*
4.	10.2	12.1	–	12.4 ± 0.8	*d*
5.	9.9	11.5			
6.	9.8	10.9			
7.	10.4	10.9			
8.	10.2	10.3			
$\bar{E}$	**10.1(2)**	**11.2(5)**			

For the present work an average temperature of 295 K is used.

[a] *Mauersberger et al.* [1999]. No distinct temperature is reported.

[b] *Morton et al.* [1990] at 321 K

[c] *Wolf et al.* [2000] at 300 K.

[d] *Janssen et al.* [2003] at 324 K

Mass spectrometric analysis has been performed on all samples, while TDLAS investigations were only done for the last four (from 5 to 8) samples. The enrichments measured with the mass spectrometer are listed in Table 4.5. For comparison purposes experimental data of measurements from the literature are also given. In order to make a quantitative comparison between the present measured ozone isotopologue fractionation values and those from the literature, the temperature dependency of ozone isotopologue fractionations needs to be considered. Figure 4.6 shows the temperature dependence of $^{49}O_3$ and $^{50}O_3$ fractionations based on the available data of experimental investigations [*Janssen et al.*, 2003; *Morton et al.*, 1990].

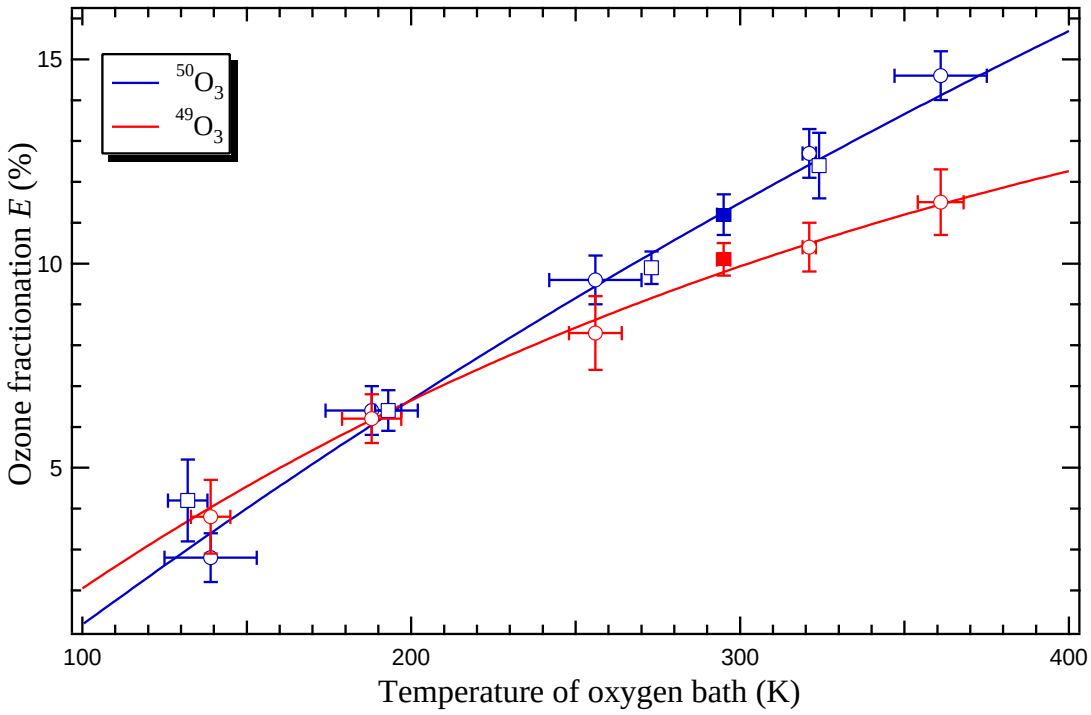

Figure 4.6.: Temperature dependence of $^{49}O_3$ and $^{50}O_3$ isotopologue fractionation. Open symbols represent data from *Morton et al.* [1990](○) and *Janssen et al.* [2003] (□). The values measured in this work are displayed as solid squares (■). The error bars represent $1\,\sigma$ uncertainties.

It should be mentioned that the temperature resolved measurements of *Morton et al.* [1990] have been performed with ozone samples that were produced under similar conditions as in this work. The good agreement between the measurements allows to assess the data quality. With regard to fractionation effects the differences in pressure conditions are negligible, because all the measurements of Table 4.5 were well in the low pressure region where the isotopologue enrichments have been shown to level off to a constant value (see later on page 55).

Now we turn to the investigation of the leftover ozone samples, which resulted from photolytic dissociation of ozone. The aim of this experiment is to identify potential isotopic effects related to the photolysis of ozone. In Table 4.6 the experimental conditions for the samples together with the measured enrichments are given.

Table 4.6.: Ozone samples from the photolytic dissociation experiments .

Sample Date / #	P_{O_3} in PRC (Torr)	Photolysis Time (min)	Temperature (K)	P_{O_3} in MPC (Torr)	^{49}E (%)	^{50}E (%)
14.10.04 / 1.	1.006	12	-	0.061	1.4	2.0
15.10.04 / 2.	0.815	10	-	0.075	0.6	2.6
22.10.04 / 3.	0.809	8	292.6 ± 0.1	0.110	0.7	1.0
26.10.04 / 4.	0.803	9	293.2 ± 0.2	0.092	1.3	2.2

While the isotopic composition of the initial ozone as well as the ozone left after the photodissociation has been analyzed by means of MS, the last sample (4) was also investigated by TDLAS. The instantaneous fractionation factor α for the combined (dissociation and ozone destruction) process was calculated based on the experimentally determined photolysis rate J and the measured fractionation of the leftover O_3. The average value for $^{50}O_3$ is given in Table 4.7 together with experimental values found in the literature.

Table 4.7.: Comparison of the measured instantaneous fractionation factor α of $^{50}O_3$ with available data. The δ values are normalized to the initial ozone isotopic composition.

Parameter	1[a]	2[b]	3[c]
α	-	1.0151	1.011
$\delta^{17}O/\delta^{18}O$	0.53	0.54	0.51

[a] *Wen and Thiemens* [1991]. Light source: Nd YAG laser at 532 nm.
[b] *Chakraborty and Bhattacharya* [2003], Light source: tungsten lamp with two different interference filters that transmit at 520 nm and 630 nm, respectively.
[c] This work

The current experimental results indicate that decomposition effects are significantly smaller in magnitude than isotope fractionation during ozone formation. Nevertheless, ozone photodissociation may contribute to the observed isotope fractionations with about 0.5 % and 1 % for the $^{49}O_3$ and $^{50}O_3$ isotopologues, respectively.

At present it is not clear whether this isotopic effect is associated only to the photolysis step $O_3 + h\nu$ or whether there is a contribution from the consecutive ozone destruction reaction $O_3 + O$, too. In the photolytic decomposition experiment half of the ozone is destroyed by the former reaction and the other half by the latter reaction. Hence the experiment puts an upper limit of 2 % on the isotope effects of ozone photolysis in the Chappuis band. However, this additional isotope effect has to be considered when the rate coefficients of the ozone formation reaction channels are calculated.

Finally, the ozone samples that were generated in molecular oxygen flow by electric discharge are listed in Table 4.8. This table also includes the parameters characterizing the electric discharge flow system: the range of O_2 pressures that enter in the discharge volume (P_i) and the pressure measured after the cold trap (P_f), the flow rate, the ozone sampling times and the current-voltage settings of the high frequency voltage generator.

The isotope fractionation values measured with the mass spectrometer are plotted in Figure 4.7 along experimental values taken from *Janssen* [1999]. It should be noted that, except for the reaction chamber geometry, the flow system parameters were similar in both studies. Mass spectrometric investigation of the low pressure ozone samples, however, shows that the concept of heterogeneous ozone formation is only partly able to explain the present observations. Even though the high pressure enrichments agree very well with earlier studies, and even though a similar pressure dependence is observed, there is an obvious deviation from the standard relation $\delta^{17}O = 0.5\ \delta^{18}O$ in the low-pressure data, indicating that the simple model outlined in the previous section (see page 45) cannot completely account for the observations.

Presently the source of the observed discrepancy is unknown. An instrumental artifact can be ruled out from a comparison with a high precision isotope ratio mass spectrometer. Possibly, there are additional yet unidentified reactions that influence the isotopic composition of ozone, as is observed under discharge conditions at high pressures.

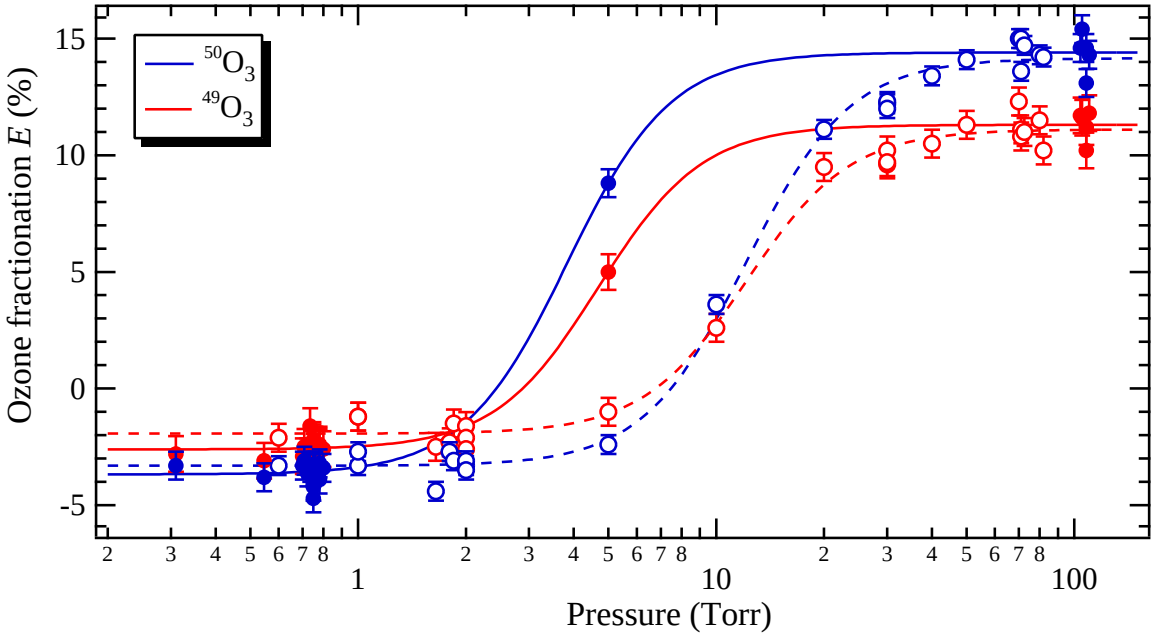

Figure 4.7.: Pressure dependence of $^{49}O_3$ and $^{50}O_3$ isotopologue fractionations. Open symbols represent data from *Janssen* [1999] (○). The values measured in this work are displayed as solid circles (●). The model correctly reproduces the observed pressure dependence and is able to quantitatively explain the observed depletions in the heavy isotopes.

The observed $\delta^{17}O/\delta^{18}O = 0.7$ adds the complication of how to interpret the TDLAS results and how to derive relative isotopomer abundances. In the light of past investigations, a pragmatic approach was chosen to address this problem without resolving the details of the kinetics. When there was no isotopic effect in the gas phase formation process a depletion of the heavy isotopomers is expected due to the effect of the atom isotope exchange reaction. This implies the exclusive depletion of asymmetric molecules in the absence of an isotope effect related to ozone formation in the gas phase (Section 4.2.4.1). The assumption that the asymmetric molecules are exclusively fractionated in the low pressure experiment, where obviously other effects than the ozone gas phase formation process are important, thus appears to be reasonable: $E^s_{u(w)} = 0$, $E^a_{u(w)} = 3/2E_{u(w)}$. Nevertheless, since this prediction must be incomplete, a fractionation in the symmetric molecules cannot be ruled out.

A reference material having isotopic composition that deviates from the above assumption obviously has an influence on the fractionation values measured by the TDLAS. Therefore, an analytical investigation has been performed to quantify the degree of this influence in different scenarios. A parameter β, which represents the fraction of the symmetric species contributing to the total enrichment, has been introduced into the Eqs. 4.8a and 4.8b, which become:

$$E^a_{u(w)} = \frac{3}{2}(1-\beta)E_{u(w)} \tag{4.10a}$$

$$E^s_{u(w)} = 3\beta E_{u(w)} \tag{4.10b}$$

$\beta = 0$ reproduces the standard case of the exclusive depletion of the asymmetric molecules. It is very unlikely that all the fractionation resides in the symmetric molecules ($\beta = 1$) because of several reasons: no physical or chemical process is known that seriously affects the symmetric molecules while it leaves the asymmetric molecules unchanged. Secondly, $\beta = 1$ would imply that the symmetric species in the ozone samples produced by photolytic recycling measured with the TDLAS are depleted (see also Figure 4.8). This is in conflict with the existing experimental results [*Anderson et al.*, 1989; *Janssen et al.*, 1999] as well as with theoretical predictions [*Gao and Marcus*, 2002; *Gao et al.*, 2002; *Schinke and Fleurat-Lessard*, 2005]. From these considerations the assumed limit-scenario was placed at $\beta = 1/3$ where the depletions are equally distributed amongst the isotopomers. In what follows it is shown that even $\beta = 1/3$ is too high, and implies the depletion of the symmetric molecules in ozone formation.

The symmetry specific enrichments, $E^a_{u(g/w)}$ and $E^s_{u(g/w)}$ are related to the reference material but can be normalized to the isotopic composition of the molecular oxygen (standard for the mass spectrometer measurements) simply by:

$$E^a_{u(g/s)} = E^a_{u(g/w)}(E^a_{u(w)} + 1) + E^a_{u(w)}\,, \tag{4.11a}$$

$$E^s_{u(g/s)} = E^s_{u(g/w)}(E^s_{u(w)} + 1) + E^s_{u(w)}\,, \tag{4.11b}$$

where $E^a_{u(w)}$ and $E^s_{u(w)}$ are given by Eqs. (4.10a) and (4.10b). We are interested in the variation of these normalized symmetry specific enrichments and also in the variation of the derived total enrichments as a function of the parameter β.

Figure 4.8 shows the β-dependence of derived enrichments. Interestingly, the total enrichment is almost independent from the isotopic composition of the reference material. Even in the upper limit-scenario ($\beta = 1/3$) the deviation is $\approx$ 0.23 %. This is clearly not the case for the normalized symmetry specific enrichments. The symmetric part is most strongly affected ($\approx 3.5\,\%$), followed by the asymmetric that varies by $\approx 2.1\,\%$.

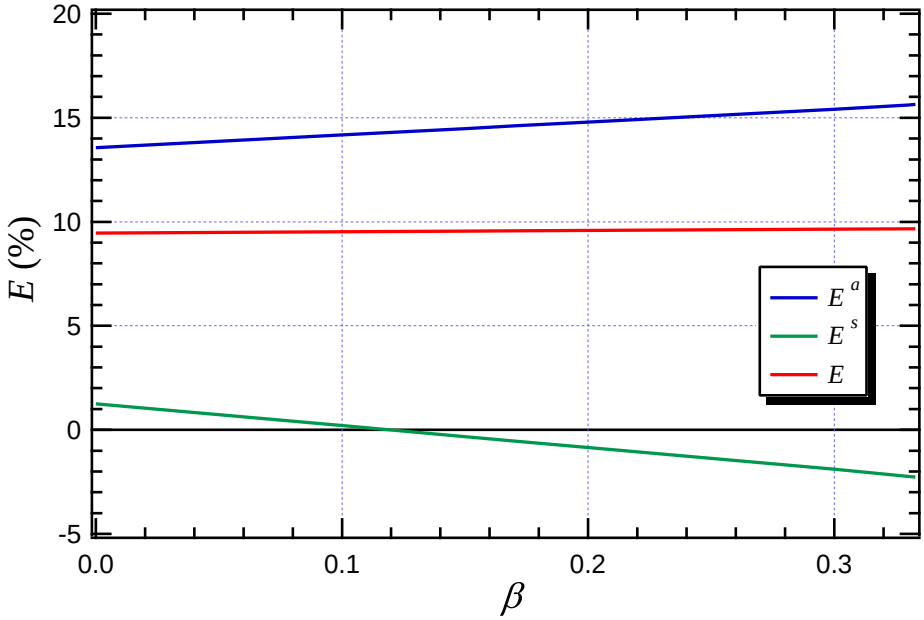

Figure 4.8.: Dependence of normalized symmetry specific enrichments (E_u^s and E_u^a) and the derived total enrichment (E_u) of the ^{18}O containing ozone (produced in photolytic recycling) on the isotopic composition of the reference material quantified by β (for definition see main text). Enrichment values are from Table 6.2 (page 79) by taking into account the additional isotope effect of ozone photodissociation (Table 6.3).

Based on this analysis it is concluded that independent of the isotopic composition of the reference material, the normalized total enrichments derived from the TDLAS measurements can be directly compared to the mass spectrometer results without introducing any substantial error. Furthermore, β cannot be higher than 0.12, otherwise the enrichment E_u^s of the symmetric species drops below zero. Assuming the standard case of $\beta = 0$, the uncertainties introduced by the above mentioned β-value to the enrichments of the different ozone isotopomers are: 0.74 % for $^{16}O^{16}O^{18}O$, 1.26 % for $^{16}O^{18}O^{16}O$, 0.54 % for $^{16}O^{16}O^{17}O$ and 0.92 % for $^{16}O^{17}O^{16}O$. They will be considered as additional 2σ systematic errors in the determination of the rate coefficients of ozone formation.

Table 4.8.: Ozone samples produced in electric discharge experiments.

Low-Pressure Discharge								
Sample Date/#	$P_i(O_2)$ (mTorr)	$P_f(O_2)$ (mTorr)	Flow (sccm)	Time (min)	U (kV)	I (mA)	E_{50} (%)	E_{49} (%)
03.06.04/ 1.	5007	3835	97.6	10	3.02	0.82	8.8	5.0
04.06.04/ 2.	546	368	4.8	45	2.03	0.46	-3.6	-2.9
07.06.04/ 3.	306	188	1.4	60	2.47	0.43	-3.8	-3.1
07.06.04/ 4.	711	356	7.9	60	3.15	0.57	-3.3	-2.8
09.06.04/ 5.	720	484	7.7	90	3.32	0.60	-3.1	-2.5
16.06.04/ 6.	792	507	11.1	95	3.31	0.63	-3.6	-2.9
17.06.04/ 7.	734	431	11.0	145	3.41	0.64	-3.4	-2.6
20.07.04/ 8.	760	404	12.1	140	2.92	0.60	-3.4	-1.6
23.07.04/ 9.[a]	740	350	11.0	150	3.46	0.64	-3.3	-2.4
29.07.04/10.[a]	750	430	11.5	150	3.13	0.63	-3.3	-2.9
02.08.04/11.[a]	740	430	11.0	150	3.24	0.63	-3.3	-2.4
04.08.04/12.	750	420	11.5	165	3.10	0.63	-3.4	-2.2
27.09.04/13.[a]	760	420	12.5	200	3.60	0.66	-3.4	-2.5
30.09.04/14.	770	398	12.6	200	4.15	0.78	-3.2	-2.4
28.10.04/15.[a]	742	354	13.2	180	4.00	0.73	-3.9	-2.5
12.11.04/16.[a]	740	380	13.2	170	3.88	0.77	-3.6	-3.1
18.11.04/17.	735	370	12.8	165	3.96	0.75	-4.7	-2.7
30.11.04/18.	780	350	13.4	180	-	-	-4.2	-2.3

High-Pressure Discharge								
Sample Date/#	$P_i(O_2)$ (Torr)	$P_f(O_2)$ (Torr)	Flow (sccm)	Time (min)	U (kV)	I (mA)	E_{50} (%)	E_{49} (%)
22.09.04/ 1.	105	101	99.5	3	7.50	1.31	15.4	11.6
27.09.04/ 2.[b]	105	102	97.4	2	7.46	1.44	14.6	11.7
30.09.04/ 3.[b]	108	105	99.9	2	8.41	1.15	14.6	11.2
12.11.04/ 4.[b]	110	109	98.6	2	-	-	13.1	10.7
01.12.04/ 5.	108	105	99.6	7	7.98	1.26	14.3	11.8

[a] Ozone samples used as reference material for the spectroscopic measurements.
[b] Ozone samples investigated by TDLAS technique

5. Spectroscopic Data Analysis

In this chapter, the investigation of high-resolution absorption spectra of ozone samples in selected spectral regions will be systematically presented. After some general remarks examples of micro-windows containing suitable absorption lines for isotope ratio measurements will be shown for each individual spectral range. The analysis procedure employed for accurate determination of the optical densities and isotope abundance ratios is discussed in detail.

5.1. General Remarks

Accurate isotope ratio measurements require the simultaneous determination of the isotopic abundance in a sample and standard material, respectively. With this respect the reactivity of the ozone molecule does need special attention. The first important constraint is that a stable ozone standard is not available. Secondly, the time evolution of the ozone sample concentration in the multipass cell leads to an additional complication, which needs to be accounted for.

In order to circumvent the first problem, a unique ozone preparation method has been employed, namely ozone generation in a low pressure electric discharge (see page 49). The isomeric distribution of ozone isotopologues in such samples appears to be well characterized. It can therefore be used as standard material (SM) for the laser spectroscopic measurements. In Figure 5.1 and 5.2 a comparison of a standard with a sample spectrum is shown. It can easily be observed that while the symmetric ozone species have the same optical densities in both the standard and the sample, respectively, the asymmetric species are more abundant in the sample than in the standard. This demonstrates the distinct isotopic characteristics of the two O_3 samples obtained under different ozone formation conditions.

The second restriction has been diminished by a proper treatment of the multipass cell interior metal surfaces (see Chapter 3, page 32). Blank experiments demonstrated that within about two hours of scanning, the ozone sample concentration may decrease by approximatively 4 - 6 %. The scatter of the ozone lifetime in the multipass cell is most likely due to non-identical surface conditions.[1] Averaging optical densities of the sample ozone over all the different spectral windows, and then taking the ratio with the similarly averaged optical densities of the reference ozone, whose concentration might have a different time evolution, thus is a potential source of error for the measured ratios of more than 5 ‰. Therefore, this time dependency factor must be considered in the data evaluation analysis.

[1] The ozone decomposition is very sensitive to catalysis by impurities and by surfaces

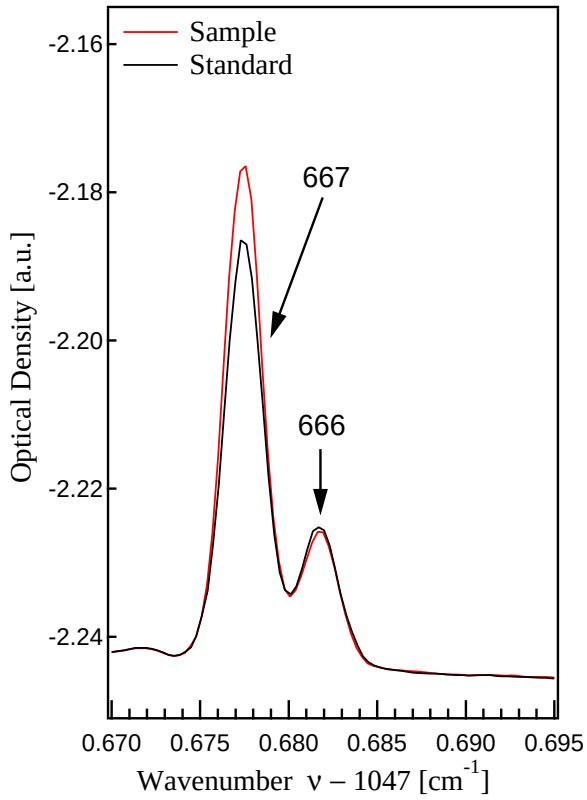

Figure 5.1.: Comparison of the absorption features of sample and standard ozone. Due to a fortunate coincidence, the amount of sample ozone produced in photolytic recycling experiment was exactly the same as the "standard" ozone generated in low-pressure electric discharge. This makes a direct and illustrative comparison of the two possible. The similarity of the absorption features of $^{16}O^{16}O^{16}O$ species provides a simple measure how good the ozone amounts match in the two gas samples. Note that, although, there is a perfect match, the asymmetric $^{49}O_3$ isotopomer in the sample ozone is more abundant than in the standard.

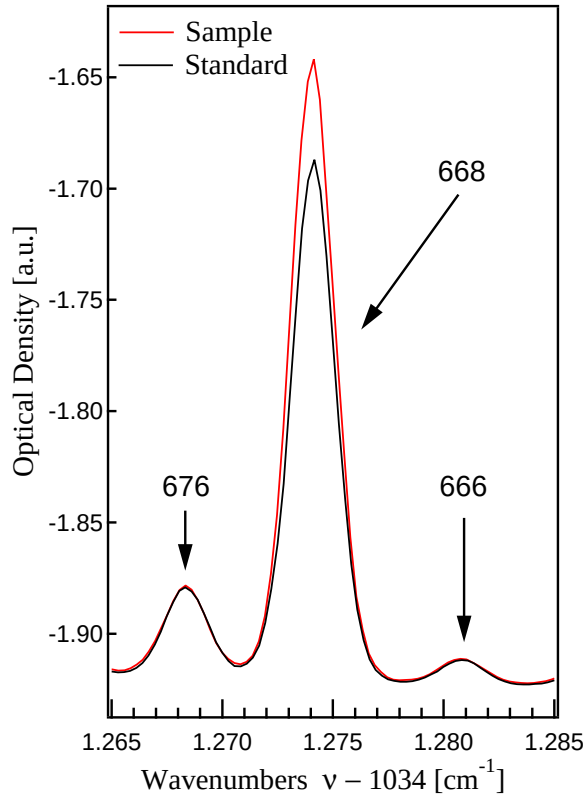

Figure 5.2.: The same as the top figure, but in a different spectral region. It clearly demonstrates that spectral features of symmetric ozone isotopomers ($^{16}O^{16}O^{16}O$ and $^{16}O^{17}O^{16}O$) perfectly overlap each other, while the asymmetric $^{50}O_3$ isotopomer in the sample ozone is again more abundant relative to the standard.

The method employed to minimize this ozone degradation effect on the measured abundance ratios is relatively simple. It relies on two factors: on the fast scanning speed (48 s/spectrum) of the laser diode and secondly, on the separate evaluation of individual spectral regions.

The first factor assures that the time, which is needed to acquire 20 spectra of a given frequency range is short enough ($\simeq$ 16 minutes) to avoid significant ozone degradation. The optical densities of individual ozone isotopomer absorption lines are then averaged over all the 20 scans. An eventual degradation effect is eliminated by dividing individual averaged absorption signals from sample and reference. It should be noted that this is valid only when absorption lines recorded within the same spectral window are used. Otherwise, apart from variations in ozone decomposition, time shifts of about ten minutes (times[1] required for temperature adjustment of the laser diode) between the two recording sequences of sample and reference ozone alone lead to artificial fractionation effects. As a consequence, the data evaluation procedure was thus to first calculate optical density ratios $(\tau_x)_S/(\tau_x)_R$ for each line within a selected window and then average over all ratios available, separately. From these average values the ratio of optical densities is obtained (see Eq. 2.23). Because the fractionation effects due to heterogeneous ozone decomposition in the cell are negligible ($<$ 1‰), considering the observed ozone decomposition times of about 33 h, averaging of individual ratios over all the available windows is possible.

In the next Chapter, the implementation of this approach will be considered and its validity is checked by a repeat measurement of the first window after a complete cycle (further details on page 78).

5.2. The Selected Spectral Regions

In the next pages, the direct absorption spectra of O_3 recorded in the four selected (see Figure 2.2 on page 23) spectral regions are shown.

As Figures 5.3 - 5.6 demonstrate, the IR spectrum around 1040 cm^{-1} of O_3 is very crowded and contains many overlapping transitions. The multitude of lines in the 10 μm spectral region is a result of several hot bands, including the $\nu_1 + \nu_2 - \nu_2$, $\nu_2 + \nu_3 - \nu_2$, $2\nu_3 - \nu_3$, $\nu_1 + \nu_3 - \nu_1$, and $2\nu_2 + \nu_3 - 2\nu_2$ bands. Despite these bands being very weak compared to the fundamental bands, the huge difference in the abundance between the main ozone isotopologue and its isotopic variants causes the absorption lines of $^{48}O_3$ that belong to the hot bands have similar intensities than the fundamental bands of $^{49}O_3$ and $^{50}O_3$. This is actually useful for finding regions that satisfy the selection criteria discussed in Chapter 2.

[1] The time required for the acquisition of 20 spectra was the same in every spectral range. This was obtained by taking the same scanning parameters for each spectral window: 24 mA tuning current divided in 3000 steps and 80 channels/s scanning speed. The jump to a selected frequency range of the TDL was manually achieved by changing the laser diode's heat sink temperature and adjusting the base current. The procedure practically took the same amount of time, typically 10 minutes until a stable operation of the TDL has been reached.

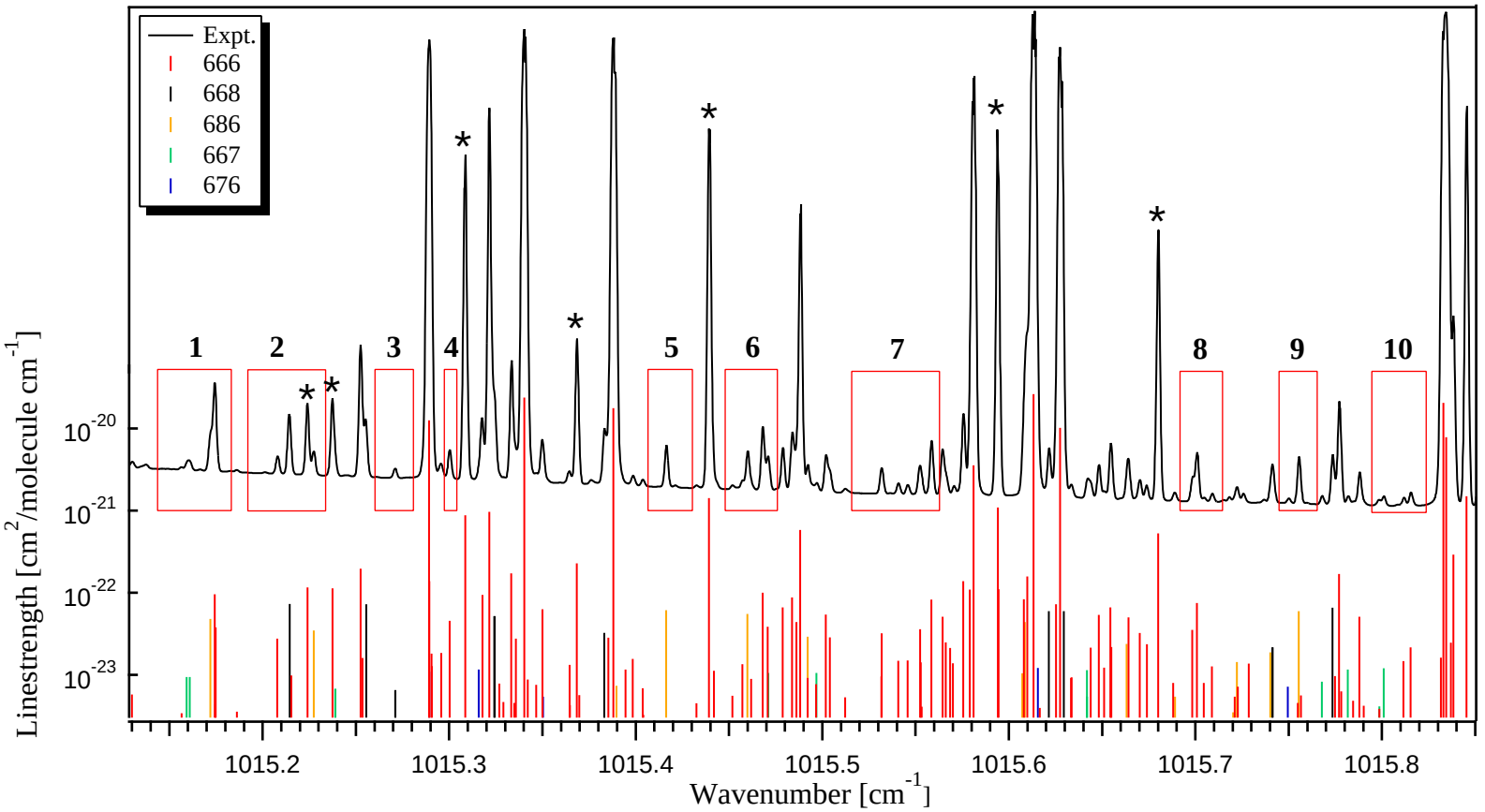

Figure 5.3.: Ozone absorption spectrum in spectral window I (in arbitrary units). Diode laser settings: T = 86 K, I = 225 mA. Micro-windows with suitable absorption lines for isotope ratio measurements are indicated by rectangles. For identification purposes, the HITRAN database values are displayed in a stick plot at the bottom. The experimental spectrum is frequency calibrated. The position of the ozone lines marked by stars served as frequency standards for the calibration. These lines are listed in the Appendix (Table C.1). For specifying the different isotopomeric species the AFGL shorthand notation is used.

In general, the published data of the fundamental bands agree well in position and intensity with the measured absorption features, but differences regarding the line positions – and probably the linestrengths – of individual lines in the hot bands and for the isotopic species may occur. A complete list of absorption lines of different ozone isotopologues, which have been used for isotopic ratio measurements, is given in the Appendix.

It should be noted that the ro-vibrational line intensities for the $^{16}O^{18}O^{16}O$ and $^{16}O^{17}O^{16}O$ isotopic species have been derived only through theoretical predictions. The dipole moment of the symmetrical species is derived from the $^{16}O^{16}O^{16}O$ dipole moment, and then used to calculate the line intensities for the fundamental bands. Finally, assuming a factor of 2 between the abundances[1] of $^{16}O^{16}O^{18}O$ and $^{16}O^{18}O^{16}O$ the line intensities of the asymmetric species are obtained [*Flaud and Bacis*, 1998]. It is obvious that there are several uncertainties regarding this method, and therefore, an ozone gas calibration standard is an absolute need to obtain the necessary accurate linestrength information.

The spectral window I (hereafter referred to as **SW-I**) has mainly been considered because of the symmetric $^{16}O^{18}O^{16}O$ species. In the present investigation, it is the only spectral region[2] that contains suitable absorption lines of this ozone isotopomer. Each of the five lines associated to $^{16}O^{18}O^{16}O$ has sufficiently strong intensity for an accurate determination of optical densities. In this frequency range, the main ozone isotopologue, $^{48}O_3$, has only very few strong absorption features and they are well separated from the $^{16}O^{18}O^{16}O$ isotopomer lines, *i.e.*, no overlap or interference occurs. Nevertheless, there are many individual weak absorption features of $^{48}O_3$, which allow to accurately determine the abundance of this species.

Even though there are only a few micro-windows, the spectral window II (**SW-II**) has a number of well separated non-overlapping $^{16}O^{17}O^{16}O$ lines. Such absorption features are rare and, therefore, this frequency range is important for the linestrength measurement of the symmetric ^{17}O containing ozone isotopomer.

Spectral window III (**SW-III**) provides most information about the different ozone isotopologues. In this frequency range all the naturally occurring isotopic species, except for the symmetric $^{50}O_3$, can be found. The asymmetric $^{50}O_3$ and $^{49}O_3$ species have a number of well separated absorption features, and even the symmetric $^{49}O_3$ isotopomer has three exceptionally suitable lines. The analysis is further facilitated due to the fact that in this frequency domain the main ozone isotopologue has weak and only few absorption lines.

For the spectral window IV (**SW-IV**) the situation is similar to that of **SW-III**. The identification of suitable lines of symmetric $^{49}O_3$, however, was hampered by the fact that reported line positions in the HITRAN'04 database suffered from a substantial shift in the frequency.

[1] It assumes that during the production of O_3, no isotopic enrichment occurs

[2] Obviously, at lower wavenumbers ($\nu < 1000\,cm^{-1}$) where the $^{16}O^{18}O^{16}O$ isotopomer reaches maximum intensity in its P-branch practically without overlapping with other species (the main ozone isotopologue has only very weak absorption features), is another spectral region with potentially suitable absorption lines. However, the frequency range of the selected laser diode was about 1010 - 1070 cm^{-1}.

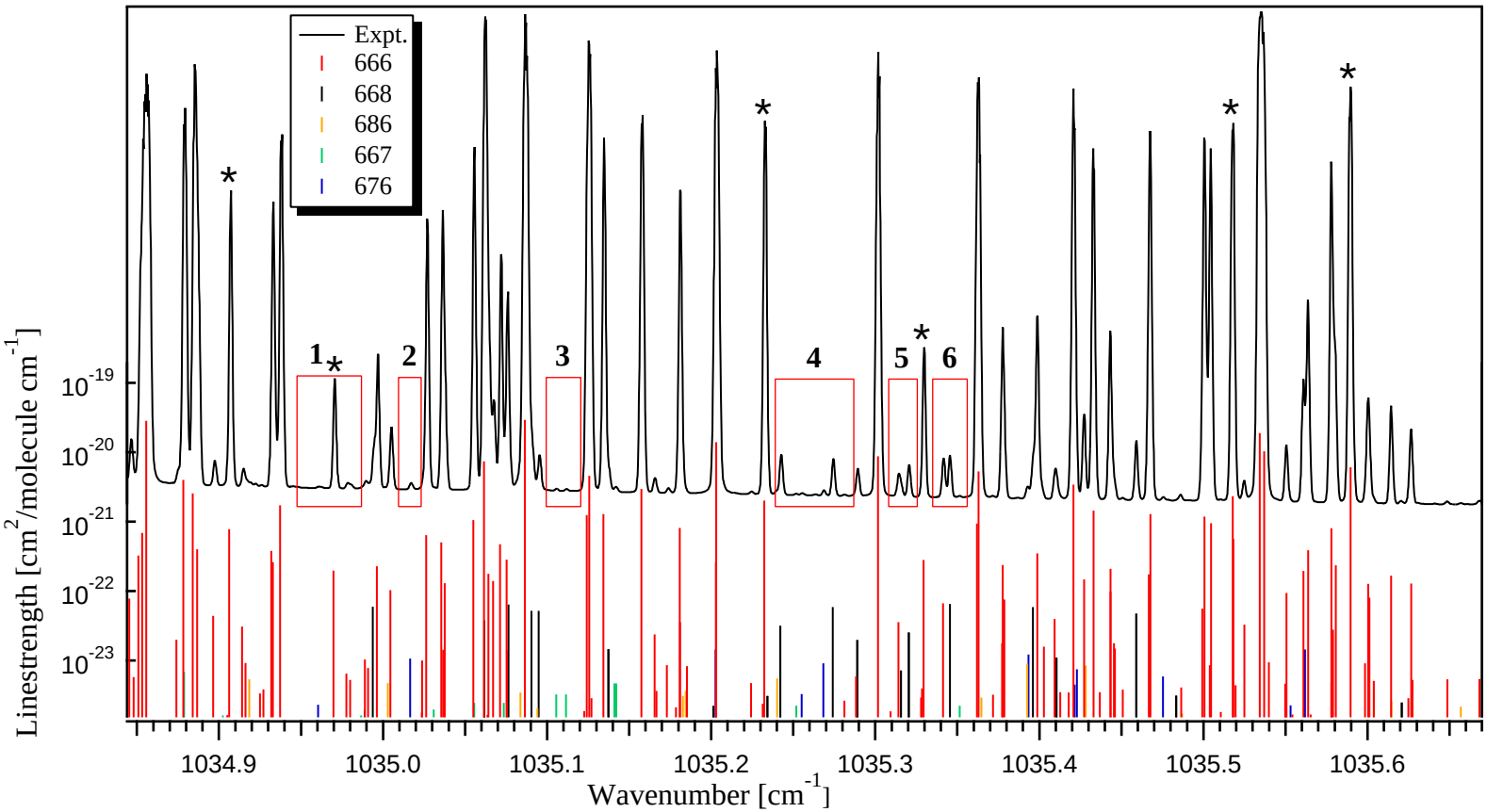

Figure 5.4.: Ozone absorption spectrum in spectral window II (in arbitrary units). Diode laser settings: T = 89 K, I = 290 mA. Micro-windows with suitable absorption lines for isotope ratio measurements are indicated by rectangles. For identification purposes, the HITRAN database values are displayed in a stick plot at the bottom. The experimental spectrum is frequency calibrated. The position of the ozone lines marked by stars served as frequency standards for the calibration. These lines are listed in the Appendix (Table C.1).

An offset of about $2.3 \times 10^{-3}\,\mathrm{cm}^{-1}$ has been determined (see Table E.1), and it was possible to find three well isolated absorption lines associated to $^{16}O^{17}O^{16}O$, which according to the database should actually interfere with other absorption features. Besides these lines, well separated and strong absorption features of asymmetric $^{50}O_3$ isotopomer can be found.

In order to unambiguously ascertain the identity of the absorption features, two different ozone samples have been prepared. The first sample was produced from pure, natural O_2, while the second from ^{17}O-doped molecular oxygen. By comparing the two ozone absorption spectra, it was easy to identify the $^{49}O_3$ isotopomers, because of their increased absorption signals. Examples of this comparison is given in the Appendix. Moreover, the frequency shift of $^{16}O^{17}O^{16}O$ line positions has been investigated and accurately measured by calibrating the frequency scale with CO_2 laser II band transitions. In Table E.1 the list of the studied absorption lines are given. From the measurements it is clear that the revealed frequency offset of the symmetric $^{49}O_3$ isotopomer is not a constant value overall in the database. For example, the offset is almost negligible in the frequency range of 1015 - 1038 cm^{-1} ($\leq 1 \times 10^{-4}\,\mathrm{cm}^{-1}$), but is very pronounced in the range of 1042-1044 cm^{-1}, where deviations of more than $3 \times 10^{-3}\,\mathrm{cm}^{-1}$ have been determined.

Altogether about 80 absorption lines of different ozone isotopologues have been used for isotopic ratio analysis. For the major experiment (photolytic recycling) the maximal number of lines was used, while in the case of the control experiments (the high pressure electric discharge and ozone photolytic dissociation) fewer lines have been utilized. An exact account of the number of lines analyzed in the various experiments is given in Table 5.1.

Table 5.1.: The number of absorption lines analyzed in different experiments.

Isotopic Species	Number of Lines		
	A	**B**	**C**
$^{16}O^{16}O^{16}O$	30	22	18
$^{16}O^{16}O^{18}O$	19	17	6
$^{16}O^{18}O^{16}O$	5	5	5
$^{16}O^{16}O^{17}O$	13	10	6
$^{16}O^{17}O^{16}O$	11	8	5

Here **A** stands for photolytic recycling, **B** for high pressure electric discharge and **C** for ozone photolytic dissociation experiments, respectively.

Each of the spectra was recorded at room temperature. The laboratory room was air conditioned, and kept at $21 \pm 1\,^{\circ}\mathrm{C}$. The cell temperature was monitored with two Pt-thermocouples (to within $0.1\,^{\circ}\mathrm{C}$ accuracy) mounted at the glass tube of the multipass cell. In order to minimize random air-fluctuations, the cell was covered with photographic black paper, which, beside thermal isolation, also prevents unwanted illumination of the ozone sample inside the cell.

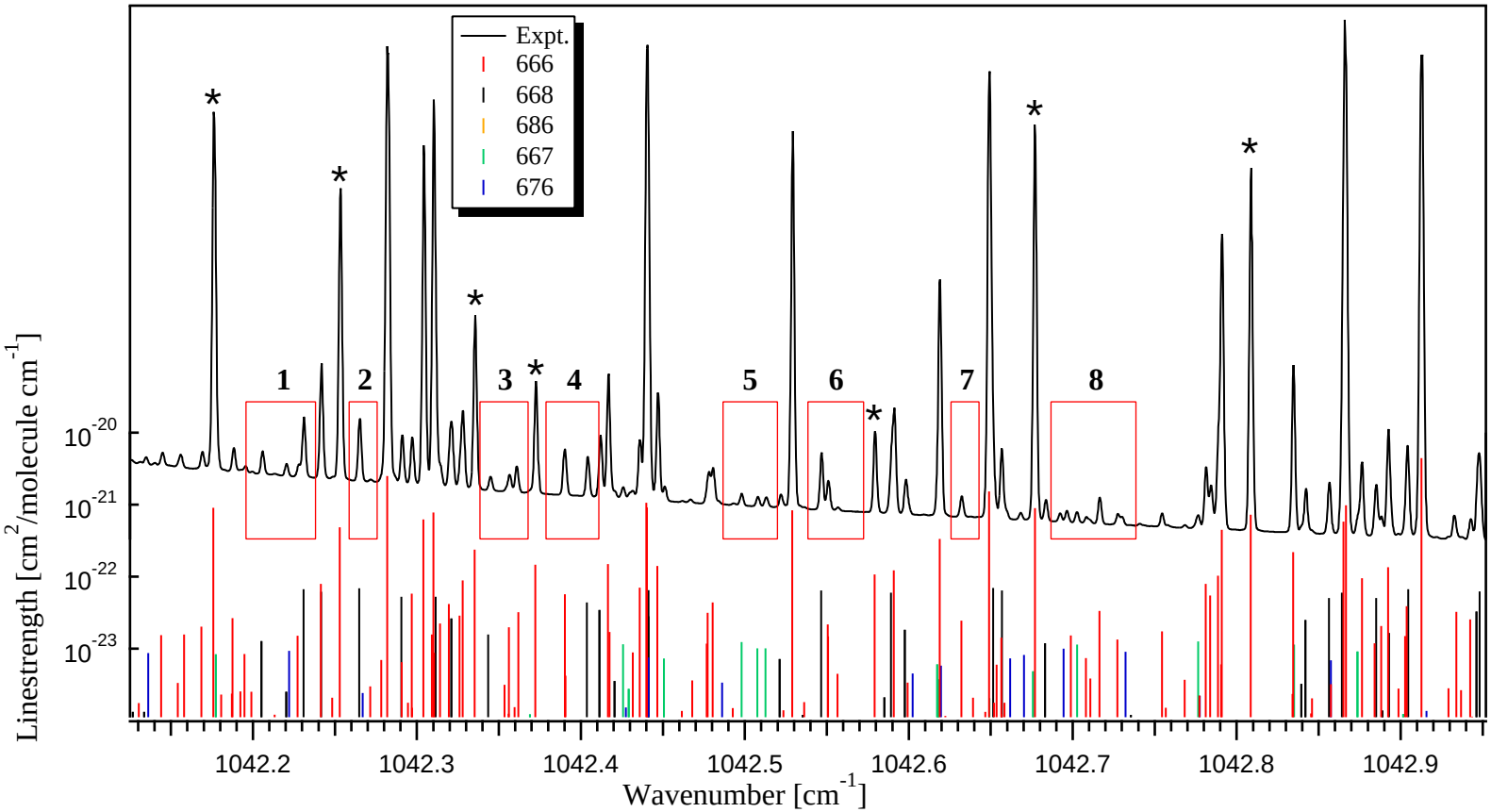

Figure 5.5.: Ozone absorption spectrum in spectral window III (in arbitrary units). Diode laser settings: T = 91 K, I = 273 mA. Micro-windows with suitable absorption lines for isotope ratio measurements are indicated by rectangles. For identification purposes, the HITRAN database values are displayed in a stick plot at the bottom. The experimental spectrum is frequency calibrated. The position of the ozone lines marked by stars served as frequency standards for the calibration. These lines are listed in the Appendix (Table C.1).

Due to the different lower state energies of individual ro-vibrational transitions the line-strength ratios are temperature dependent.[1] In Chapter 2, the temperature dependence of the absorption linestrength was given by Eq. 2.16 (see page 19). The expression contains three temperature dependent terms, apart from the absorption linestrength at the reference temperature. The term, which accounts for the stimulated emission can be set equal to one (at $\Delta T = 1\,K$, the absolute change of this term is about 0.1 ‰) in the 10 μm spectral region and at room temperature. To estimate the importance of the second term, the temperature dependence of the total internal partition functions needs to be known. Accurate calculations of the total internal partition sums for the ozone isotopomers can be performed in a rapid and convenient way using a third-order polynomial expression in temperature [*Gamache et al.*, 2000]:

$$Q(T) = a + bT + cT^2 + dT^3. \tag{5.1}$$

This expression reproduces the partition sum better than 1 %. The polynomial coefficients are listed in *Gamache et al.* [2000]. Based on this approach, it was found that 1 K temperature variation introduces about 5.8 ‰ change in the total internal partition function, which, however, is independent from the ozone isotopomer considered. Therefore, its temperature dependence cancels in the isotope ratio measurements.

The most pronounced temperature dependency is actually in the third term that accounts for the ratio of Boltzmann populations. A relative temperature variation of $\Delta T/T$ leads to a relative change of the absorption signal

$$\frac{\Delta S}{S} = \frac{E_i}{kT}\frac{\Delta T}{T}, \tag{5.2}$$

with E_i being the lower state energy. Taking 50 and 2000 cm^{-1} as the lower and upper limits for E_i that appear in this work, the corresponding relative change in the Boltzmann-term will be between 0.08 % and 3.22 %. Since absorption lines of the $^{48}O_3$ species were chosen to have low intensities, comparable to that of the minor isotopic species, they have much higher ground state energies than the other molecules. In the present case, the $^{48}O_3$ isotopologue has lower-state energies around 1650 cm^{-1}, $^{16}O^{16}O^{18}O$ and $^{16}O^{17}O^{16}O$ about 340 cm^{-1}, $^{16}O^{16}O^{17}O$ around 110 cm^{-1} and $^{16}O^{18}O^{16}O$ just 50 cm^{-1}. Hence, the $^{48}O_3$ absorption lines are most strongly affected by temperature variations.

It is therefore evident that a small thermal drift in the ozone sample temperature translates into a drift in the measured isotopic ratio and, finally in the δ-value. The selection of comparable absorption depths, therefore, introduces a significant temperature sensitivity. If we control the temperature to within 0.1 K between the sample and reference measurements, the lower state energy levels separated by $\geq 1000\,\mathrm{cm}^{-1}$ limit the achievable precision to approximatively 2 or 3 ‰. This level of precision is comparable with the precision of the mass spectrometer employed for the isotopic fractionation measurements.

[1] The Doppler width of an absorption line is also temperature dependent, but its contribution is < 1 ‰ and can be neglected.

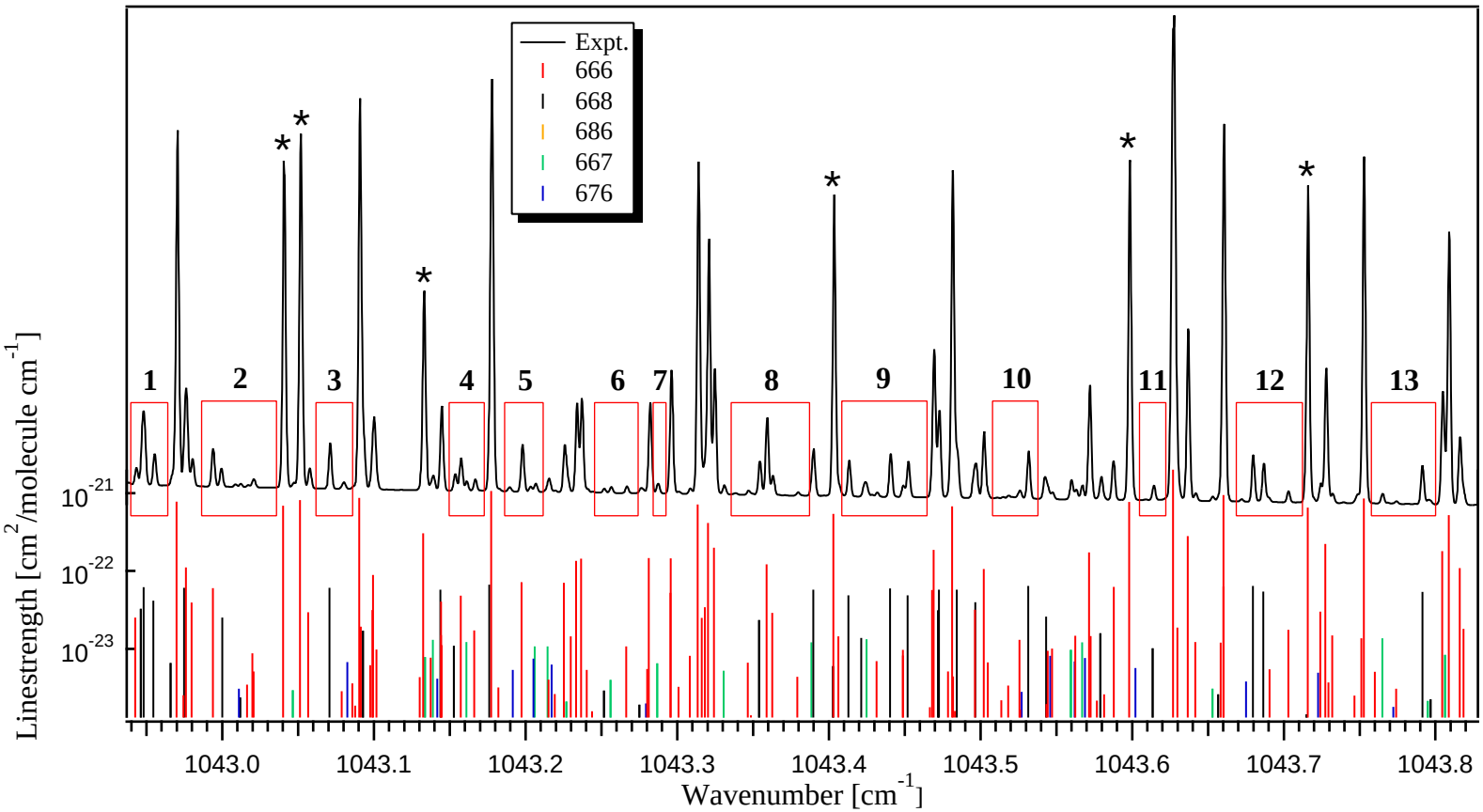

Figure 5.6.: Ozone absorption spectrum in spectral window IV (in arbitrary units). Diode laser settings: T = 90 K, I = 325 mA. Micro-windows with suitable absorption lines for isotope ratio measurements are indicated by rectangles. For identification purposes, the HITRAN database values are displayed in a stick plot at the bottom. The experimental spectrum is frequency calibrated. The position of the ozone lines marked by stars served as frequency standards for the calibration. These lines are listed in the Appendix (Table C.1).

5.3. Analysis of High Resolution Absorption Spectra

The analysis of an absorption spectrum is concerned with obtaining accurate parameters to represent the absorption features (peaks). Three such parameters that define a peak are its position, amplitude, and width (FWHM). The absorption lines in spectroscopic data generally appear on a background. In order to accurately determine peak parameters, the background must be subtracted correctly. Improper correction for the background of a spectrum can skew peak positions and alter their FWHM. More importantly, the area of a peak is determined by subtracting an appropriate background and integrating under the resultant curve. Moreover, the frequency scale is required to be linear. Otherwise distortions of absorption line-shapes may occur.

For the analysis of the spectroscopic data a commercially available software package has been used, namely Igor Pro (v. 5.03, Wavemetrics Inc.). Its built-in peak analysis feature permits fitting[1] of multiple and even overlapping peaks. It can remove backgrounds from the spectroscopic data by including a baseline function when fitting a sum of functions to the data.

Raw spectra of the TDLAS are recorded *vs.* the diode current (given in channel numbers), which is not directly related to the actual frequency. Likewise, the ordinate scale is an arbitrary voltage, representing the output of the signal demodulators. For quantitative analysis it is necessary to convert the abscissa to units of frequency. Using a two-channel configuration ozone absorption spectra and FPE transmission signals can be simultaneously recorded. A calibration procedure, then, automatically converts the abscissa into a linearized, relative frequency scale using the etalon fringes. Based on well known ozone absorption line positions that were selected as frequency standards, the procedure performs an absolute frequency calibration. This procedure is performed for each spectrum individually (for more detail consult Appendix A).

Weak absorption features require to average the determined optical density over a set of spectra. This improves the signal-to-noise ratio by increasing the effective signal integration time and also gives an assessment of statistical errors due to the experimental dispersion of the measurements. Typically, 20 individual spectra have successively been recorded in each spectral range.

To calculate the optical density, the incident light intensity, I_0, must be known accurately. The frequency scan is wide enough (about $1\,\mathrm{cm}^{-1}$) to assure that I_0 can be inferred from portions of the scan, which are free of any absorption features. Thus, the systematic error introduced by uncertainties in the determination of the polynomial baseline is small. An effective fitting procedure has been implemented, which uses a quadratic polynomial[2] to fit regions of the baseline that surround the spectral features of interest. This baseline represents I_0 for each spectral micro window. The residual

[1] The fitting procedure uses the Levenberg-Marquardt algorithm to search for the coefficient values that minimize chi-square.

[2] To use higher degree polynomial for the baseline determination can produce unwanted oscillations in the spectrum similar to optical fringing. A 2^{nd} order polynomial function defines the unattenuated diode-laser power accurately without suffering from the laser power fluctuations.

plot is used to decide whether the fit is good or whether there may be additional peaks lurking in the data or whether the baseline is not correctly defined. After a good fit, the residuals should be just noise.

The peak positions, amplitude, FWHM and area obtained from the fit are separately stored for each spectrum. In this "spectrum-by-spectrum" least-squares fitting method, no correlation is introduced between the spectra. The data processing procedures outlined above were exclusively carried out using a combination of interactive graphics routines and automated spectrum manipulation routines written in IGOR.

On the next pages two examples of micro-windows for three selected spectral regions are given. In addition to the recorded high-resolution absorption spectrum, the multi-peak least-squares fit used to model[1] the experimental data is plotted. Together with the measured spectra, the calculated spectra based on linestrengths and positions from HITRAN'04 are depicted as stick plots. This way, the identification of absorption lines belonging to different ozone isotopologues is straightforward. However, sometimes we have to deal with serious frequency shifts in the line position, which reflects the uncertainties in the calculations employed for generating the spectroscopic database.

The upper plots show the residuals of the least-squares fit, which give a good account of the validity of the fit-model performed. Practically, it is the only way to decide whether a fit in combination with the modelled baseline is correct or needs adjustments. The spectral features of interest in the selected part of the spectrum are accentuated by darker color. This also indicates which parts were considered in the fit. Note that the base-line sections are as large as possible (up to $0.4\,\mathrm{cm}^{-1}$) to better define I_0. By fitting a quadratic polynomial to the base-line, the background intensity variation of the diode laser output is removed.

[1] Due to the low O_3 pressures (ranging from 80 to 130 mTorr), the molecular collisions are less frequent, and leave thermal motion to be the dominant broadening mechanism. The corresponding line shape is Gaussian. Furthermore, it was experimentally found that the laser line shape can be well approximated by a Gaussian. This Gaussian is then convoluted to the Doppler line-shape function to produce a combined low-pressure line-shape function.

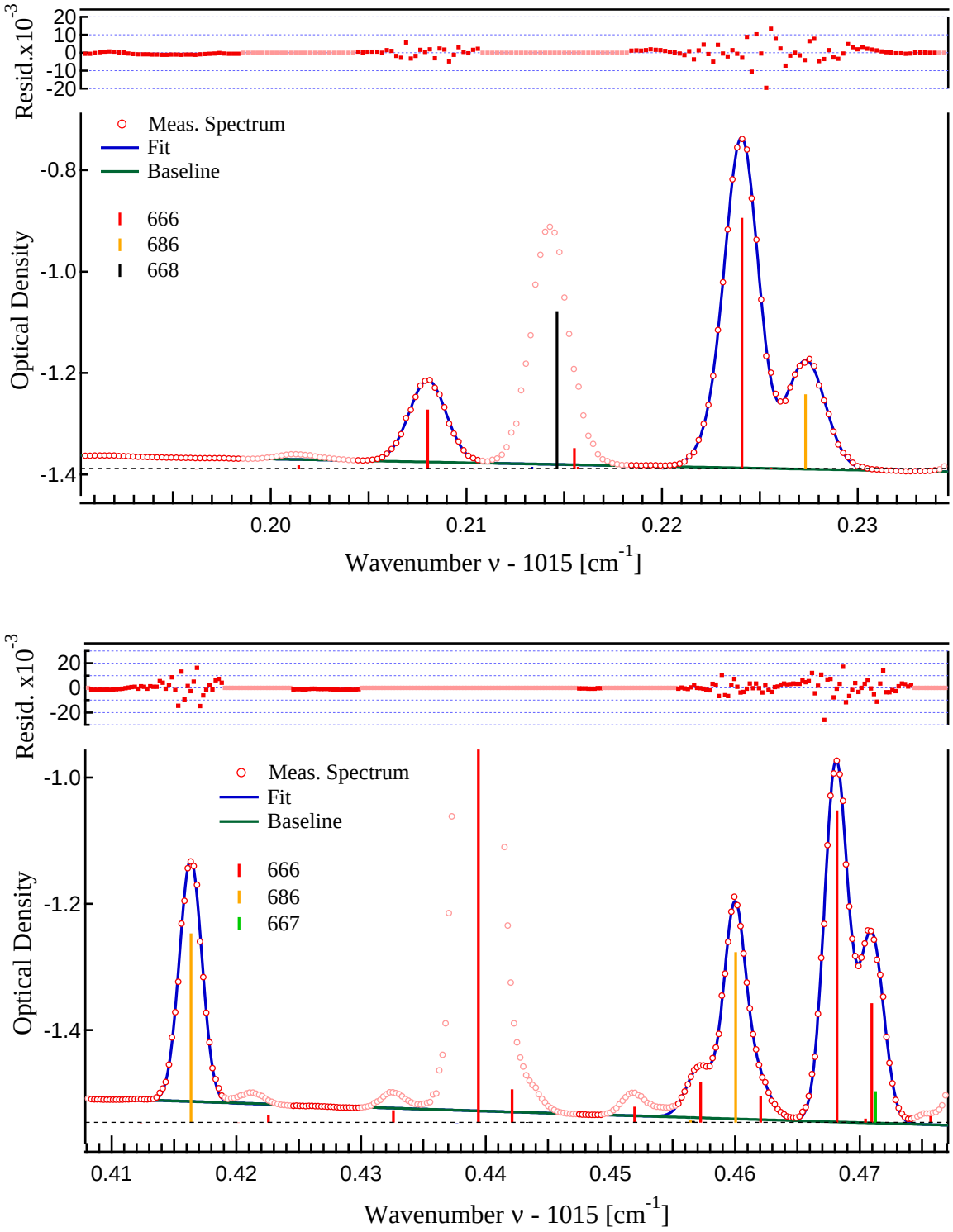

Figure 5.7.: Two micro-windows from **SW I**. Top panel: Micro-window 2. Bottom panel: Micro-windows 5 and 6. (see Figure 5.3). The spectral features of interest in the selected part of the spectrum are accentuated by darker color. This also indicates which parts were considered in the fit. The calculated spectra based on linestrengths and positions from HITRAN'04 are depicted as stick plots.

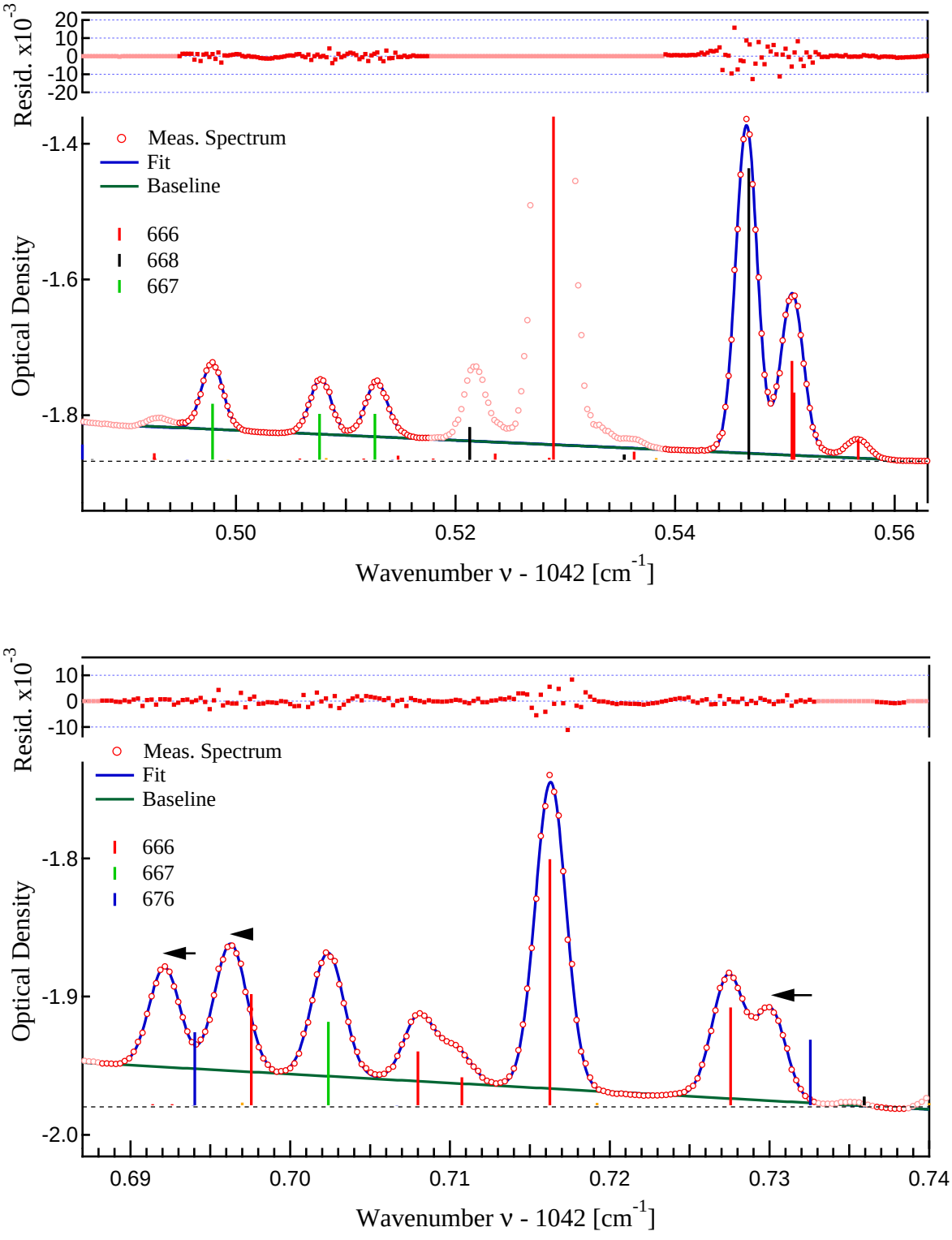

Figure 5.8.: Two micro-windows from **SW III**. Top panel: Micro-window 5 and 6. Bottom panel: Micro-windows 8 (see Figure 5.5). The spectral features of interest in the selected part of the spectrum are accentuated by darker color. The frequency shifts in the line position listed in the spectroscopic database are indicated by arrows.

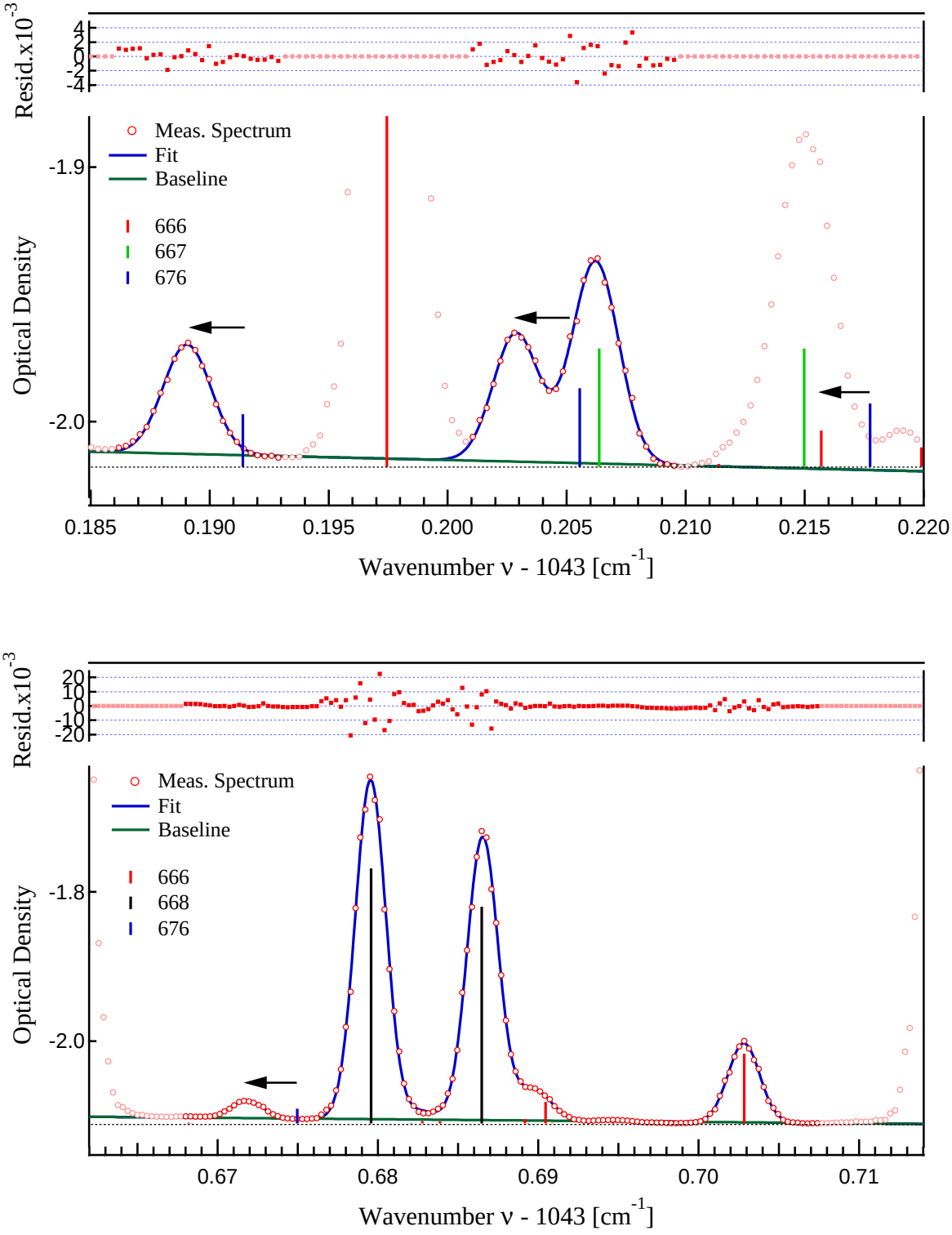

Figure 5.9.: Two micro-windows from **SW IV**. Top panel: Micro-window 5. Bottom panel: Micro-windows 12 (see Figure 5.6). The spectral features of interest in the selected part of the spectrum are accentuated by darker color. The frequency shifts in the line position listed in the spectroscopic database are indicated by arrows.

6. Results and Discussion

This chapter summarizes the results of the laser spectroscopic measurements. Due to the large number of recorded IR spectra (> 700) and due to the amount of investigated absorption lines (up to 79 lines), a detailed presentation of the raw data from the spectral analysis is omitted here (for completeness they are given in the Appendix). Instead, average values typically over 20 spectra of the evaluated optical density ratios between sample and reference will be discussed. Total enrichments E_{49} and E_{50}, respectively, derived from the spectroscopic data are compared with the mass spectrometric measurements in order to assess the accuracy of the TDLAS technique. Branching ratios of individual ozone formation reactions as well as the relative abundance of asymmetric *vs.* symmetric species of the $^{49}O_3$ and $^{50}O_3$ isotopologues from scrambled oxygen are determined. Finally, the transfer of isotope anomaly from ozone into carbon dioxide is investigated.

6.1. Enrichments and Rate Coefficients

Before presenting the results of the TDLAS measurements, an overview of the isotopomer specific kinetics of ozone formation in scrambled mixtures of ^{16}O, ^{17}O and ^{18}O containing oxygen is appropriate. In order to interpret the measurement data, the ratios of isotopomer and isotopologue abundances need to be related to the kinetic quantities. Potential fractionation effects due to side reactions that may influence the final results also need to be accounted for.

As pointed out in the introductory part of this work, the anomalous isotope effect has to be attributed to the elementary kinetic process of the gas phase recombination reaction [*Morton et al.*, 1990]:

$$O(^3P) + O_2(^3\Sigma_g) + M \rightarrow O_3 + M. \tag{6.1}$$

Considering the naturally occurring oxygen isotopes, ozone formation takes place via four possible reaction channels:

$$^xO + {}^{16}O{}^{16}O + M \xrightarrow{(1-\gamma)k_{x+66}} {}^xO{}^{16}O{}^{16}O + M \tag{6.2a}$$

$$\xrightarrow{\gamma k_{x+66}} {}^{16}O{}^xO{}^{16}O + M \tag{6.2b}$$

$$^{16}O + {}^{16}O{}^xO + M \xrightarrow{\frac{1}{2}k^a_{6+6x}} {}^{16}O{}^{16}O{}^xO + M \tag{6.2c}$$

$$\xrightarrow{\frac{1}{2}k^s_{6+6x}} {}^{16}O{}^xO{}^{16}O + M \tag{6.2d}$$

where ^xO stands for the ^{17}O or ^{18}O isotope. The k are the rate coefficients of the individual reaction channels (here x in the index of the rate coefficients is the AFGL

shorthand notation for various oxygen atoms and diatoms) and the parameter γ gives the branching ratios between the reaction channels in which an O atom reacts with a homonuclear oxygen molecule. Obviously, when the reaction of an O atom with a homonuclear O_2 proceeds in an end-on fashion, $\gamma = 0$. It should be noted that an additional normalization factor of 2 is introduced in the rate coefficients k^a_{6+6x} and k^s_{6+6x}. This serves to give reaction probabilities when compared to k_{6+66} and therefore is a measure of the isotopic effect in these reactions [*Janssen et al.*, 2001].

In the photolytic recycling experiment, which is the preferred means to study the isotopic effects in ozone formation (see Chapter 4), the isotopic composition of ozone is due to formation and decomposition reactions, respectively. Furthermore, the isotopic fractionation in the formation is not solely due to the different reaction rate coefficients, but also due to the exchange reactions, such as

$$^{x}\mathrm{O} + {}^{16}\mathrm{O}{}^{16}\mathrm{O} \xrightarrow{k_x} {}^{16}\mathrm{O} + {}^{16}\mathrm{O}{}^{x}\mathrm{O} \tag{6.3a}$$

$$^{16}\mathrm{O} + {}^{16}\mathrm{O}{}^{x}\mathrm{O} \xrightarrow{k_{-x}} {}^{x}\mathrm{O} + {}^{16}\mathrm{O}{}^{16}\mathrm{O}. \tag{6.3b}$$

In the low-pressure limit these reactions are 3 to 4 order of magnitude faster than ozone formation. The exchange reactions therefore establish a dynamic equilibrium between the molecular oxygen composition and the atoms. By use of the equilibrium constant $K_x = k_x/k_{-x}$ for the forward and reverse reaction the relationship of the atomic ratio to molecular oxygen may be expressed as:

$$\frac{[^{x}\mathrm{O}]}{[^{16}\mathrm{O}]} = \frac{1}{K_x}\frac{[^{x}\mathrm{O}^{16}\mathrm{O}]}{^{16}\mathrm{O}_2}, \tag{6.4}$$

which implies a depletion of the heavy oxygen atoms. Because ozone fractionation values are defined with respect to the molecular oxygen bath, a deviation of $[^{x}\mathrm{O}]\,/\,[^{16}\mathrm{O}]$ from the $^{x}\mathrm{O}/^{16}\mathrm{O}$-ratio in O_2 thus is an additional source of fractionation.

Ozone decomposition occurs via (see Chapter 4):

$$\mathrm{O}_3 + h\nu \rightarrow \mathrm{O}(^3P) + \mathrm{O}_2(^3\Sigma_g^-) \tag{6.5}$$

and may have an influence on the isotopic composition of ozone. At present, the isotopic effect in (6.5) is not well quantified. This is mostly due to the experimental difficulty in separating the photolysis step (6.5) from subsequent ozone destroying reactions of the photo-products, such as

$$\mathrm{O}_3 + \mathrm{O}(^3P) \rightarrow 2\mathrm{O}_2(^3\Sigma_g^-). \tag{6.6}$$

Though direct measurement of the fractionation factor of visible light photolysis (6.5) cannot be performed, repeated test experiments, in which pure ozone was photolyzed, revealed that the combined effect of ozone photolysis may contribute to the observed isotope fractionations by about 1 %.

When the consumption of molecular oxygen is neglected for the moment and when ozone destruction is insignificant, the isotopologue enrichment E_u is directly linked to the rates of ozone formation (6.2a - 6.2d) and to the equilibrium constant K_x of the exchange reactions (6.3a, 6.3b) [*Anderson et al.*, 1997]:

$$1 + E_u = \frac{2}{3}\left[\frac{1}{K_x}\frac{k_{x+66}}{k_{6+66}} + \frac{k_{6+6x}}{k_{6+66}}\right], \tag{6.7}$$

where u represents the ozone isotopologues of mass 49 (for $x = 7$) and 50 (for $x = 8$), respectively. Similar relations hold for the isotopomer specific enrichments E_u^a and E_u^s, too.

$$1 + E_u^a = \frac{1}{2}\left[(1-\gamma)\frac{2}{K_x}\frac{k_{x+66}}{k_{6+66}} + \frac{k^a_{6+6x}}{k_{6+66}}\right], \tag{6.8a}$$

$$1 + E_u^s = \gamma\frac{2}{K_x}\frac{k_{x+66}}{k_{6+66}} + \frac{k^s_{6+6x}}{k_{6+66}}. \tag{6.8b}$$

Eqs.(6.7) - (6.8b) implicitly fulfill the mass balance requirement:

$$3E_u = 2E_u^a + E_u^s. \tag{6.9}$$

When ozone photolysis has a significant effect on the observed ozone isotopic composition E_u, than the previously used enrichment values characterizing the formation effects $E_{u(formation)}$ can still be deduced, provided that the fractionation $E_{u(phot)}$ in the photolysis is known. From the steady state condition in the photolytic recycling experiment one obtains:

$$1 + E_{u(formation)} = \frac{1 + E_u}{1 + E_{u(phot)}}. \tag{6.10}$$

Based on these relationships the spectroscopic results can easily be interpreted. Four distinct ozone samples, generated at almost the same conditions in the photolytic recycling experiment, have been studied. Below, one example of the evaluation of such an ozone sample is given in detail (Table 6.1). The spectroscopic results of the other three samples are listed in the Appendix. Since the same oxygen gas was used to produce ozone for sample and reference measurements, symmetry-specific fractionations could be determined by direct comparison of sample and reference signals.

The results show that the enrichment not only predominantly, but also almost exclusively resides in the asymmetric isotopomers $^{16}O^{16}O^{17}O$ and $^{16}O^{16}O^{18}O$. Compared to the size of the fractionation effect ($\sim 20\,\%$) the difference between the two asymmetric species is only marginal. The agreement between the observed variation of the fractionation values derived from individual spectral windows and the uncertainties estimated from individual absorptions within a single spectral window demonstrates the data consistency. A similar degree of consistency is observed when all four different ozone samples are compared (Table 6.2).

Table 6.1.: Spectroscopic results of the photolytic recycling experiment from **28.10.04** (Sample #8. in Table 4.4). The mean values of the isotopic abundance ratios of sample (ozone produced by photolytic recycling) and reference material (ozone obtained from heterogeneous wall formation in low pressure electric discharge) are given ($\bar{R}_{g/w}$) together with their relative errors (e_r). Every data point is an average of several absorption lines whose optical densities are calculated from 20 consecutive, individual scans. When there are temperature differences between sample and reference, the linestrengths are properly corrected. Isotope fractionation values ($\bar{E}_u$) are the weighted means of individual E_u values determined separately for each spectral window (SW). Their estimated standard deviations are given in parentheses.

SW	**Ozone Isotopomers**[a]									
	666		668		686		667		676	
	$\bar{R}_{g/w}$	e_r (%)	$\bar{R}_{g/w}$	e_r (%)	$\bar{R}_{g/w}$	e_r (%)	$\bar{R}_{g/w}$	e_r (%)	$\bar{R}_{g/w}$	e_r (%)
I	1.0133	0.12	1.2362	0.59	1.0371	0.17	1.2011	0.56	1.0241	0.58
	1.0276	0.23	-	-	1.0497	0.34	-	-	-	-
II	1.0311	0.21	1.2515	0.18	-	-	1.2159	0.39	1.0376	0.28
III	1.0223	0.31	1.2422	0.21	-	-	1.2186	0.27	1.0338	0.33
IV	1.0285	0.22	1.2471	0.22	-	-	1.2210	0.35	1.0498	0.24
$\bar{E}_u$ **(%):**			**21.42**	(0.21)	**2.30**	(0.19)	**18.62**	(0.28)	**1.31**	(0.35)

[a] The AFGL shorthand notation is adopted to mark the different ozone isotopomers.

It must be stressed in this context that the good agreement of the TDLAS derived total enrichments with the completely independently measured mass spectrometric values is a firm demonstration of the precision obtained with the laser absorption spectrometer. This degree of agreement between MS and TDLAS is generally observed and is also proved in the measurements discussed later in this section.

In the measurements displayed in Tables 6.1 and F.6, the spectral window **SW I** was scanned twice. One scan was performed just at the beginning of the measurement when the ozone has been introduced into the multipass cell, and the other one after a one complete scanning cycle (including measurements in the spectral window **SW II**, **SW III** and **SW IV**). This allows to verify the validity of the implemented evaluation method, which attempts to minimize the effect of variable ozone concentrations on the measured isotope ratios. Although, the time interval between the two scans was about two hours, which is equivalent to a 4 to 6 % decrease in ozone concentration (not identical in the two samples), the fractionation values could be reproduced better than 0.2 % by taking the isotopic ratios for each scan separately. Thus, if the various spectral windows are separately evaluated the isotopic composition can reliably determined even though some ozone decomposition occurs during the measurement.

Table 6.2 summarizes the averaged values of isotopomer specific enrichments for all the four ozone samples. The total enrichments reported in Table 6.2 are related to the reference material, which is ozone formed heterogeneously in low-pressure electric discharge (see discussion in Chapter 4). However, they can be normalized to

the statistically expected ones simply by:

$$E^a_{u(g/s)} = E^a_{u(g/w)}(E^a_{u(w)} + 1) + E^a_{u(w)}\,, \tag{6.11a}$$

$$E^s_{u(g/s)} = E^s_{u(g/w)}\,, \tag{6.11b}$$

where $E^a_{u(w)}$ and $E^s_{u(w)}$ are given by Eqs. (4.9b) and (4.9c).

According to the discussion in Chapter 4, the good agreement between mass spectrometer and diode laser measurements further implies agreement with mass spectrometric photolysis recycling studies that were performed in the past [*Janssen et al.*, 2003; *Morton et al.*, 1990]. This provides additional support for the high degree of accuracy reached with the diode laser spectrometer, at least for the measurement of the total enrichments.

When isotopic effects due to the ozone destruction reactions like (6.5) or (6.6) can be neglected, the calculation of the relative rate coefficients is straightforward. Given the likely effect of photodissociation on the isotopic composition of ozone, the current status is not satisfactory, because a considerable uncertainty in the visible light experiments can be present. Therefore, repeated test experiments were performed to investigate whether the combined effect of ozone photolysis (6.5) and ozone destruction by atomic oxygen (6.6) would change the isotopic composition of ozone or not. In Table 6.3 the spectroscopic results of the leftover ozone from the VIS photolytic dissociation experiment is given. The values are normalized to the isotopic composition of the initial ozone. These results clearly show that, even though the isotopic effect due to the ozone dissociation reaction is small, its contribution cannot be neglected when the rate coefficients of ozone formation channels have to be calculated. The most affected will be the asymmetric $^{50}O_3$ isotopologue with a correction of almost 2 %. For all the other isotopomeric species the correction is less than 1 %.

Table 6.2.: Summary of isotopomer specific enrichments of ozone produced in photolytic recycling. Standard deviations of individual measurements are estimated from the scatter in the measured optical densities and given in parentheses. The average values (in bold) together with standard deviations that refer to the scatter of the independent measurements are also shown. Total enrichments E_{50} and E_{49} are inferred from the isotopomer data in the first four columns according to mass balance. In the last line the normalized (see the main text for details) isotopomer specific enrichments are compared to the total isotope fractionation values measured with the mass spectrometer.

Photolytic Recycling							
#	Date	E^a_{50} (%)	E^s_{50} (%)	E^a_{49} (%)	E^s_{49} (%)	E_{50} (%)	E_{49} (%)
1	23.07.04	21.92(31)	-	19.03(23)	1.10(59)	-	13.05(18)
2	29.07.04	22.10(20)	1.85(28)	19.29(23)	1.71(51)	15.35(16)	13.43(14)
3	02.08.04	22.61(67)	1.29(40)	19.16(60)	1.92(58)	15.51(21)	13.41(17)
4	28.10.04	21.42(21)	2.30(19)	18.62(28)	1.31(35)	15.05(15)	12.85(19)
$\bar{E}_{u(g/w)}$ (%):		**22.01(43)**	**1.81(42)**	**19.02(25)**	**1.51(32)**	**15.30(19)**	**13.18(24)**
$\bar{E}_{u(g/s)}$(%):		15.69 (62)	1.81 (42)	14.50 (38)	1.51 (32)	11.06 (75)	10.17 (50)
$\bar{E}_{u(MS)}$ (%):		-	-	-	-	10.90 (48)	10.08 (26)

Table 6.3.: Spectroscopic results of the leftover ozone from the O_3 photolytic dissociation experiment. The notation is the same as in Table 6.1. In the last row the normalized enrichments (at $t = t_{1/e}$) are given. Subscripts i and f indicate initial and final ozone.

	Ozone Isotopomers									
SW	666		668		686		667		676	
	$\bar{R}_{f/i}$	e_r (%)	$\bar{R}_{f/i}$	e_r (%)	$\bar{R}_{f/i}$	e_r (%)	$\bar{R}_{f/i}$	e_r (%)	$\bar{R}_{f/i}$	e_r (%)
I	0.7399	0.15	0.7556	0.58	0.7464	0.32	0.7546	0.25	0.7437	0.96
III	0.7531	0.11	0.7770	0.25	-	-	0.7607	0.08	0.7583	0.39
$\bar{E}_u$ **(%):**			**2.99**	(39)	**0.88**	(35)	**1.18**	(37)	**0.67**	(37)
$\bar{E}_u(t_{1/e})$ **(%):**			**1.89**	(25)	**0.56**	(22)	**0.75**	(24)	**0.42**	(24)

With this additional isotopic fractionation in mind, we now turn to the calculation of the relative rate coefficients. k_{6+6x} can be derived without the need of any symmetry specific measurement from Eq. 6.7 when the corresponding homonuclear rate coefficient (reaction (6.2a)) has already been determined:

$$\frac{k_{6+6x}}{k_{6+66}} = \frac{3}{2}(1 + E_u) - \frac{1}{K_x}\frac{k_{x+66}}{k_{6+66}} . \tag{6.12}$$

For further discussions, however, it will be useful to treat reactions (6.2c) and (6.2d) as independent channels (specifying the symmetry of the product molecule) with individual rate coefficients. The relative rates can be calculated from Eq. 6.8a and 6.8b, respectively, which yield

$$\frac{k^a_{6+6x}}{k_{6+66}} = 2(1 + E^a_u) - (1 - \gamma)\frac{2}{K_x}\frac{k_{x+66}}{k_{6+66}} , \tag{6.13a}$$

$$\frac{k^s_{6+6x}}{k_{6+66}} = 1 + E^s_u - \gamma\frac{2}{K_x}\frac{k_{x+66}}{k_{6+66}} . \tag{6.13b}$$

The equilibrium constant for the isotopic exchange reactions (6.3a) and (6.3b), which is furthermore required for the determination of the rate coefficients, has been evaluated with an estimated accuracy of better than 1 ‰, by incorporating higher order approximations like ro-vibronic interaction, centrifugal distortion and anharmonic correction in the calculation of the partition functions [*Richet et al.*, 1977]. Additionally, the following parameterizations for K_8 and K_7 have been found to reproduce the computed values with a fractional deviation less than $2 \cdot 10^{-5}$ in the temperature interval between 200 and 500 K

$$\begin{aligned} K_8 &= 1.9481 \exp(31.652\,\mathrm{K}/T)\left[1 - 1.28 \cdot 10^{-5}(T/\mathrm{K}) + 2.32 \cdot 10^{-8}(T/\mathrm{K})^2\right] , \\ K_7 &= 1.9727 \exp(16.930\mathrm{K}/T)\left[1 - 6.79 \cdot 10^{-6}(T/\mathrm{K}) + 1.20 \cdot 10^{-8}(T/\mathrm{K})^2\right] . \end{aligned} \tag{6.14}$$

and were used for the determination of the rate coefficients.

By inserting the derived symmetric specific enrichment values E_u^a and E_u^s given in Table 6.2 into Eqs. (6.13a) and (6.13b) and using the equilibrium constants K_x determined at 295 K, and, finally adopting the value of $\gamma = 0.006$ [*Janssen et al.*, 1999] for the $^{49}O_3$ isotopologue, too, the rate coefficients for the ozone formation in reaction channels involving heteronuclear oxygen molecules are obtained. The calculated values are listed in Table 6.4.

Table 6.4.: Summary of the obtained low-pressure recombination rate coefficients of $^{49}O_3$ and $^{50}O_3$ produced in ^{16}O-^{17}O-^{18}O mixture by visible light photolysis. The measured isotopologue enrichments are also included. Error limits represent 1σ uncertainties.

Molecular mass	$\bar{E}_u$ (%)	Relative rate coefficient		
		Reaction	Direct Value[a]	Corrected Value[b]
49	10.3	(R2c) $^{16}O + {}^{16}O^{17}O \longrightarrow {}^{16}O^{16}O^{17}O$	1.309 ± 0.008	1.292 ± 0.019
		(R2d) $^{16}O + {}^{17}O^{16}O \longrightarrow {}^{16}O^{17}O^{16}O$	1.009 ± 0.003	1.005 ± 0.010
50	11.1	(R3c) $^{16}O + {}^{16}O^{18}O \longrightarrow {}^{16}O^{16}O^{18}O$	1.469 ± 0.013	1.426 ± 0.034
		(R3d) $^{16}O + {}^{18}O^{16}O \longrightarrow {}^{16}O^{18}O^{16}O$	1.013 ± 0.004	1.007 ± 0.013

For reactions involving heteronuclear oxygen molecules the relative reaction probability is shown while relative rate coefficients are obtained by dividing the quoted numbers by two.
The enrichments values were measured at 295 ± 2 K

[a] Isotopic effects due to the ozone photodissociation are neglected.

[b] Isotopic effects from the side reactions are considered (see Eq. 6.10). Error limits also include the systematic uncertainties in the isotopic composition of the reference material (see discussion in Chapter 4, page 57).

These data confirm the earlier idea that, due to their large rate coefficient advantage of 30 to 40 %, the reaction channels (R2c) and (R3c) are responsible for the observed fractionation in the $^{49}O_3$ and $^{50}O_3$ isotopologues. In the case of $^{50}O_3$ it was revealed that the asymmetric molecules formed in reaction (R3c), due to the large rate coefficient advantage of ≈ 45 %, are responsible for the enrichment in the $^{50}O_3$ isotopologue measured by mass spectrometer.

Comparing these results with the existing spectroscopic data [*Anderson et al.*, 1989; *Janssen et al.*, 1999], which show small (1.9 - 5.4 % and 9.5 %, respectively) but not negligible enrichment in the symmetric $^{50}O_3$ isotopomer, however reveals a striking difference regarding the symmetric species. However, it should be mentioned that while the present experiment, which used VIS-light photolysis of ozone in the Chappuis band to generate O-atoms for ozone formation, till the earlier studies utilized an electric discharge in molecular oxygen to produce ozone.

One explanation for the difference between the two data sets would be that photolysis of ozone gives rise to an isotope effect that compensates the fractionation of the symmetric species in ozone formation. However, this seems unlikely if we consider the results of the experiment where pure ozone has been photolyzed in the Chappuis band (see Table 6.3). A slight isotope effect, less than 1 %, was found, but this leads to an additional enrichment rather than to a depletion of the symmetric isotopomers.

Therefore, it is more likely that ozone generation by electric discharge causes an extra enrichment. In order to test this hypothesis, three ozone samples generated in

a high-pressure electric discharge have been analyzed by the TDLAS. The summary of all the three ozone samples is listed in Table 6.5 (spectroscopic results of individual ozone sample are given in the Appendix.).

Table 6.5.: Isotopomer specific enrichments of the ozone samples produced in high-pressure electric discharge. The notation is the same as in the Table 6.2.

Electric Discharge							
#	Date	E^a_{50} (%)	E^s_{50} (%)	E^a_{49} (%)	E^s_{49} (%)	E_{50} (%)	E_{49} (%)
1	27.09.04	25.03(34)	5.21(30)	19.95(36)	2.71(21)	18.42(25)	14.20(25)
2	30.09.04	24.39(24)	5.89(45)	19.61(32)	3.15(29)	18.22(22)	14.12(23)
3	12.11.04	24.80(22)	4.83(24)	20.11(19)	2.63(22)	18.15(17)	14.28(15)
$\bar{E}_u$ (%):		**24.74(32)**	**5.31(54)**	**19.89(25)**	**2.83(28)**	**18.26(14)**	**14.20(08)**
$E_{u(g/s)}$ (%)		18.48 (31)	5.31 (54)	15.32 (41)	2.83 (28)	14.09 (35)	11.16 (33)
$E_{u(MS)}$ (%)		-	-	-	-	14.09 (86)	11.20 (51)

Interestingly, the symmetric isotopomers of ozone produced by electric discharge, indeed, show an accentuated enrichment. Therefore, a good agreement can be observed between the past laser spectroscopic measurements and the present work. In these measurements, the striking consistency between mass spectrometer and diode laser measurements is once more confirmed. However, the question as to what the origin of the higher enrichments in the electric discharge is, remains unanswered at present. It is only mentioned that *Valentini* [1987] originally proposed electric discharges in oxygen to be a source of oxygen isotope anomalies due to the presence of non - adiabatic collision-induced isotope fractionation between ground state O_2 and $O_2(^1\Delta_g)$. Nevertheless, this hypothesis remains unexaminable at the moment and may be the subject of future research.

Having established the consistency of previous experiments, the origin of the large variability (see Table 6.4) in the derived rate coefficients is discussed now. Recently, this variability of rate coefficients has been attributed to the difference in the zero-point energies (ZPE) of the oxygen molecules participating in a specific isotope exchange reaction that otherwise would result in an ozone molecule [*Janssen et al.*, 2001]. Details of this correlation may give insight into the physics of the fractionation mechanism as well as the dynamics of the ozone formation process.

Let us consider the following overall ozone formation mechanism:

$$X + YZ \rightleftharpoons (XYZ)^* \rightleftharpoons XY + Z \tag{6.15}$$

Here, the metastable state $(XYZ)^*$ can be formed from both sides and can decay either to the right or left. The bimolecular association together with the reverse unimolecular redissociation reactions is part of this reaction. When different isotopes of oxygen (X, Y, and Z) are involved, the ZPE of the O_2 molecules on the right- and left-hand sides differ, and reaction (6.15) can thus be slightly exothermic or slightly endothermic. The vibrationally excited molecule $(XYZ)^*$ can also be stabilized into ozone by collision with an inert molecule M.

Given the experimental fact that ozone formation is an end-on process, a one-to-one correspondence between ozone formation and oxygen exchange reactions for all reactions involving homonuclear diatoms follows. The energetic ozone molecule formed in collisions, where the O-atom is isotopically different from the diatom, will either lead to a stabilized asymmetric ozone molecule or, most of the time, will undergo dissociation via one of two exit channels which differ in ZPE of the product oxygen molecule. Endothermic exchange reactions ($\Delta(\mathrm{ZPE}) < 0$) such as the back reaction of (R2c or R3c, see Table 6.4) imply large rate coefficients, while exothermic reactions correlate with small rate coefficients. Considering the entrance and exit channels of an isotope exchange reaction, in an endothermic process the exit channel has an energy barrier due to the higher zero-point energy of the product diatom. This will result in a longer lifetime of the collision complex, and thus, to an increased probability of becoming stabilized to an ozone molecule. With further constraints the above discussion holds for the reactions involving heteronuclear diatoms, too [*Janssen et al.*, 2001].

The substantial number of measured rate coefficient data permits to draw a rather consistent picture about the origin of the isotope effect in ozone. The zero-point energy change in the isotope exchange reactions determines the lifetime of the collision complex and thus its probability to become stabilized to ozone. This process is independent of the mass of the produced ozone molecule and favors endothermic exchanges. Considering the newly determined rate coefficients of the $^{49}O_3$ and $^{50}O_3$ formation reactions involving the heteronuclear channels, the validity of the above presented concept can be tested. Taking $^{49}O_3$ as an example, this isotopologue is produced in a well-mixed oxygen gas via reactions (R2a) – (R2d) (see Table 1.2) whenever oxygen atoms are available. However, fast isotope exchange reactions will rapidly recycle the atoms through many molecules before ozone is produced by collisional stabilization of an atom-diatom pair. As it was pointed out in Chapter 4, at gas pressures used in photolytic recycling experiments, the exchange reactions are about 10^4 times faster than ozone formation. The equation that describes the isotope exchange equilibrium is:

$$^{17}O + {}^{16}O{}^{16}O \rightleftharpoons {}^{17}O{}^{16}O + {}^{16}O \tag{6.16}$$

The equilibrium constant for the isotope exchange reaction can be calculated (see on page 80); forward reactions are slightly faster than the back reactions since the zero-point energies of the molecules on the left side are higher by $11.67\,\mathrm{cm}^{-1}$ than those on the right which are tighter bound. Left-to-right processes are exothermic, the reverse processes are endothermic. Comparing the rates of ozone formation from Table 6.4 with the enthalpy of the competing exchange reaction, indeed, it is found that ozone is enhanced by a factor of 1.3 when the exchange is endothermic (see reaction channel (R2c)), otherwise comparably small effects are observed. For convenience, the relative rate coefficients are plotted *vs.* ZPE differences in oxygen molecules of the corresponding isotope exchange reactions (see Figure 6.1).

The good agreement between the existing results and the new data for the $^{49}O_3$ and $^{50}O_3$ isotopologues provides the important information that the concept of a linear

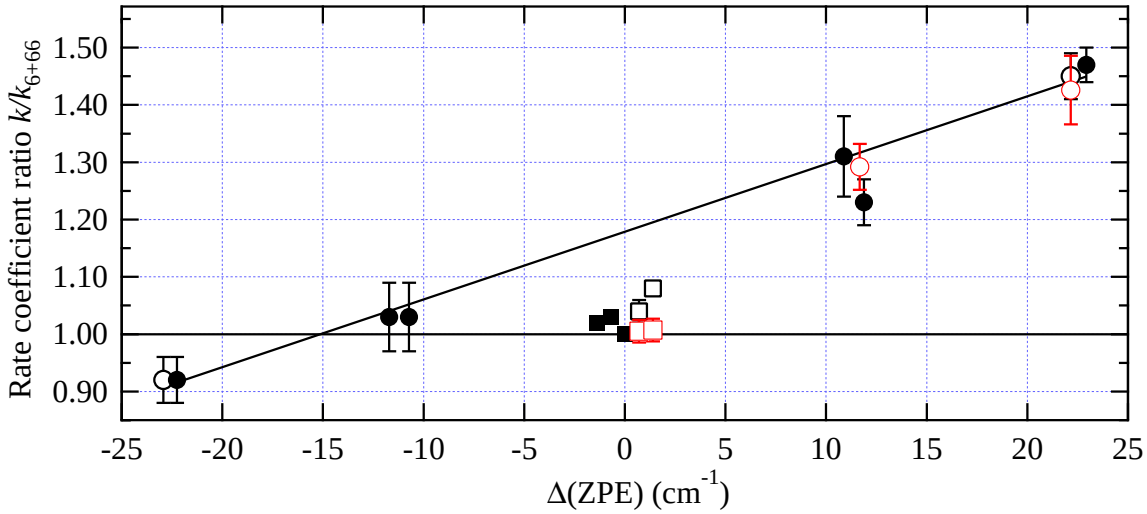

Figure 6.1.: Relative rate coefficients *vs.* ZPE differences in oxygen molecules of the corresponding isotope exchange reactions adopted from *Janssen et al.* [2001]. Error bars represent 1σ statistical uncertainties. The exothermic (slow ozone formation) or endothermic (fast ozone formation) isotope exchange reactions (circles) are collisions with homonuclear diatoms (●) and heteronuclear molecules (○). The energetically neutral (Δ(ZPE) = 0) collisions (squares) resulted from collisions with homonuclear oxygen (■) and heteronuclear molecules (□) can be clearly distinguished from the former reactions. The red symbols are the rate coefficients measured within this work. The line is a best fit to the collisions with homo- and heteronuclear oxygen molecules. The neutrals (shifted in ZPE for clarity) are well below the fit and show almost no deviation from the standard reaction.

correlation between the rate coefficients involving the exo- and endothermic isotope exchange reactions and the zero-point energy change in these reactions, is obviously correct. It further confirms that there is a symmetry selection in the formation process, which favors the formation of asymmetric molecules. This is manifested in the offset ($\sim$ 0.17) of the line connecting the rate coefficients for asymmetric molecule formation compared to those for the symmetric molecules. Such symmetry selection was first suggested by *Hathorn and Marcus* [1999] who explained it in terms of symmetry dependent energy redistribution in the excited ozone complex.[1] The argument why the symmetric complexes XYX are less efficiently stabilized than the asymmetric ones YXX or XYZ assumes that, because of the lower density of states, the coupling between the ro-vibrational states is weaker for the symmetric complexes. However, this hypothesis needs to be investigated in order to assign a real physical meaning to the η parameter.

Turning back to the Figure 6.1, another important detail can be observed when the newly obtained rate coefficient of reaction that forms the singly substituted symmetric $^{16}O^{18}O^{16}O$ molecule is compared with the earlier rate coefficient measured using ozone

[1] An *ad hoc* parameter $\eta = 1.18$, which effectively reduces the formation rates of the symmetric XYX ozone molecules, has to be introduced in order to obtain good agreement with the measured rate coefficients [*Gao and Marcus*, 2001].

produced in an electric discharge [*Janssen et al.*, 1999]. The former value is very close to the standard $^{16}O + {}^{16}O^{16}O$ reaction rate, and thus in better agreement with theoretical predictions *Gao et al.* [2002]; *Hathorn and Marcus* [1999]; *Schinke and Fleurat-Lessard* [2005]. A similar conclusion can be drawn for the rate coefficient of reaction that forms the $^{16}O^{17}O^{16}O$.

6.2. Isotope Transfer from Ozone into Carbon Dioxide

Recent investigations of stratospheric ozone samples using improved sample transfer and analysis revealed that the enrichments measured in these samples can be correlated with the results obtained in the laboratory studies when reasonable stratospheric temperatures are assumed. In an altitude range between 22 and 33 km enrichments range from 7 to 9 % for $^{49}O_3$ and from 7 to 11 % for $^{50}O_3$ [*Krankowsky et al.*, 2000].

Due to the reactivity of ozone, an isotope transfer into other atmospheric oxygen containing compounds can occur. For example, the isotope ratios determined from stratospheric CO_2 samples resulted in a surprising relationship: a gradient for $\delta^{17}O/\delta^{18}O$ of about 1.7 was found [*Lämmerzahl et al.*, 2002]. This clearly shows that there is a preferred incorporation of ^{17}O over ^{18}O into CO_2. A detailed kinetical model to describe such an isotope transfer process has not yet been developed.

Yung et al. [1991] proposed a mechanism for the transfer of the anomalous oxygen isotope signature from O_3 to CO_2. In their scheme, $O(^1D)$ radicals from UV photolysis of O_3 and CO_2 form short-lived CO_3^* intermediates, which pre-dissociate into $CO_2 + O(^3P)$ and thus allow for an isotope transfer:

$$^{16}O_2{}^xO + h\nu(\lambda < 315\,\text{nm}) \rightarrow {}^xO(^1D) + {}^{16}O_2(^1\Delta_g) \tag{6.17}$$

$${}^xO(^1D) + C^{16}O_2 \rightarrow (C^{16}O^{16}O^xO)^* \rightarrow C^{16}O^xO + {}^{16}O(^3P) \tag{6.18}$$

This scheme may be completed by an exchange reaction that was only recently established [*Perri et al.*, 2003]:

$${}^xO(^1D) + C^{16}O_2 \rightarrow (C^{16}O^{16}O^xO)^* \rightarrow C^{16}O^xO + {}^{16}O(^1D) \tag{6.19}$$

Only two sets of laboratory experiments have been published to date that investigate this isotope transfer process in detail. The first study [*Wen and Thiemens*, 1993] confirmed that isotope exchange occurs but concluded that additional mass independent fractionation processes associated with the CO_3^* intermediate must contribute.

The second set of experiments [*Johnston et al.*, 2000] was able to determine the final equilibrium value of the $CO_2 + O(^1D)$ reaction from the temporal evolution of the CO_2 and O_2 reservoirs. Similar to the atmosphere, O_3 was in a dynamic isotopic equilibrium with O_2 in these experiments. The results indicate that while the isotopic composition of the CO_2 reservoir is qualitatively controlled by the isotopic composition of the $O(^1D)$ reservoir (like in a two-component mixing proposed by *Yung et al.*), there should be other contributing factors.

To date, at least four different mechanisms have been proposed to explain the oxygen isotope transfer from O_3 to CO_2 [*Brenninkmeijer et al.*, 2003]:

1. Simple statistical mixing between the CO_2 and the $O(^1D)$ reservoirs

2. Isotope transfer, including an additional mass-dependent fractionation process in the CO_3^* complex.

3. Isotope transfer, including an additional mass-independent fractionation process in the CO_3^* complex

4. An additional (*e.g.*, mesospheric) source of the mass-independent anomaly in stratospheric CO_2

From the molecular perspective, isotope transfer according to 6.17 - 6.18 is governed by two important effects: first, the isotopic composition of the $O(^1D)$ reactant, and second, possible fractionation mechanisms in the formation and/or dissociation of the CO_3^* complex. If the former is known, the latter could be derived, and thus a decision can be made between the proposed mechanisms.

Even though the isotopic composition of $O(^1D)$ is hardly accessible in an experiment, some clues about its role may be inferred from the asymmetric ozone, which is the precursor molecule of heavy $O(^1D)$. This is due to the fact that the $O(^1D)$ is preferentially formed from the terminal oxygen atoms in ozone [*Sheppard and Walker*, 1983]. Hence, E_u^a is a direct measure of the heavy atom transfer potential.

In collaboration with the Atmospheric Isotope Physics group headed by *T. Röckmann* the investigation of the oxygen isotope transfer mechanism from O_3 to CO_2 by the TDLAS technique has been undertaken for the first time.

The experiments in which a mixture of 10.5 μmol isotopically well characterized CO_2 and 5.3 mmol oxygen gas of natural isotopic composition are brought to temperatures of about $-75\,^\circ$C and irradiated by a pen-ray Hg-lamp with primary emission peaks at 184.9 and 253.7 nm are part of another PhD thesis [*Shaheen*, 2005]. For a detailed presentation of the experimental procedures and set-up, the reader is asked to consult that work.

An experimental run took about 6 days, enough time to isotopically equilibrate the CO_2 with the buffer O_2. The isotopic composition of the initial as well as the isotopically equilibrated CO_2 has been determined with a commercial high precision isotope ratio mass spectrometer (Delta^{XL}Plus *ThermoQuest Finnigan*). When the illumination was stopped the ozone generated during irradiation was collected together with the CO_2 and separated from the molecular oxygen. This sample was transferred to the evacuated multipass cell of the TDLAS. Beforehand, first reference ozone was prepared from the same oxygen gas that was used in the CO_2 experiment in a low-pressure electric discharge and then analyzed. The scanning procedure was similar to that described before. Only the spectral analysis had to be modified in order to account for the line broadening effect due to the presence of the CO_2 buffer gas. Therefore, the Voigt shape function was implemented in the fit model. The summary of the spectroscopic investigation is given in Table 6.6. Note that the listed values

Table 6.6.: Isotopomer specific enrichments of ozone resulted from the isotope transfer experiment. Isotope fractionation values ($\bar{E}_u$) are the weighted means of individual E_u values determined separately for each spectral window (SW). Their estimated standard deviations are given in parentheses. Total enrichments E_{50} and E_{49} are inferred from the isotopomer data in the first four columns according to Eq. 6.9.

Ozone from Isotope Transfer Experiment						
#	E^a_{50} (%)	E^s_{50} (%)	E^a_{49} (%)	E^s_{49} (%)	E_{50} (%)	E_{49} (%)
1	19.38(20)	0.05(16)	17.04(15)	1.89(20)	12.92(29)	11.99(25)

are related to the reference material. Normalization to the isotopic composition of the oxygen gas used in the experiments is done with the assumption that only the asymmetric molecules are fractionated in the reference material ($\beta = 0$). The effect of systematic uncertainties in the composition of the reference ozone are explored by considering the limiting case of $\beta = 0.12$ (see discussion in Chapter 4, page 57). An insight into the $CO_2 + O(^1D)$ reaction mechanism is gained by plotting the isotopic compositions of the ozone obtained during illumination along with initial and final CO_2 compositions (Figure 6.2).

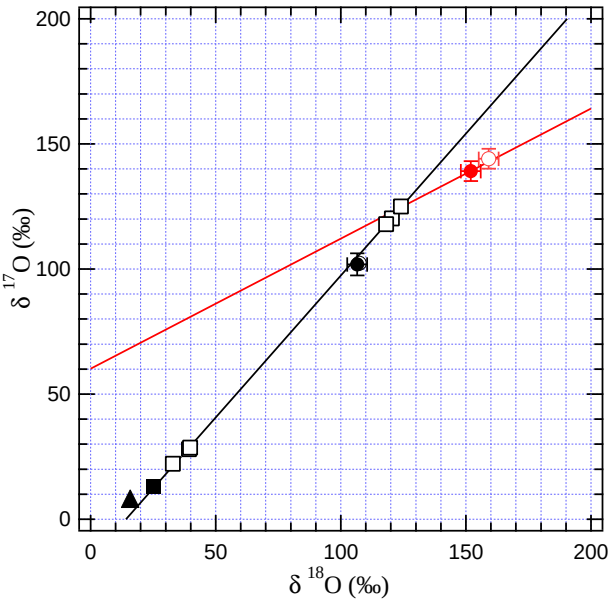

Figure 6.2.: A three-isotope plot with the isotopic composition of initial CO_2 (■), O_2 (▲) and O_3 (●). Asymmetric ozone is marked by a red symbol, while a black symbol indicates the total ozone. For ozone, solid symbols represent the case $\beta = 0$. The limiting case of $\beta = 0.12$ is also indicated (open symbol). Isotopically altered CO_2 is marked by (□) and equilibrated CO_2 is given by the same symbol with the highest δ values. The line connecting the isotopic composition of initial carbon dioxide with the isotopically equilibrated CO_2 has a slope of 1.13, while the line, which connects the asymmetric ozone with the isotopically equilibrated CO_2 follows the fundamental mass-dependent fractionation law, *i.e.*, has a slope of 0.52. Error bars represent 2σ statistical uncertainties.

Even though, the experimental conditions were selected such that they approximately simulate stratospheric conditions, the observed evolution of the oxygen isotopic composition in CO_2 follows the relation $\delta^{17}O = 1.13\ \delta^{18}O$, instead of that observed in the stratospheric CO_2 samples. However, this isotopic composition already shows a strong deviation from the mass-dependent fractionation line, indicating that the anomalous isotope fractionation from ozone is transferred to the CO_2 molecules. The most important information, however, resides in the key element of the isotopic transfer reaction: in the source of the $O(^1D)$, *i.e.* in the asymmetric ozone isotopologues.

Interestingly, a standard mass dependent fractionation line with a slope of 0.52 already connects the asymmetric ozone and the equilibrated CO_2. This indicates that all processes subsequent to ozone formation – from ozone photolysis to the isotope transfer reaction – show a standard mass dependence instead of involving a mass independent step in the mechanism as proposed earlier [*Wen and Thiemens*, 1993]. This conclusion holds even when the limiting case of $\beta = 0.16$ is assumed.

Presently, it can be concluded that there is no evidence for any anomalous isotope physics in the photolytic dissociation reaction and the $CO_2 + O(^1D)$ reaction. Finally, what causes the stratospheric observations remains a puzzle and requires further investigation.

7. Summary and Conclusions

The goal of the present work was first to develop a diode laser spectrometer for sensitive and simultaneous detection of naturally occurring ozone isotopomers and then to investigate the unusual ozone isotope effect in ozone formation and possible transfer pathways of the effect into other molecules.

Through careful selection and modification of an astigmatic mirror multipass absorption cell, a limit sufficient for the detection of even the rare isotopomers $^{16}O^{17}O^{16}O$ and $^{16}O^{16}O^{17}O$ was achieved in combination with an extended ozone lifetime. A long lifetime is a fundamental requirement for precise measurements that require integration of the order of one to two hours. Furthermore, a high precision frequency calibration method for individual ro-vibrational transitions of the ν_3 fundamental of ozone at $1000\,\mathrm{cm}^{-1}$ was developed. A relative precision of 5×10^{-8} was achieved on the frequency scale even within a single spectrum. This degree of precision was necessary not only for the unambiguous identification of individual transitions, but it also was a requirement for the quantitative determination of isotopomer abundances.

With these innovations a precision of 0.3 % ($1\,\sigma$ error) was achieved for the measurement of individual ozone isotopomer abundances. This value was confirmed in a comparison with mass spectrometer measurements, which naturally lack the ability of detecting individual isotopomers, but allow for precise measurement of isotopologue abundances.

Currently, the accuracy of ozone isotopomer investigations is limited by systematic uncertainties that were also explored in detail. Most importantly, uncertainties in the composition of the standard ozone mixture used to derive the isotopomer abundances in ozone samples, were investigated and their effect was estimated. From theoretical modelling of isotopic effects in ozone formation [*Gao et al.*, 2002; *Schinke and Fleurat-Lessard*, 2005] an upper limit on the effects of the isotopic standard is deduced that gives an accuracy of 0.74 % and 0.54 % in the measurements of $^{16}O^{16}O^{18}O$ and $^{16}O^{16}O^{17}O$, respectively. These values have to be compared to the signatures of 22 and 19 %, which are typical for the measurements. As the comparison with mass spectrometer measurements shows, the determination of total isotopologue contents, *i.e.* of $^{16}O_2{}^{18}O$ or $^{16}O_2{}^{17}O$ for example, is only marginally ($\leq 0.1\,\%$) affected by this uncertainty.

In order to characterize the isotope effects in the kinetic process of ozone formation $O + O_2 + M \rightarrow O_3 + M$, the absorption spectrometer was utilized to analyze ozone samples that were generated under different conditions. Ozone was generated by photolysis recycling, which assures reactants to be in their electronic ground states, but suffers from effects in the photolytic decomposition of ozone. In order to investigate the influence of the decomposition reaction, a control experiment was performed. Photolytic effects have been found to be non-vanishing, but much smaller than iso-

topic effects in the formation reaction. From these values a set of new and refined rate coefficients was derived: Relative to the reaction $^{16}O + {}^{16}O^{16}O \rightarrow {}^{16}O^{16}O^{16}O$, the rate coefficients of the channels $^{16}O + {}^{16}O^{17}O \rightarrow {}^{16}O^{16}O^{17}O$ and $^{16}O + {}^{17}O^{16}O \rightarrow {}^{16}O^{17}O^{16}O$ were determined to be 1.292 ± 0.019 and 1.005 ± 0.010, and those of the channels $^{16}O + {}^{16}O^{18}O \rightarrow {}^{16}O^{16}O^{18}O$ and $^{16}O + {}^{18}O^{16}O \rightarrow {}^{16}O^{18}O^{16}O$ were found to be 1.426 ± 0.034 and 1.007 ± 0.013.

The newly obtained coefficients bring out the influence of zero point energy differences in the ozone dissociation channels on the rate of ozone formation even more clearly than before. They suggest that a linear curve very well describes the correlation between the ZPE differences and the normalized rate coefficients of the reactions forming asymmetric molecules. Moreover, the rate of reactions that form the singly substituted symmetric molecules are close to that of reaction $^{16}O + {}^{16}O^{16}O$. This resolves a previously unexplained discrepancy between theory and experiment [*Janssen et al.*, 2001]. The discrepancy is mainly due to a significant difference in the isotopic composition of ozone prepared by photolytic recycling and of ozone from an electric discharge. The differences in the ozone formation conditions fundamentally affect the abundance of the symmetric molecules that are significantly enriched in the latter samples. Thus, the current belief that these samples mainly differ in the temperatures at which ozone is formed but not in the chemical kinetics was shown to be in error. Since up to now only measurements exist that utilized ozone formed in electric discharges [*Anderson et al.*, 1989; *Janssen et al.*, 1999], existing laboratory predictions [*Janssen*, 2005] on the relative abundance of symmetric and asymmetric ozone molecules suffer from this systematic bias.

The finding that symmetric ozone is not enriched in the process of O_3 formation, appears to contradict the most precise atmospheric observation [*Meier and Notholt*, 1996] of the ozone isomeric distribution in which significant enrichment (11 %) of the symmetric $^{16}O^{18}O^{16}O$ molecules was derived. However, these retrievals rely on the accuracy of linestrengths listed in the HITRAN spectroscopic database, which may suffer from substantial uncertainty (see discussion in Chapter 5, on page 63) due to a number of assumptions used in the linestrength calculations that may not be valid. At least the assumed statistical ratio of 2 between the asymmetric and symmetric ozone molecules is not supported by the present work. Another possibility to explain the discrepancy would be to assume an additional isotopic effect in the ozone formation at stratospheric conditions.

Finally, the characteristics of the isotope transfer from ozone into carbon dioxide was studied in a collaborative effort with the Atmospheric Isotope Physics group at the MPI für Kernphysik. The symmetry resolved analysis of heavy ozone revealed that CO_2 which derives from isotope transfer with $O(^1D)$ generated in ozone photolysis, acquires its isotopic composition in a standard mass-dependent manner. This is in contrast to earlier experiments [*Wen and Thiemens*, 1993], which concluded that the isotope transfer occurs in a non-standard way, without actually resolving the symmetry of the ozone molecules involved. Clearly, more investigations are needed, especially to explain the isotopic signature of stratospheric CO_2. Nevertheless, this measurement once more demonstrates that the large and unusual isotope effect observed in the formation of ozone appears to be unique, rather than of a general nature.

A. Validation of the Frequency Calibration

The calibration of the frequency scale has been carried out by using a fixed, internally coupled FP confocal etalon in combination with selected O_3 absorption lines. The calibration procedure was briefly discussed in Chapter 3. Here, the accuracy of the method is tested by generating an independent frequency scale from very accurately known CO_2 absorption lines and determining the ozone absorption line positions, which can then be compared with the database values.

Due to its important laser transitions in the 10 micron spectral region, the absorption line positions of CO_2 have been subject of a number of very accurate frequency measurements [*Bradley et al.*, 1986; *Claveau et al.*, 1999; *Freed et al.*, 1980; *Maki et al.*, 1994; *Teffo et al.*, 2002]. Thus, CO_2 is an ideal candidate for the diode laser frequency calibration in that frequency range [*El-Sherbiny et al.*, 1979]. The only drawback using CO_2 absorptions as standard reference lines is that, being a linear molecule, carbon dioxide has a very sparse absorption spectrum.[1] Therefore, a special mixture of different CO_2 isotopologues has been prepared in order to have at least four to five absorption lines within a laser mode. Figure A.1 shows the experimental set-up that was used for the isotopic scrambling. The method is relatively straightforward: A 2 l glass bulb is employed as a reaction chamber to which four high pressure flasks are attached. Each of these flasks contains one of the following gases: $^{12}C^{16}O$, $^{13}C^{16}O$, $^{18}O_2$ and $^{17}O_2$, respectively. First, a given amount[2] of CO_2 is introduced into the chamber and frozen out by immersing the bottom side of the reaction chamber in LN_2. Residual gases are pumped away, and then the desired amount of O_2 is added. The gas pressure in the reaction chamber is monitored by a 10 Torr pressure gauge. After closing the bulb's valve, the CO_2 is released by removing the LN_2 dewar. An electric discharge, ignited between the inner tungsten electrodes attached to the glass bulb, dissociates the O_2 molecules, and the oxygen atoms undergo isotopic exchange reactions with CO_2. Repeated discharges, lasting for at least 20 minutes, assure a high efficiency of the isotope mixing. The resulting isotopically scrambled CO_2 species are easily separated from the O_2 bath by freezing them out. The leftover O_2 is removed by pumping. After repeating the scrambling procedure with different CO_2-O_2 gas mixtures and collecting them in a 0.5 l steel

[1] The spacing between the lines of the rotational fine structure of the symmetric molecules are equal to $4B$, where $B = 0.391\,\mathrm{cm}^{-1}$.

[2] The aim of the experiment is to prepare a mixture of different CO_2 isotopologues that has the following characteristics: it contains all the possible isotopologue variants, which have absorption features around $1040\,\mathrm{cm}^{-1}$, with each species having an abundance such that the associated absorption lines have approximately the same intensities.

cylinder, the following CO_2 isotopic species were finally obtained: $^{12}C^{16}O_2$, $^{13}C^{16}O_2$, $^{12}C^{18}O_2$, $^{13}C^{18}O_2$, $^{12}C^{16}O^{18}O$, $^{13}C^{16}O^{18}O$, $^{12}C^{17}O^{17}O$ and $^{12}C^{16}O^{17}O$. The approximate abundance of each species in the final mixture is given in Table A.1.

About 2 Torr of this CO_2 isotopic mixture was transferred from the steel cylinder to an optical cell, which has then been inserted into the main laser beam of the TDLAS (see Figure 3.1, page 25).

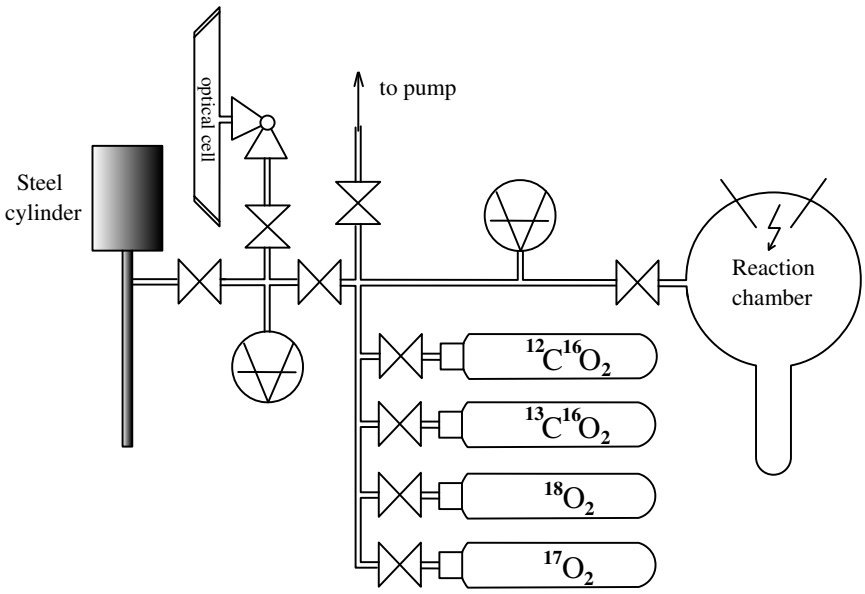

Figure A.1.: Schematic diagram of the experimental setup for CO_2 isotopic scrambling. The main components are: a glass bulb with tungsten electrodes that serves as reaction chamber, high pressure flasks of different O_2 and CO_2 isotopologues, capacitance manometers (10 Torr, MKS), a 0.5 l steel cylinder to collect the CO_2 mixtures, a turbo molecular pump (not shown) and an attachable optical cell, which is a 40 cm long glass tube with inner diameter of 3 cm. At both ends BaF_2 windows are fixed at the Brewster angle.

Table A.1.: The approximate abundance of individual isotopologues in the CO_2 isotopic calibration mixture.

	CO_2		Abundance
Nr.	Code[a]	Species	(%)
1	266	$^{12}C^{16}O^{16}O$	4.5
2	268	$^{12}C^{16}O^{18}O$	14.4
3	288	$^{12}C^{18}O^{18}O$	16.8
4	366	$^{13}C^{16}O^{16}O$	10
5	368	$^{13}C^{16}O^{18}O$	19
6	388	$^{13}C^{18}O^{18}O$	8.6
7	267	$^{12}C^{16}O^{17}O$	12.7
8	277	$^{12}C^{17}O^{17}O$	14

[a] AFGL shorthand notation.

Because of the low intensity[1] of the CO_2 absorption lines, the accurate line position measurements required second harmonic detection[2] ($2f$-detection). A sensitivity improvement of one order of magnitude in comparison to direct absorption spectroscopy has been achieved. Employing this detection technique, the etalon, reference and ozone spectra are simultaneously recorded. In the existing two channel configuration this is accomplished by introducing a very small amount (< 10 mTorr) of ozone in the multipass cell and recording an overlapped spectrum of CO_2 and O_3. A fit procedure (already presented in Chapter 3) is used to obtain the linearized, relative frequency scale (see Figure 3.8, page 34). In Figure A.2 a CO_2-O_3 spectrum is plotted against the relative frequency scale.

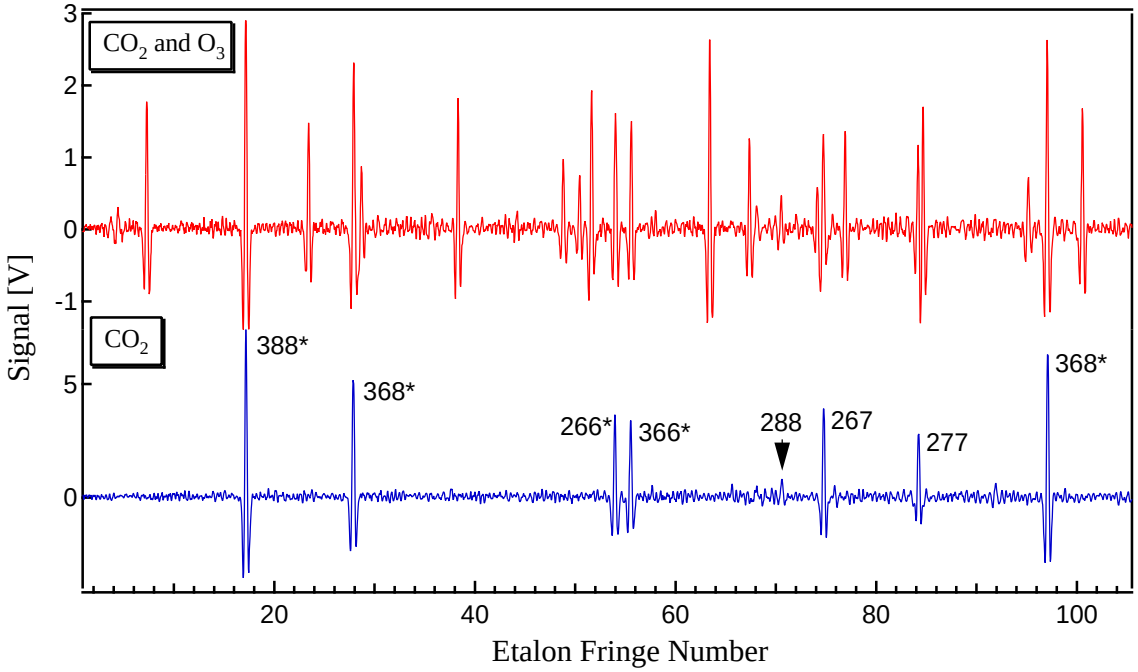

Figure A.2.: An example of overlapped CO_2-O_3 second derivative spectrum plotted against the linearized, relative frequency scale. (top panel). The pure CO_2 standard spectrum is given for identification purpose (bottom panel). The numbers represent the different CO_2 isotopic species (see Table A.1). A least-squares peak fitting procedure returns the position of the marked CO_2 absorption lines.

A least-squares fit, using second derivative Gaussian, returns the position of CO_2 absorption lines. These become the x values in a linear least-squares fit, which takes the high accuracy CO_2 line frequencies as the y values. The coefficients from the fit then yield the absolute frequency scale. One example is presented in Figure A.3. Performing a number of calibration procedures – similar to that presented above – in different frequency ranges, an accurate value of $(8.0248 \pm 0.0008) \cdot 10^{-3}\,\mathrm{cm}^{-1}$ for the etalon free spectral range has been determined.

[1] The line intensities range between $(0.2 - 3) \cdot 10^{-23}\,\mathrm{cm}^{-1}/(\mathrm{molecule\,cm}^{-2})$.

[2] In this technique the TDL output wavelength is internally modulated at a frequency f (1771 Hz), and the absorption signal is detected at a twice of this frequency using lock-in.

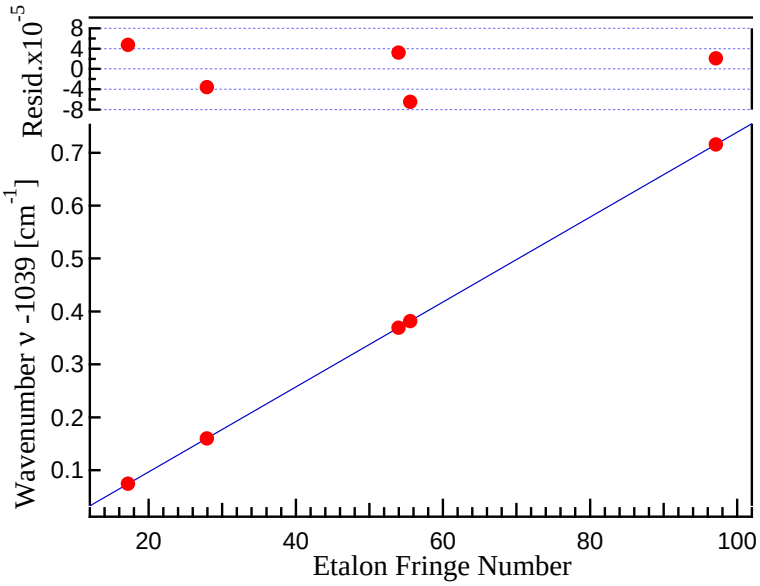

Figure A.3.: High accuracy CO_2 line frequencies from the literature are plotted *vs.* the line positions given in relative frequency units. The absolute frequency scale is obtained from the coefficients returned by a linear least-square fit. The slope defines the free spectral range (FSR) of the FPE.

Applying the calibration procedure presented above, the CO_2-O_3 spectrum is plotted versus the linearized, absolute frequency scale. Performing a least-squares fit on the ozone absorption lines, the frequency of each line position is obtained, and then compared with the values listed in the HITRAN database (Table A.2).

Table A.2.: Comparison of the peak fit results with the reference data. The CO_2 absorption lines that can be found in this spectral region are also listed. Line positions are given in cm^{-1}.

		O_3		
Nr.	CO_2 [a]	Fit	Reference [b]	$\Delta_{Ref-Fit}$
1.	1039.074230 [c]	1038.99413	1038.99410	-2.80E-05
2.	1039.159979 [c]	1039.12430	1039.12426	-4.39E-05
3.	1039.369319 [c]	1039.16640	1039.16639	-1.42E-05
4.	1039.381829 [c]	1039.24286	1039.24291	5.14E-05
5.	1039.502785	1039.32721	1039.32734	1.30E-04
6.	1039.536329	1039.34022	1039.34030	8.13E-05
7.	1039.612187	1039.44532	1039.44529	-2.78E-05
8.	1039.715515 [c]	1039.47720	1039.47723	3.11E-05
9.		1039.55356	1039.55353	-2.73E-05
10.		1039.74357	1039.74351	-5.70E-05

[a] The absolute frequencies of the II band CO_2 laser transitions were taken from *Bradley et al.* [1986] and *Claveau et al.* [1999].

[b] O_3 line positions are from the HITRAN database [*Rothman et al.*, 2005].

[c] CO_2 lines used for absolute frequency calibration. The remaining lines suffered from overlapping with O_3 absorption features.

The average deviation of the fit from the reference values is about $5 \cdot 10^{-5}\,cm^{-1}$.

Although, the database values of ozone line positions have been determined by high-resolution Fourier-transform spectroscopy (FTS), they may also suffer from uncertainty [*Rinsland et al.*, 2003, and references therein]. Thus, it is not clear whether the discrepancies are primarily due to inaccuracies in the calibration procedure presented or whether they also reflect experimental errors in the FTS results. Nevertheless, the accuracy of the ozone line positions, at least for the strong ones, must comply with the value of $5 \cdot 10^{-5}\,\mathrm{cm}^{-1}$. Therefore, they can be used as a frequency reference, too. However, the database does not specify the uncertainty range of the listed line positions. Thus, care must be taken using these lines for calibration. To avoid unexpected problems, the absolute frequency calibration performed is based on at least half a dozen of ozone reference lines (from 5 up to 8 in about $1\,\mathrm{cm}^{-1}$ spectral range) and the FSR value defined by the linear least-squares fit is compared with the accurately determined FSR of the FPE. The difference between the two values can be used as a measure for the accuracy of the calibration. An example where the frequency calibration is performed purely based on selected ozone lines is shown in Figure A.4. For the measured FSR an excellent agreement is found with the value determined from the CO_2 lines employing $2f$-detection. The good reproducibility is encouraging and gives firm support for the validity and accuracy of the calibration method.

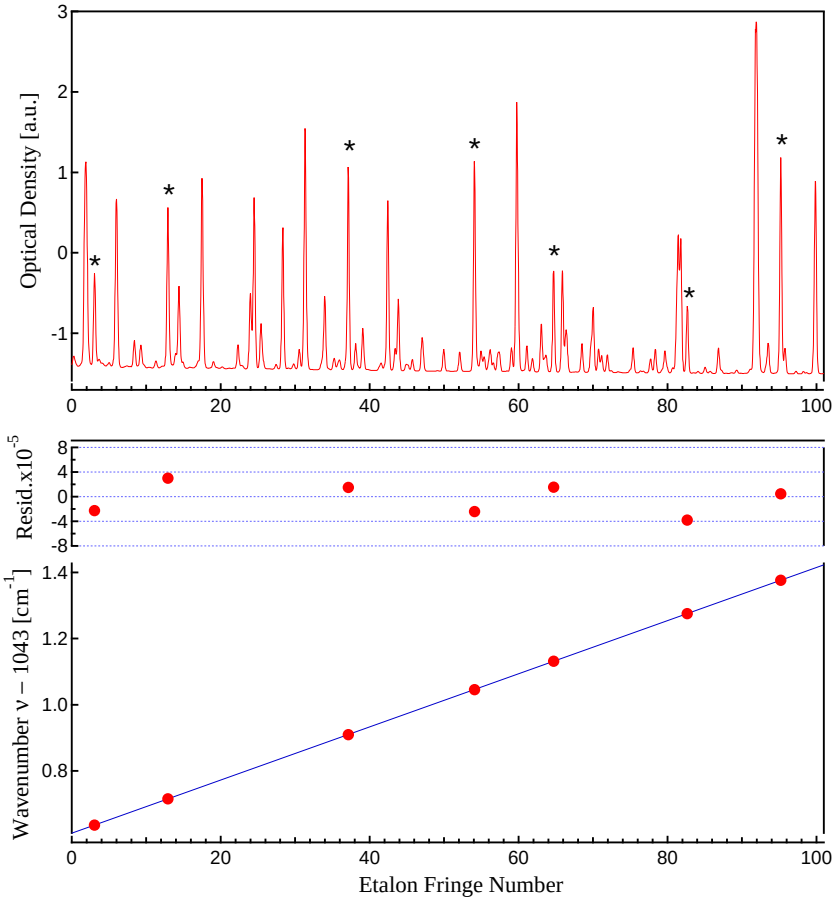

Figure A.4.: A direct absorption spectrum of O_3 around 1044 cm^{-1}. The frequency calibration is based on selected ozone absorption lines, marked by $(*)$. The FSR from the linear least-squares fit is $(8.0248 \pm 0.0003) \times 10^{-3}$ cm^{-1}. The residual plot assesses the extent of linearity of the relative frequency scale. For accurate line-shape measurements, a highly linear frequency scale is a fundamental requirement.

B. Propagation of Rays in an Astigmatic Mirror Multipass Cell

Optical interference fringe effects impose severe sensitivity restrictions on measurements of gas phase species using laser absorption methods. Typically, optical fringes occur when light which is scattered from different optical surfaces interferes with the primary beam. Due to the large number of reflections, fringes are especially common in systems using multipass cells (MPC). Although the MPC enhances the absorption signal, it also increases the likelihood of fringe generation. Therefore, a deeper understanding of the multipass cell as an optical system is crucial. On the one hand, it allows to optimize the cell configuration such that the fringe generation within the cavity is reduced. This is achieved by selecting proper cell geometries that spatially separate the multiple reflections within the cavity and thus, the spillover of light from the beam spots which neighbor the coupling hole on the cell's front mirror is minimized (details are given on page 30). Understanding the transmission properties of the MPC, on the other hand, can lead to an improved integration of the cell within the whole optical system.

Here, the geometry of the recirculating beam paths in the astigmatic mirror multipass cell is discussed after a brief review of the special case of a spherical mirror multipass cell.

In terms of ray optics a multipass cell consisting of two spherical mirrors with mirror radii R_1, R_2 spaced d apart, is equivalent to a biperiodic lens sequence with lenses of focal length $f_1 = R_1/2$ and $f_2 = R_2/2$ spaced at the same distance d (see Figure. B.1). The only difference between the two structures is that the ray path in the mirror system is folded back. In an optical system whose symmetry axis is in the z direction, a paraxial ray in a given cross-section (z=constant) is characterized by its distance x from the z axis and the angle x' it makes with that axis. In the paraxial ray approximation there is a linear relation between the parameters $x_1 x_1'$ and $x_2 x_2'$ of two different planes of the system:

$$x_2 = Ax_1 + Bx_1' \tag{B.1a}$$
$$x_2' = Cx_1 + Dx_1' \tag{B.1b}$$

or, in matrix notation

$$\begin{pmatrix} x_2 \\ x_2' \end{pmatrix} = \begin{pmatrix} A & B \\ C & D \end{pmatrix} \begin{pmatrix} x_1 \\ x_1' \end{pmatrix} \tag{B.2}$$

where the matrix containing the parameters A, B, C and D is called the ray transfer matrix. This ray transfer matrix allows to describe the properties of an optical system in general terms of the location of its focal points and principal planes.

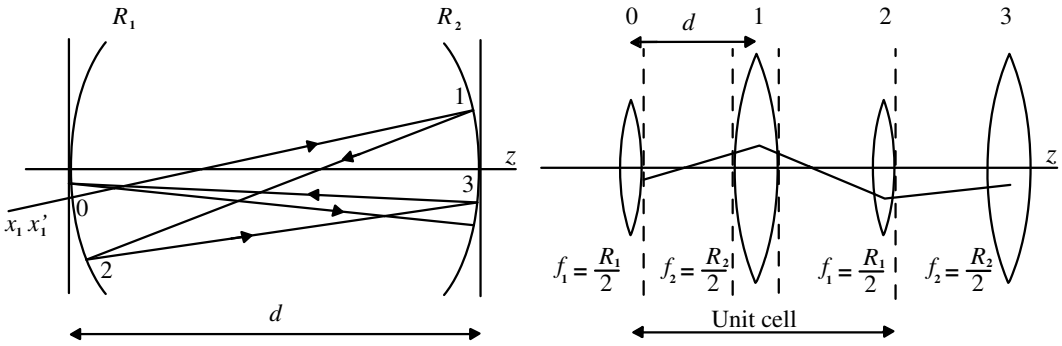

Figure B.1.: Curved mirror resonator and its equivalent biperiodic lens sequence

For example, the 'unit cell' of the above mentioned periodic structure can be expressed as

$$x_2 = Ax_1 + Bx_1', \qquad x_3 = Ax_2 + Bx_2', \tag{B.3a}$$
$$x_2' = Cx_1 + Dx_1', \qquad x_3' = Cx_2 + Dx_2', \tag{B.3b}$$

or in general for transmission through n sections

$$\begin{pmatrix} x_{n+1} \\ x'_{n+1} \end{pmatrix} = \begin{pmatrix} A & B \\ C & D \end{pmatrix}^n \begin{pmatrix} x_1 \\ x_1' \end{pmatrix} \tag{B.4}$$

Such a matrix product can be evaluated by using Sylvester's theorem

$$\begin{pmatrix} A & B \\ C & D \end{pmatrix}^n = \frac{1}{\sin\phi} \begin{pmatrix} A\sin n\phi - \sin(n-1)\phi & B\sin n\phi \\ C\sin n\phi & D\sin n\phi - \sin(n-1)\phi \end{pmatrix} \tag{B.5}$$

where $\cos\phi = \frac{1}{2}(A + D)$ and

$$\sin\phi = \sqrt{1 - \frac{1}{4}(A+D)^2} \tag{B.6}$$

Clearly,

$$x_{n+1} = \{[A\sin n\phi - \sin(n-1)\phi]\, x_1 + B(\sin n\phi)x_1'\}/\sin\phi \tag{B.7}$$

If the angular factors remain real then x_{n+1} will oscillate as a function of n and the structure has periodic refocusing properties. The condition for ϕ to be real and $\sin\phi$ to remain oscillatory is $|\cos\phi| \leq 1$, which gives

$$\left|\frac{1}{2}(A+D)\right| \leq 1. \tag{B.8}$$

The condition that a ray remains paraxial and eventually retraces its pattern between the two mirrors, is the same as the stability condition for the equivalent biperiodic lens sequence. The ray matrix for the biperiodic lens sequence has the form

$$\begin{pmatrix} A & B \\ C & D \end{pmatrix} \equiv \begin{pmatrix} 1 - d/f_1 & 2d - d^2/f_1 \\ -1/f_1 - 1/f_2 + d/f_1 f_2 & 1 - d/f_1 - 2d/f_2 + d^2/f_1 f_2 \end{pmatrix} \tag{B.9}$$

Hence, the stability condition for the biperiodic lens sequence can be written as

$$0 \leq \left(1 - \frac{d}{2f_2}\right)\left(1 - \frac{d}{2f_1}\right) \leq 1 \tag{B.10}$$

where d is the spacing between mirrors. By simply substituting f_i with $R_i/2$, the stability condition for the equivalent spherical mirror resonator is obtained.

In the case of astigmatic mirrors, however, the above treatment has to be generalized by including a further dimension, which allows to account for the different radii of curvature of the mirror. Thus, for an astigmatic mirror multipass cell there are two independent reentrant equations that describe the circulation of beams within the cavity, and the stability condition must be established for two axes simultaneously. A single integer n is used to count the beam reflections from both mirrors, as if the spot patterns were combined on a single plane. Figure B.2 depicts the coordinate system adopted.

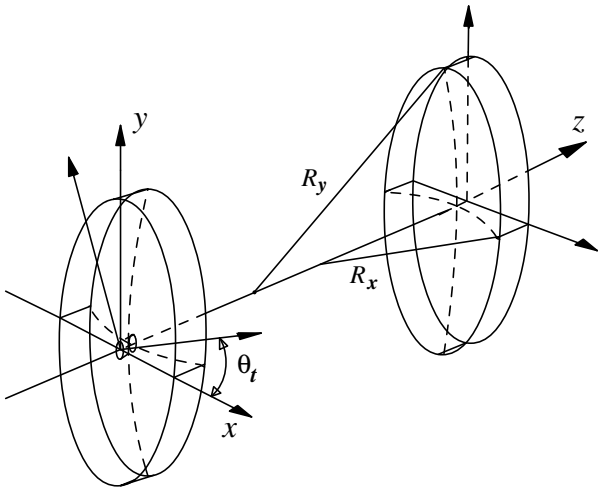

Figure B.2.: Coordinate system for the astigmatic mirror multipass cell. The z-axis passes through the mirror's center. The surface of the front mirror intersects this axis at $z = 0$, while the corresponding intersection of the back mirror surface occurs at $z = d$. The x and y axes are the mirror's principal axes, and they are orthogonal to the z axis. The mirror different radii of curvature are also indicated by R_x and R_y, respectively. θ_t depicts mirror rotations around the z-axis.

Here, the z axis still remains the optical axis. The front mirror is placed at $z = 0$, while the back mirror intersects the axis at $z = d$. The x and y axes represent the mirror's principal axes. In this 2D system, the $x-y$ coordinates of the n^{th} beam spot given by Eq. B.7 can be rewritten in the form

$$\begin{aligned} x_n &= X_0 \sin(n\phi_x), & y_n &= Y_0 \sin(n\phi_y), \\ \phi_x &= \arccos\left(1 - \tfrac{d}{R_x}\right), & \phi_y &= \arccos\left(1 - \tfrac{d}{R_y}\right) \end{aligned} \tag{B.11}$$

where X_0 and Y_0 define the size of the overall spot pattern and are proportional to the slope of the entering beam.

Thus the beam spots trace out a path on the mirrors that is sinusoidal in x and y but with different frequencies (hence a Lissajous spot pattern). For cells close to confocal spacing ($d \approx R$), one has $\phi_x \approx \frac{\pi}{2}$ and $\phi_y \approx \frac{\pi}{2}$. The reentrant condition is that the beam exits after N passes, *i.e.*, $x_N = y_N = 0$, which is satisfied for

$$N\phi_x = M_x\pi, \qquad N\phi_y = M_y\pi, \tag{B.12}$$

The integers N, M_x and M_y define the pattern of transits through the cell. A choice of N, cell base length, and mirror radii will result in a number of possible values for M_x, M_y. However, not all parameters satisfying Eq. B.12 are equally desirable in a practical absorption cell. Because of the finite size of the light spots, a minimum separation must be provided between the n^{th} spot that leaves the cell and the spot closest to it. Furthermore, spots corresponding to high n values should not be in the neighborhood of the coupling hole, otherwise they can cause interference fringes. In order to increase the number of possible cell configurations for a given set of mirrors, it is very useful to consider the rotation of the mirrors. This introduces an additional degree of freedom for the existing system.

The combined effects of rotation of nonidentical mirrors about the optical axis and of mirror tilts have been investigated by numerical calculations. The beam propagation through the cell was simulated implementing the ray 4×4 matrix method that is presented below [*McManus et al.*, 1995].

A propagating ray is represented by a column vector $\mathbf{Z}$, with components $[x, x', y, y']$, where x' and y' are the slopes in the x and y directions, respectively. The ray matrix for one cycle of the beam's propagation through the cell is constructed from free-space propagation and mirror reflection matrices

$$\mathbf{C} = \mathbf{R}(R_x, R_y) \cdot \mathbf{D}(d) \cdot \mathbf{R}(R_x, R_y) \cdot \mathbf{D}(d) \tag{B.13}$$

where

$$\mathbf{D}(d) = \begin{pmatrix} 1 & d & 0 & 0 \\ 0 & 1 & 0 & 0 \\ 0 & 0 & 1 & d \\ 0 & 0 & 0 & 1 \end{pmatrix} \tag{B.14}$$

is the free space propagation matrix and

$$\mathbf{R}(R_x, R_y) = \begin{pmatrix} 1 & 0 & 0 & 0 \\ -2/R_x & 1 & 0 & 0 \\ 0 & 0 & 1 & 0 \\ 0 & 0 & -2/R_y & 1 \end{pmatrix} \tag{B.15}$$

is the mirror reflection matrix.

When the mirror axes are rotated by an angle θ_t to the coordinate axes, the reflection matrix becomes

$$\mathbf{R}'(R_x, R_y) = \mathbf{T}(-\theta_t) \cdot \mathbf{R}(R_x, R_y) \cdot \mathbf{T}(\theta_t) \tag{B.16}$$

where

$$\mathbf{T}(\theta_t) = \begin{pmatrix} \cos\theta_t & 0 & \sin\theta_t & 0 \\ 0 & \cos\theta_t & 0 & \sin\theta_t \\ -\sin\theta_t & 0 & \cos\theta_t & 0 \\ 0 & -\sin\theta_t & 0 & \cos\theta_t \end{pmatrix} \tag{B.17}$$

is the rotation matrix that causes the mixing between the x and y components of the beam coordinates.

The coordinate of the beam spot after n cycles, $\mathbf{Z}_n$, is given by $\mathbf{C}^n\mathbf{Z}_0$, where $\mathbf{Z}_0$ is the initial vector with $x = 0$, $y = 0$. When the exit conditions are satisfied for n passes ($\mathbf{C}^n = 1$) the ray exits from the cell. The ray exit parameters can be obtained simply from the ray matrix $\mathbf{C}^{n-1}$:

$$\mathbf{C_{exit}} = \mathbf{D}(d) \cdot \mathbf{R}'(R_x, R_y) \cdot \mathbf{D}(d) \cdot \mathbf{C}^{n-1}. \tag{B.18}$$

Using the MPC parameters, such as the separation distance between mirrors (d), mirror radii (R_x, R_y), mirror rotation angles (θ_t) and the entrance beam slope (x'_0), the pattern of beam spots given in the New Focus user's manual [*New Focus, Inc.*, 1995] has been reproduced, demonstrating the validity of the method used. The entrance parameters used as input values for the program, as well as the results are given in Table B.1

From the elements of the resulting $\mathbf{C_{exit}}$ matrix, it was obvious that the multipass cell can be treated as a single astigmatic mirror placed in the position $z = 0$. The focal length of this hypothetical mirror is very close to that of the cell mirrors. The sign indicates that this mirror is convex. Therefore, as an optical element, the cell functions as if the beam was reflected off the hypothetical convex surface of the front mirror. Sending a slightly focalized beam into the cell will thus result in a nearly collimated output beam. This optical property of the multipass cell can be useful in a proper design of the focalizing optics, which couples the out-coming laser beam onto the detector. Furthermore, the numerical simulation allows to investigate different geometries. The main goal was to find an optimal solution that offers increased performance compared to the original New Focus mirror arrangement, which results in a highly rectangular spot-pattern (see Figure B.3).

Table B.1.: Multipass cell parameters used for simulation of ray propagation in the cavity. The values for the mirror radius were adopted from the technical drawing of the astigmatic mirrors purchased from Aerodyne Research, Inc. A HeNe laser that is co-aligned with the IR laser, was used to estimate the entrance angles of the beam.

Cell	Input Parameters							Calculated	
Configuration	d [cm]	R_x [cm]	R_y [cm]	x'_0	y'_0	θ_{front}	θ_{back}	f_x [cm]	f_y [cm]
NewFocus	56.0118	67.6656	74.0816	3.6°	0°	9°	26.76°	33.898	36.900
Current	〃	〃	〃	〃	〃	129°	146.76°	35.714	35.088

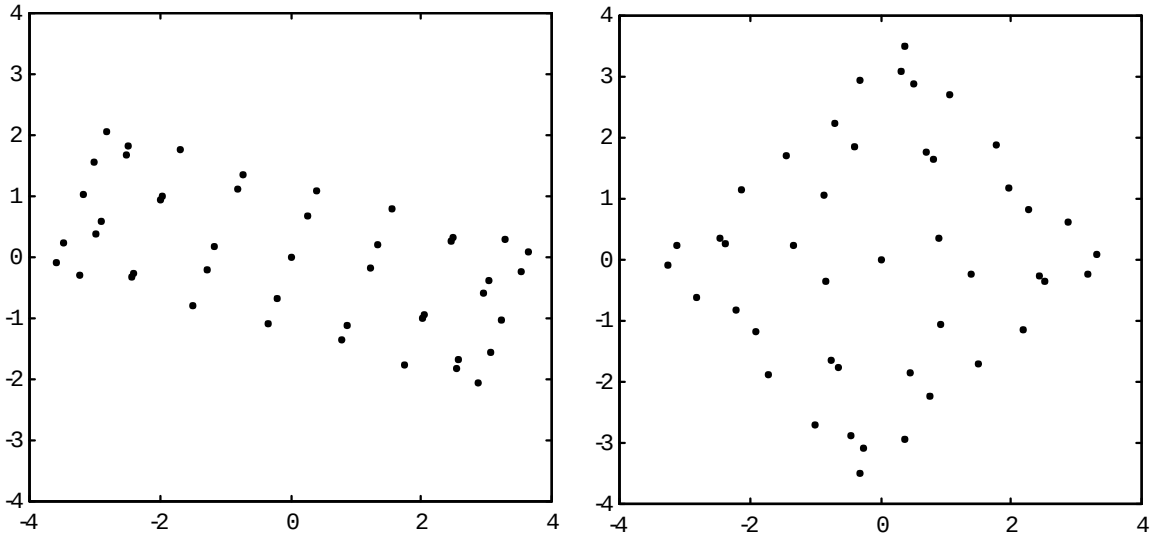

Figure B.3.: Comparison of the original New Focus spot pattern for the 90-pass configuration (left panel) with the spot pattern adopted in this work (right panel).

The final configuration differs from the original one only by the rotational angle of the mirrors. Hence, a nearly square pattern was obtained by rotating both mirrors 120° ccw from their positions.[1] The benefits of a square spot pattern have been discussed in Chapter 3 (page 30).

Interestingly, rotation of the mirrors affects the focal length of the overall optical system (see Table B.1) and, therefore, requires adjustment of the collimating optics. Considering the detector's small active area (1 mm^2), it should be stressed that an improperly focalized beam can cause strong optical fringes due to the light scattering from the detector windows and walls.

Finally, when both, the cell configuration and the collection optics was optimized, an optical fringe level of 1 to 5 $\times 10^{-4}$ absorption equivalent was reached.

[1] This solution was indicated by *Zahniser* [priv. comm.], too, as an optimal performance for the MPC.

C. Ozone Frequency Standards

Table C.1.: The list of $^{48}O_3$ absorption lines whose positions ν_0 [cm^{-1}] served as frequency standards for the absolute calibration. The individual spectral windows (SW) have the same notation as in Figure 2.2, page 23.

SW	ν_0	S	E_i	ν' - ν''	$J'K'_aK'_c$	$J''K''_aK''_c$
	1015.22410	1.14	1199.446	101-100	11 4 7	10 4 6
	1015.23740	1.11	1087.252	002-001	6 3 3	6 3 4
I	1015.30863	8.45	766.021	001-000	18 14 5	19 14 6
	1015.36840	2.22	1074.815	002-001	3 3 1	3 3 0
	1015.43933	13.7	678.877	001-000	22 12 11	23 12 12
	1015.59410	10.6	768.817	011-010	10 2 9	11 2 10
	1015.68002	5.11	717.225	100-000	27 10 18	28 11 17
	1034.90627[a]	7.79	856.662	011-010	14 5 10	13 5 9
	1034.96975[a]	1.96	1176.508	011-010	20 10 11	19 10 10
II	1035.23242	20.1	472.787	001-000	25 8 17	25 8 18
	1035.32954[a]	2.82	1100.803	011-010	19 9 10	18 9 9
	1035.51786	23.3	451.781	001-000	24 8 17	24 8 16
	1035.58975	60.7	425.568	001-000	16 10 7	16 10 6
	1042.17573[a]	8.75	986.061	011-010	27 0 27	26 0 26
	1042.25297[a]	4.69	1109.249	011-010	27 6 21	26 6 20
	1042.33518[a]	2.32	1268.039	011-010	30 8 23	29 8 22
III	1042.37232	1.39	405.162	100-000	23 6 18	24 7 17
	1042.57911	1.03	1032.562	001-000	19 17 2	18 17 1
	1042.67691[a]	8.66	983.629	011-010	26 2 25	25 2 24
	1042.80849[a]	7.06	1024.284	011-010	26 4 23	25 4 22
	1043.04019	6.71	171.502	001-000	19 2 17	19 2 18
	1043.05114[a]	7.94	1001.949	011-010	26 3 24	25 3 23
	1043.13245[a]	2.98	1220.673	011-010	30 7 24	29 7 23
IV	1043.40300	5.26	1097.118	011-010	28 5 24	27 5 23
	1043.59812[a]	7.51	1027.304	011-010	28 2 27	27 2 26
	1043.71573[a]	6.37	1077.104	011-010	31 0 31	30 0 30

The line intensities S are given in 10^{-22} cm/(molecule cm^{-2}) at 296 K. E_i represents the lower-state energy in cm^{-1}. ν' and ν'' are the upper- and the lower-state global quanta index, respectively. J, K_a and K_c define the upper- and lower-state local quanta. Data are taken from HITRAN'04 [*Rothman et al.*, 2005].

[a] Values taken from *Wagner et al.* [2002], with stated experimental uncertainties $\sim 1 \times 10^{-4}$ cm^{-1}.

D. Ozone Absorption Lines for Isotopic Ratio Measurements

Table D.1.: Spectral window I. Besides the measured absorption line positions $\nu_{0\,Meas}$ [cm^{-1}] the spectroscopic data-base values $\nu_{0\,Calc}$ [cm^{-1}] and the difference Δ [$10^{-4}\,cm^{-1}$] between the two are listed. The other notations are the same as in Table C.1.

Species	ν_0		Δ	S	E_i	ν' ν''	$J'K'_aK'_c$	$J''K''_aK''_c$
	$\nu_{0\,Calc.}$	$\nu_{0\,Meas.}$						
666	1015.1743	1015.17441	-1.1	$9.31{\cdot}10^{-23}$	1093.059	002-001	7 3 5	7 3 4
666	1015.2080	1015.20803	-0.3	$2.71{\cdot}10^{-23}$	1458.468	021-020	9 3 6	8 3 5
666	1015.2241	1015.22400	1.0	$1.14{\cdot}10^{-22}$	1199.446	101-100	11 4 7	10 4 6
666	1015.2374	1015.23741	-0.1	$1.11{\cdot}10^{-22}$	1087.252	002-001	6 3 3	6 3 4
666	1015.3003	1015.30029	0.1	$4.43{\cdot}10^{-23}$	1077.705	002-001	7 2 6	7 2 5
666	1015.4680	1015.46810	-1.0	$9.81{\cdot}10^{-23}$	1236.837	101-100	12 5 8	11 5 7
666	1015.5317	1015.53179	-0.5	$9.37{\cdot}10^{-24}$	330.497	100-000	23 222	24 5 19
666	1015.5585	1015.55849	-0.1	$8.07{\cdot}10^{-23}$	1062.712	002-001	4 2 2	4 2 3
666	1015.7008	1015.70087	-0.7	$7.30{\cdot}10^{-23}$	1046.026	002-001	1 1 1	1 1 0
666	1015.8115	1015.81172	-2.2	$1.45{\cdot}10^{-23}$	1591.734	101-100	21 1011	20 10 10
668	1015.2712	1015.27101	1.9	$6.27{\cdot}10^{-24}$	301.488	001-000	10 9 1	11 9 2
668	1015.2712	1015.27101	1.9	$6.27{\cdot}10^{-24}$	301.488	001-000	10 9 2	11 9 3
686	1015.1720	1015.17198	0.2	$4.60{\cdot}10^{-23}$	55.981	001-000	9 3 6	8 3 5
686	1015.2274	1015.22738	0.2	$3.33{\cdot}10^{-23}$	109.357	001-000	10 5 6	9 5 5
686	1015.4163	1015.41641	-1.1	$5.85{\cdot}10^{-23}$	29.962	001-000	9 0 9	8 0 8
686	1015.4599	1015.45999	-0.9	$5.27{\cdot}10^{-23}$	41.743	001-000	9 2 7	8 2 6
686	1015.7554	1015.75548	-0.8	$5.71{\cdot}10^{-23}$	33.926	001-000	9 1 8	8 1 7
667	1015.1593	1015.15953	-2.3	$9.13{\cdot}10^{-24}$	238.477	001-000	20 416	21 4 17
667	1015.1610	1015.16118	-1.8	$9.13{\cdot}10^{-24}$	238.451	001-000	20 417	21 4 18
667	1015.8009	1015.80095	-0.5	$1.16{\cdot}10^{-23}$	195.555	001-000	20 119	21 1 20
676	1015.7496	1015.74998	-3.8	$6.90{\cdot}10^{-24}$	85.612	001-000	8 4 5	9 4 6

The AFGL shorthand notation was adopted to identify the various isotopic species. Data are taken from HITRAN'04 [*Rothman et al.*, 2005].

Table D.2.: Spectral window II. The notations are the same as in Table D.1.

Species	ν_0		Δ	S	E_i	ν' ν''	$J'K'_aK'_c$	$J''K''_aK''_c$
	$\nu_{0\,Calc.}$	$\nu_{0\,Meas.}$						
666	1034.8965	1034.89666	-1.6	$4.39{\cdot}10^{-23}$	1755.385	002-001	34 9 25	33 9 24
666	1034.9698	1034.96973	0.7	$1.96{\cdot}10^{-22}$	1176.508	011-010	20 10 11	19 10 10
666	1035.3413	1035.34149	-1.9	$6.66{\cdot}10^{-23}$	1676.313	002-001	33 8 26	32 8 25
668	1035.2741	1035.27414	-0.4	$5.65{\cdot}10^{-23}$	48.066	001-000	10 2 9	9 2 8
668	1035.3204	1035.32042	-0.2	$2.43{\cdot}10^{-23}$	212.934	001-000	13 7 7	12 7 6
668	1035.3204	1035.32042	-0.2	$2.43{\cdot}10^{-23}$	212.934	001-000	13 7 6	12 7 5
668	1035.3455	1035.34538	1.2	$6.23{\cdot}10^{-23}$	35.560	001-000	10 0 10	9 0 9
667	1035.1055	1035.10521	2.9	$3.14{\cdot}10^{-24}$	17.338	001-000	3 2 2	3 2 1
667	1035.1116	1035.11132	2.8	$3.14{\cdot}10^{-24}$	17.335	001-000	3 2 1	3 2 2
676	1034.9605	1034.95985	6.5	$2.22{\cdot}10^{-24}$	473.666	001-000	21 10 11	20 10 10
676	1035.0165	1035.01644	0.6	$1.03{\cdot}10^{-23}$	135.976	001-000	15 4 11	14 4 10
676	1035.2683	1035.26844	-1.4	$8.72{\cdot}10^{-24}$	175.416	001-000	16 5 12	15 5 11

Table D.3.: Spectral window III. The notations are the same as in Table D.1.

Species	ν_0		Δ	S	E_i	ν' ν''	$J'K'_aK'_c$	$J''K''_aK''_c$
	$\nu_{0\,Calc.}$	$\nu_{0\,Meas.}$						
666	1042.36113	1042.36051	6.2	$3.08{\cdot}10^{-23}$	1516.862	001-000	27 20 7	26 20 6
666	1042.5507	1042.55065	0.5	$1.45{\cdot}10^{-23}$	1816.508	101-001	43 0 43	42 3 40
666	1042.55657	1042.55652	0.5	$4.56{\cdot}10^{-24}$	112.542	001-000	15 2 13	16 0 16
666	1042.6320	1042.63211	-1.1	$2.40{\cdot}10^{-23}$	1969.030	002-001	48 1 47	47 1 46
666	1042.69787	1042.69630	15.7	$1.46{\cdot}10^{-23}$	1734.531	001-000	31 21 10	30 21 9
666	1042.7081	1042.70816	-0.6	$7.30{\cdot}10^{-24}$	2213.872	002-001	49 8 42	48 8 41
666	1042.7162	1042.71636	-1.6	$3.30{\cdot}10^{-23}$	1887.715	002-001	45 3 43	44 3 42
666	1042.7273	1042.72748	-1.8	$1.32{\cdot}10^{-23}$	2089.835	002-001	47 7 41	46 7 40
668	1042.2051	1042.20545	-3.5	$1.22{\cdot}10^{-23}$	549.260	001-000	28 9 19	27 9 18
668	1042.2051	1042.20545	-3.5	$1.22{\cdot}10^{-23}$	549.260	001-000	28 9 20	27 9 19
668	1042.2308	1042.23073	0.7	$6.39{\cdot}10^{-23}$	196.582	001-000	23 0 23	22 0 22
668	1042.2648	1042.26472	0.8	$6.62{\cdot}10^{-23}$	165.265	001-000	20 2 18	19 2 17
668	1042.3435	1042.34455	-10.5	$1.50{\cdot}10^{-23}$	278.207	100-000	23 2 22	22 5 17
668	1042.5466	1042.54650	1.0	$6.12{\cdot}10^{-23}$	214.552	001-000	24 1 24	23 1 23
667	1042.4980	1042.49779	2.1	$1.18{\cdot}10^{-23}$	38.698	001-000	10 1 10	9 1 9
667	1042.5077	1042.50771	-0.1	$9.71{\cdot}10^{-24}$	64.719	001-000	10 3 8	9 3 7
667	1042.7026	1042.70241	1.9	$1.10{\cdot}10^{-23}$	49.126	001-000	10 2 9	9 2 8
676	1042.6703	1042.66811	21.9	$7.83{\cdot}10^{-24}$	326.109	001-000	28 2 27	27 2 26
676	1042.6944	1042.69217	22.3	$9.57{\cdot}10^{-24}$	268.482	001-000	25 2 23	24 2 22
676	1042.7322	1042.73013	20.7	$8.61{\cdot}10^{-24}$	301.640	001-000	27 1 26	26 1 25

Table D.4.: Spectral window IV. The notations are the same as in Table D.1.

Species	ν_0		Δ	S	E_i	ν' ν''	$J'K'_aK'_c$	$J''K''_aK''_c$
	ν_0 *Calc.*	ν_0 *Meas.*						
666	1042.99348	1042.99335	1.3	$5.82{\cdot}10^{-23}$	1357.494	001-000	25 19 6	24 19 5
666	1043.0567	1043.05701	-3.1	$2.92{\cdot}10^{-23}$	1914.440	002-001	45 4 42	44 4 41
666	1043.1573	1043.15693	3.7	$4.77{\cdot}10^{-23}$	1812.397	002-001	42 4 38	41 4 37
666	1043.1661	1043.16632	-2.2	$1.71{\cdot}10^{-23}$	2046.501	002-001	50 1 49	49 1 48
666	1043.2664	1043.26643	-0.3	$1.06{\cdot}10^{-23}$	1597.299	110-010	30 12 18	29 13 17
666	1043.3589	1043.35887	0.3	$1.19{\cdot}10^{-22}$	1427.017	011-010	34 9 26	33 9 25
666	1043.3626	1043.36271	-1.1	$2.86{\cdot}10^{-23}$	1923.182	002-001	46 2 44	45 2 43
666	1043.7029	1043.70280	1.0	$1.74{\cdot}10^{-23}$	2018.230	002-001	47 5 43	46 5 42
666	1043.7740	1043.77397	0.3	$3.03{\cdot}10^{-24}$	1994.442	101-001	40 9 32	39 10 29
668	1042.9546	1042.95484	-2.4	$4.00{\cdot}10^{-23}$	296.496	001-000	24 5 20	23 5 19
668	1043.0001	1042.99878	13.2	$2.42{\cdot}10^{-23}$	296.498	001-000	24 5 19	23 5 18
668	1043.0118	1043.01157	2.3	$2.30{\cdot}10^{-24}$	699.127	100-000	26 11 16	25 12 13
668	1043.0118	1043.01157	2.3	$2.30{\cdot}10^{-24}$	699.127	100-000	26 11 15	25 12 14
668	1043.0707	1043.07050	2.0	$5.81{\cdot}10^{-23}$	232.535	001-000	25 0 25	24 0 24
668	1043.2516	1043.25150	1.0	$2.82{\cdot}10^{-24}$	871.281	001-000	36 11 26	35 11 25
668	1043.2516	1043.25150	1.0	$2.82{\cdot}10^{-24}$	871.281	001-000	36 11 25	35 11 24
668	1043.3539	1043.35405	-1.5	$2.26{\cdot}10^{-23}$	429.791	001-000	27 7 20	26 7 19
668	1043.3539	1043.35405	-1.5	$2.26{\cdot}10^{-23}$	429.791	001-000	27 7 21	26 7 20
668	1043.4128	1043.41292	-1.2	$4.65{\cdot}10^{-23}$	268.886	001-000	24 4 21	23 4 20
668	1043.4404	1043.44042	-0.2	$5.73{\cdot}10^{-23}$	230.368	001-000	24 2 23	23 2 22
668	1043.5314	1043.53141	-0.1	$6.19{\cdot}10^{-23}$	198.571	001-000	22 2 20	21 2 19
668	1043.6796	1043.67957	0.3	$6.15{\cdot}10^{-23}$	208.032	001-000	23 1 22	22 1 21
668	1043.7914	1043.79114	2.6	$5.15{\cdot}10^{-23}$	271.700	001-000	27 1 27	26 1 26
667	1043.1610	1043.16072	2.8	$1.18{\cdot}10^{-23}$	40.859	001-000	10 1 9	9 1 8
667	1043.2061	1043.20618	-0.8	$1.04{\cdot}10^{-23}$	72.887	001-000	11 3 9	10 3 8
667	1043.2561	1043.25609	0.2	$3.88{\cdot}10^{-24}$	283.948	001-000	15 8 8	14 8 7
667	1043.2561	1043.25609	0.2	$3.88{\cdot}10^{-24}$	283.948	001-000	15 8 7	14 8 6
667	1043.2868	1043.28694	-1.4	$6.32{\cdot}10^{-24}$	175.383	001-000	13 6 7	12 6 6
667	1043.2868	1043.28694	-1.4	$6.32{\cdot}10^{-24}$	175.383	001-000	13 6 8	12 6 7
667	1043.7650	1043.76479	2.1	$1.32{\cdot}10^{-23}$	55.275	001-000	12 1 12	11 1 11
676	1043.1915	1043.18901	24.9	$5.16{\cdot}10^{-24}$	415.704	001-000	29 5 24	28 5 23
676	1043.2053	1043.20283	24.7	$7.22{\cdot}10^{-24}$	344.372	001-000	28 3 26	27 3 25
676	1043.6750	1043.67185	31.5	$3.66{\cdot}10^{-24}$	497.824	001-000	31 6 25	30 6 24
676	1043.7723	1043.76848	38.2	$1.74{\cdot}10^{-24}$	661.374	001-000	34 8 27	33 8 26

E. Identity Check of the Symmetric $^{49}O_3$ Isotopomer Line Positions

Comparison of measured ozone absorption spectra with the spectrum generated from the HITRAN'04 database, revealed a significant frequency shift for the $^{16}O^{17}O^{16}O$ isotopomer line positions in the frequency range of 1042–1044 cm^{-1}. Calibration of the frequency scale by highly accurate CO_2 laser II band transitions allowed a detailed investigation of this offset. The line positions determined from this survey are listed in Table E.1. The identity of these absorption lines has been verified employing the *isotopic labeling* method (see Figure E.1).

Table E.1.: Measured positions $\nu_{0\ Meas}$ [cm^{-1}] of the $^{16}O^{17}O^{16}O$-transitions.

SW	$\nu_{0\ Meas.}$	$\nu_{0\ Calc.}$ [a]	Δ
I	1015.74997	1015.7496	$-3.7\cdot10^{-4}$
II	1034.95983	1034.9605	$6.7\cdot10^{-4}$
	1035.01644	1035.0165	$6.0\cdot10^{-5}$
	1035.25520	1035.2551	$-1.0\cdot10^{-4}$
	1035.26842	1035.2683	$-1.2\cdot10^{-4}$
III	1042.66810	1042.6703	$2.2\cdot10^{-3}$
	1042.69217	1042.6944	$2.2\cdot10^{-3}$
	1042.73011	1042.7322	$2.1\cdot10^{-3}$
IV	1043.18903	1043.1915	$2.5\cdot10^{-3}$
	1043.20283	1043.2053	$2.5\cdot10^{-3}$
	1043.67181	1043.6750	$3.2\cdot10^{-3}$
V	1044.28703	1044.2897	$2.7\cdot10^{-3}$
	1044.30006	1044.3020	$1.9\cdot10^{-3}$
	1044.39257	1044.3956	$3.0\cdot10^{-3}$

[a] Values taken from HITRAN'04 database

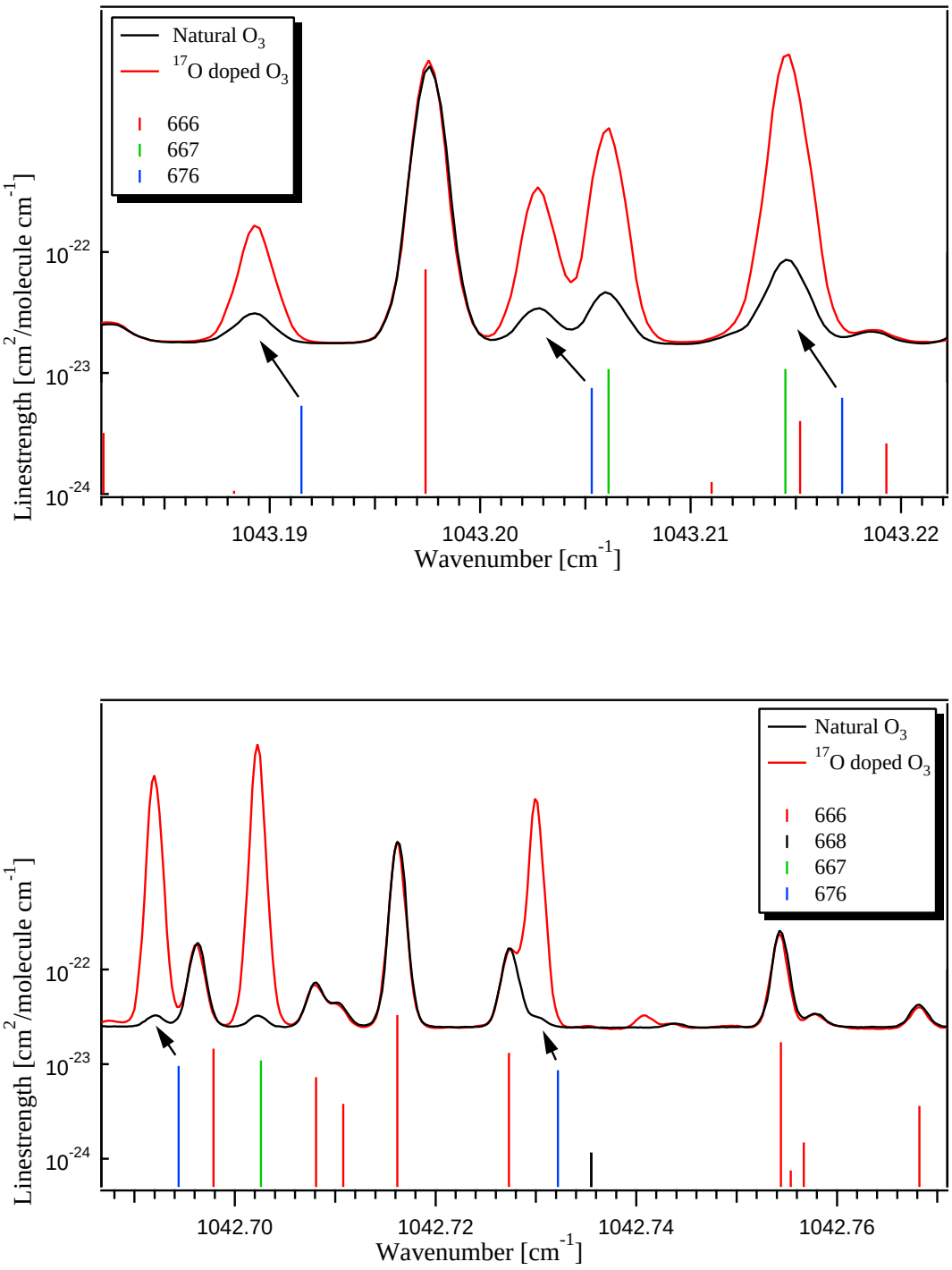

Figure E.1.: Overlapped absorption spectra of ozone formed from ^{17}O-doped molecular oxygen (red line), and ozone generated from natural O_2 (black line). Differences in the intensity of individual absorption features make the identification unambiguous. The arrows indicate the discrepancy between the measured $^{16}O^{17}O^{16}O$ isotopomer line positions and the database listed values depicted as stick plot.

F. Optical Density Ratios

Table F.1.: Spectroscopic results of the photolytic recycling experiment from **23.07.04** (Sample #5. in Table 4.4). The mean values of the isotopic abundance ratios of sample (ozone produced by photolytic recycling) and reference material (ozone obtained from heterogeneous wall formation in low pressure electric discharge) are given ($\bar{R}_{g/w}$) together with their relative errors (e_r). Every data point is an average of several absorption lines whose optical densities are calculated from 20 consecutive, individual scans. When there are temperature differences between sample and reference, the linestrengths are properly corrected. Isotope fractionation values ($\bar{E}_u$) are the weighted means of individual E_u values determined separately for each spectral window (SW). Their estimated standard deviations are given in parentheses.

	Ozone Isotopomers									
SW	666		668		686		667		676	
	$\bar{R}_{g/w}$	e_r (%)	$\bar{R}_{g/w}$	e_r (%)	$\bar{R}_{g/w}$	e_r (%)	$\bar{R}_{g/w}$	e_r (%)	$\bar{R}_{g/w}$	e_r (%)
I	-	-	-	-		-	-	-	-	-
II	0.8206	0.93	0.9928	0.39	-	-	0.9809	0.08	0.8318	0.15
III	0.8173	0.23	0.9946	0.26	-	-	0.9715	0.06	0.8222	0.19
IV	0.8365	0.31	1.0240	0.27	-	-	0.9983	0.20	0.8582	0.42
$\bar{E}_u$ (%):			**21.92 (31)**			-	**19.03 (23)**		**1.10 (26)**	

Table F.2.: Spectroscopic results of the photolytic recycling experiment from **29.07.04** (Sample #6. in Table 4.4). The notation is the same as in the Table 6.1.

	Ozone Isotopomers									
SW	666		668		686		667		676	
	$\bar{R}_{g/w}$	e_r (%)	$\bar{R}_{g/w}$	e_r (%)	$\bar{R}_{g/w}$	e_r (%)	$\bar{R}_{g/w}$	e_r (%)	$\bar{R}_{g/w}$	e_r (%)
I	0.9560	0.17	1.1748	0.50	0.9737	0.21	1.1281	0.52	0.9763	0.51
II	0.9671	0.38	1.1749	0.20	-	-	1.1550	0.34	0.9701	0.18
III	0.9624	0.17	1.1754	0.24	-	-	1.1498	0.10	0.9866	0.69
IV	0.9786	0.18	1.1950	0.16	-	-	1.1663	0.28	1.0007	0.26
$\bar{E}_u$ (%):			**22.10 (20)**		**1.85 (28)**		**19.29 (23)**		**1.71 (51)**	

Table F.3.: Spectroscopic results of the photolytic recycling experiment from **02.08.04** (Sample #7. in Table 4.4). The notation is the same as in the Table 6.1.

SW	Ozone Isotopomers									
	666		668		686		667		676	
	$\bar{R}_{g/w}$	e_r (%)	$\bar{R}_{g/w}$	e_r (%)	$\bar{R}_{g/w}$	e_r (%)	$\bar{R}_{g/w}$	e_r (%)	$\bar{R}_{g/w}$	e_r (%)
I	1.2262	0.16	1.5234	0.61	1.2420	0.36	1.4499	0.37	1.2688	0.48
II	1.2258	0.59	1.5147	0.28	-	-	1.4981	0.52	1.2686	0.39
III	1.2342	0.27	1.4878	0.32	-	-	1.4593	0.23	1.2510	0.42
IV	1.2420	0.17	1.5274	0.18	-	-	1.4878	0.22	1.2574	0.27
$\bar{E}_u$ (%):			**22.61 (67)**		**1.29 (40)**		**19.16 (60)**		**1.92 (58)**	

Table F.4.: Spectroscopic results of the high-pressure electric discharge experiment from **27.09.04** (Sample #2. in Table 4.8). The mean values of the isotopic abundance ratios of sample and reference material (ozone obtained from heterogeneous wall formation in low pressure electric discharge) are given ($\bar{R}_{g/w}$) together with their relative errors (e_r). Every data point is an average of several absorption lines whose optical densities are calculated from 20 consecutive, individual scans. When there are temperature differences between sample and reference, the linestrengths are properly corrected. Isotope fractionation values ($\bar{E}_u$) are the weighted means of individual E_u values determined separately for each spectral window (SW). Their estimated standard deviations are given in parentheses.

SW	Ozone Isotopomers									
	666		668		686		667		676	
	$\bar{R}_{g/w}$	e_r (%)	$\bar{R}_{g/w}$	e_r (%)	$\bar{R}_{g/w}$	e_r (%)	$\bar{R}_{g/w}$	e_r (%)	$\bar{R}_{g/w}$	e_r (%)
I	1.2438	0.21	1.5537	1.09	1.3085	0.19	1.4796	1.09	1.2951	0.47
III	1.3004	0.23	1.6233	0.35	-	-	1.5579	0.31	1.3307	0.27
IV	1.2903	0.22	1.6156	0.32	-	-	1.5539	0.46	1.3229	0.19
$\bar{E}_u$ (%):			**25.03 (34)**		**5.21 (30)**		**19.94 (36)**		**2.71 (44)**	

Table F.5.: Spectroscopic results of the high-pressure electric discharge experiment from **30.09.04** (Sample #3. in Table 4.8). The notation is the same as in the Table F.7.

SW	Ozone Isotopomers									
	666		668		686		667		676	
	$\bar{R}_{g/w}$	e_r (%)	$\bar{R}_{g/w}$	e_r (%)	$\bar{R}_{g/w}$	e_r (%)	$\bar{R}_{g/w}$	e_r (%)	$\bar{R}_{g/w}$	e_r (%)
I	1.1110	0.32	1.3872	1.23	1.1765	0.28	1.3356	1.23	1.1604	1.23
III	1.1267	0.22	1.3956	0.26	-	-	1.3503	0.34	1.1645	0.24
IV	1.1270	0.19	1.4049	0.15	-	-	1.3453	0.31	1.1486	0.64
$\bar{E}_u$ (%):			**24.39 (27)**		**5.89 (45)**		**19.61 (32)**		**3.15 (44)**	

Table F.6.: Spectroscopic results of the high-pressure electric discharge experiment from **12.11.04** (Sample #4. in Table 4.8). The notation is the same as in the Table F.7.

SW	Ozone Isotopomers									
	666		668		686		667		676	
	$\bar{R}_{g/w}$	e_r (%)	$\bar{R}_{g/w}$	e_r (%)	$\bar{R}_{g/w}$	e_r (%)	$\bar{R}_{g/w}$	e_r (%)	$\bar{R}_{g/w}$	e_r (%)
I	0.9603	0.12	1.2051	1.23	1.0067	0.33	1.1523	1.23	0.9975	1.23
	0.9887	0.17	1.2307	1.23	1.0364	0.25	1.1875	1.23	1.0269	1.23
III	0.9665	0.22	1.2053	0.20	-	-	1.1606	0.13	0.9894	0.13
IV	0.9781	0.18	1.2211	0.15	-	-	1.1749	0.12	1.0079	0.37
$\bar{E}_u$ **(%):**			**24.80 (22)**		**4.83 (24)**		**20.11 (19)**		**2.63 (24)**	

Table F.7.: Spectroscopic results of the CO_2-O_3 isotopic exchange experiment. The mean values of the isotopic abundance ratios of sample and reference material are given ($\bar{R}_{g/w}$) together with their relative errors (e_r). Every data point is an average of several absorption lines whose optical densities are calculated from 20 consecutive, individual scans. When there are temperature differences between sample and reference, the linestrengths are properly corrected. Isotope fractionation values ($\bar{E}_u$) are the weighted means of individual E_u values determined separately for each spectral window (SW). Their estimated standard deviations are given in parentheses.

SW	Ozone Isotopomers									
	666		668		686		667		676	
	$\bar{R}_{g/w}$	e_r (%)	$\bar{R}_{g/w}$	e_r (%)	$\bar{R}_{g/w}$	e_r (%)	$\bar{R}_{g/w}$	e_r (%)	$\bar{R}_{g/w}$	e_r (%)
I	0.7337	0.11	0.8792	0.57	0.7340	0.12	0.8602	0.20	0.7402	1.58
III	0.7328	0.25	0.8748	0.06	-	-	0.8572	0.11	0.7445	0.11
IV	0.7372	0.15	0.8796	0.19	-	-	0.8622	0.10	0.7528	0.16
$\bar{E}_u$ (%):			**19.38 (20)**		**0.05 (16)**		**17.04 (15)**		**1.89 (20)**	

Bibliography

Abbas, M. M., J. Guo, B. Carli, F. Mencaraglia, M. Carlotti, and I. G. Nolt (1987), Heavy ozone distribution in the stratosphere from far-infrared observation, *J. Geophys. Res.*, **92**(D11), 13,231–13,239. 1.2.1

Alexander, C. M. O., and L. R. Nittler (1999), The galactic evolution of Si, Ti, and O isotopic ratios, *Astrophys. J.*, **519**(1), 222–235. 1.1

Allan, M., K. R. Asmis, D. B. Popović, M. Stepanović, N. J. Mason, and J. A. Davies (1996), Production of vibrationally autodetaching O_2^- in low-energy electron impact on ozone, *J. Phys. B: At. Mol. Opt. Phys.*, **29**, 3487–3495. 4.2.1, 4.2.4

Anderson, S. M., F. S. Klein, and F. Kaufman (1985), Kinetics of the isotope exchange reaction of ^{18}O with NO and O_2 at 298 K, *J. Chem. Phys.*, **83**(4), 1648–1656. *g*

Anderson, S. M., J. Morton, and K. Mauersberger (1989), Laboratory measurements of ozone isotopomers by tunable diode laser absorption spectroscopy, *Chem. Phys. Lett.*, **156**(2,3), 175–180. 4.3, 6.1, 7

Anderson, S. M., D. Hülsebusch, and K. Mauersberger (1997), Surprising rate coefficients for four isotopic variants of $O + O_2 + M$, *J. Chem. Phys.*, **107**(14), 5385–5392. 1.2.2, *b*, 6.1

Avetisov, V. G., A. I. Nadezhdinskii, A. N. Khusnutdinov, and M. V. Zyrianov (1993), Frequency-scale precision in diode laser spectroscopy, *J. Quant. Spectrosc. Radiat. Transfer*, **49**(4), 417–422. 3.3.3

Babikov, D., B. K. Kendrick, R. B. Walker, R. T. Pack, P. Fleurat-Lesard, and R. Schinke (2003a), Metastable states of ozone calculated on an accurate potential energy surface, *J. Chem. Phys.*, **118**(14), 6298–6308. 1.2.3

Babikov, D., B. K. Kendrick, R. B. Walker, R. T. Pack, P. Fleurat-Lesard, and R. Schinke (2003b), Formation of ozone: Metastable states and anomalous isotope effect, *J. Chem. Phys.*, **119**(5), 2577–2589. 1.2.3, 1.2, 1.2.3

Bacis, R., A. J. Bouvier, and J. M. Flaud (1998), The ozone molecule: Electronic spectroscopy, *Spectrochimica Acta*, **A 54**, 17–34. 2.1

Bahou, M., L. Schriver-Mazzuoli, C. Camy-Peyret, and A. Schriver (1997), Photolysis of ozone at 693 nm in solid oxygen. Isotopic effects in ozone reformation, *Chem. Phys. Lett.*, **273**, 31–36. 1

Bains-Sahota, S. K., and M. H. Thiemens (1987), Mass-independent oxygen isotopic fractionation in a microwave plasma, *J. Phys. Chem.*, **91**, 4370–4374. 1.2.2, 4.2.4.1, 4.2.4.2

Baker, T. A., and G. I. Gellene (2002), Classical and quasi-classical trajectory calculations of isotope exchange and ozone formation proceeding through O + O_2 collision complexes, *J. Chem. Phys.*, **117**(16), 7603–7613. 1.2.3

Bates, D. R. (1986), Heavy ozone in the stratosphere, *Geophys. Res. Lett.*, **13**(7), 664–666. 1.2.3

Bates, D. R. (1988), Suggested explanation of heavy ozone, *Geophys. Res. Lett.*, **15**(1), 13–16. 1.2.3

Bates, D. R. (1990), Isotopic fractionation in the formation of ozone and of carbon dioxide, *J. Chem. Phys.*, **93**(12), 8739–8744. 1.2.3

Bhattacharya, S. K., and M. H. Thiemens (1988), Isotopic fractionation in ozone decomposition, *Geophys. Res. Lett.*, **15**(1), 9–12. 1.2.2

Blake, A. J., S. T. Gibson, and D. G. McCoy (1984), Photodissociation of $^{16}O^{18}O$ in the atmosphere, *J. Geophys. Res.*, **89**, 7277–7284. 1.2.1

Bradley, L. C., K. L. Soohoo, and C. Freed (1986), Absolute frequencies of lasing transitions in nine CO_2 isotopic species, *IEEE J. Quant. Electr.*, **QE-22**(2), 234–267. A, *a*

Braunstein, M., P. J. Hay, R. L. Martin, and R. T. Pack (1991), The lowest excited $^1A_2$ and $^1B_1$ states of ozone: Two conical intersections and their impact on photodissociation, *J. Chem. Phys.*, **95**(11), 8239–8247. 4.2.1

Brenninkmeijer, C. A. M., C. Janssen, J. Kaiser, T. Röckmann, T. S. Rhee, and S. S. Assonov (2003), Isotope effects in the chemistry of atmospheric trace compounds, *Chem. Rev.*, **103**, 5125–5161. 4, 6.2

Burbidge, E. M., G. R. Burbidge, W. A. Fowler, and F. Hoyle (1957), Synthesis of the elements in stars, *Rev. Mod. Phys.*, **29**(4), 547–650. 1.1

Chakraborty, S., and S. K. Bhattacharya (2003), Oxygen isotopic fractionation during UV and visible light photodissociation of ozone, *J. Chem. Phys.*, **118**(5), 2164–2172. 1.3, 4.2.3, *b*

Cicerone, R. J., and J. L. McCrumb (1980), Photodissociation of isotopically heavy O_2 as a source of atmospheric O_3, *Geophys. Res. Lett.*, **7**(4), 251–254. 1.2.1, 1.2.1

Claveau, C., J.-L. Teffo, D. Hurtmans, A. Valentin, and R. R. Gamache (1999), Line positions and absolute intensities in the laser bands of carbon-12 oxygen-17 isotopic species of carbon dioxide, *J. Molec. Spectrosc.*, **193**, 15–32. A, *a*

Clayton, R. N. (1993), Oxygen isotopes in meteorites, *Annu. Rev. Earth Planet. Sci.*, **21**, 115–149. 1.1

Davis, C. C. (1996), *Lasers and Electro-Optics. Fundamentals and Engineering*, Cambridge University Press. 2.4.1, 1

De Laeter, J. R., J. K. Böhlke, P. De Biévre, H. Hidaka, H. S. Peiser, K. J. R. Rosman, and P. D. P. Taylor (2003), Atomic weights of the elements: Review 2000 (IUPAC Technical Report), *Pure Appl. Chem.*, **75**(6), 683–800. *a*

DeMore, W. B., S. P. Sander, D. M. Golden, R. F. Hampson, M. J. Kurylo, C. J. Howard, A. R. Ravishankara, C. E. Kolb, and M. J. Molina (1997), Chemical kinetics and photochemical data for use in stratospheric modeling, evaluation number 12, NASA Panel for data evaluation. *f*

Demtröder, W. (1996), *Laser Spectroscopy. Basic Concepts and Instrumentation*, 2^{nd} ed., Springer-Verlag, Heidelberg. 2, 1

El-Sherbiny, M., E. A. Ballik, J. Shewchun, B. K. Garside, and J. Reid (1979), High sensitivity point monitoring of ozone, and high resolution spectroscopy of the ν_3 band of ozone using tunable semiconductor diode laser, *Appl. Opt.*, **18**(8), 1198–1203. A

Flaud, J. M., and R. Bacis (1998), The ozone molecule: Infrared and microwave spectroscopy, *Spectrochimica Acta*, **A 54**, 3–16. 2.1, 5.2

Fleurat-Lessard, P., S. Y. Grebenshchikov, R. Siebert, R. Schinke, and N. Halberstadt (2003), Theoretical investigation of the temperature dependence of the O + O_2 exchange reaction, *J. Chem. Phys.*, **118**(2), 610–621. 1.2.3

Flöthmann, H., C. Beck, R. Schinke, C. Woywod, and W. Domcke (1997), Photodissociation of ozone in the chappuis band. II. Time-dependent wave-packet calculations and interpretation of diffuse vibrational structures, *J. Chem. Phys.*, **107**(18), 7296–7313. 2

Freed, C., L. C. Bradley, and R. G. O'Donnell (1980), Absolute frequencies of lasing transitions in seven CO_2 isotopic species, *IEEE J. Quant. Electr.*, **QE-16**(11), 1195–1980. A

Gamache, R. R., S. Kennedy, R. Hawkins, and L. S. Rothman (2000), Total internal partition sums for molecules in the terrestrial atmosphere, *J.Molec. Struct.*, **517-518**, 407–425. 5.2, 5.2

Gao, Y. Q., and R. A. Marcus (2001), Strange and unconventional isotope effects in ozone formation, *Science*, **293**, 259–263. 1.2.3, 1

Gao, Y. Q., and R. A. Marcus (2002), On the theory of the strange and unconventional isotopic effects in ozone formation, *J. Chem. Phys.*, **116**(1), 137–154. 1.2.3, 4.3

Gao, Y. Q., W. Chen, and R. A. Marcus (2002), A theoretical study of ozone isotopic effects using a modified *ab initio* potential energy surface, *J. Chem. Phys.*, **117**(4), 1536–1543. 1.2.3, 4.3, 6.1, 7

Gellene, G. I. (1996), An explanation for symmetry-induced isotopic fractionation in ozone, *Science*, **274**(5291), 1344–1346. 1.2.3

Goldman, A., F. J. Murcray, D. G. Murcray, J. J. Kosters, C. P. Rinsland, J. M. Flaud, C. Camy-Peyret, and A. Barbe (1989), Isotopic abundances of stratospheric ozone from balloon-born high-resolution infrared solar spectra, *J. Geophys. Res.*, **94**, 8467–8473. 1.2.1

Gonfiantini, R., S. Valkiers, P. D. P. Taylor, and P. D. Bièvre (1997), Adsorption in gas mass spectrometry II. Effects on the measurement of isotope amount ratios, *International Journal of Mass Spectrometry and Ion Processes*, **171**, 231–242. 4.1.2

Gross, A., and G. D. Billing (1997), Isotope effects on the rate constants for the processes $O_2 + O \rightarrow O + O_2$ and $O_2 + O + Ar \rightarrow O_3 + Ar$ on a modified ground-state potential energy surface for ozone, *Chem. Phys.*, **217**, 1–18. 1.2.3

Günther, J., B. Erbacher, D. Krankowsky, and K. Mauersberger (1999), Pressure dependence of two relative ozone formation rate coefficients, *Chem. Phys. Lett.*, **306**, 209–213. 1.2.2

Günther, J., D. Krankowsky, and K. Mauersberger (2000), Third-body dependence of rate coefficients for ozone formation in ^{16}O–^{18}O mixtures, *Chem. Phys. Lett.*, **324**, 31–36. 1.2.2, 1.2.3

Hathorn, B. C., and R. A. Marcus (1999), An intramolecular theory of the mass-independent isotope effect for ozone. I., *J. Chem. Phys.*, **111**(9), 4087–4100. 1.2.3, 6.1

Hathorn, B. C., and R. A. Marcus (2000), An intramolecular theory of the mass-independent isotope effect for ozone. II. Numerical implementation at low pressures using a loose transition state, *J. Chem. Phys.*, **113**(21), 9497–9509. 1.2.3

Hay, P. J., T. H. Dunning, and V. A. Goddard (1975), Configuration interaction studies of O_3 and O_3^+. Ground and excited states, *J. Chem. Phys.*, **62**(10), 3912–3924. 1

Heidenreich, J. E., and M. H. Thiemens (1986), A non-mass-dependent oxygen isotope effect in the production of ozone from molecular oxygen: The role of molecular symmetry in isotope chemistry, *J. Chem. Phys.*, **84**(4), 2129–2136. 1.2.2

Herriott, D., H. Kogelnik, and R. Kompfner (1964), Off-axis paths in spherical mirror interferometers, *Applied Optics*, **3**(4), 523–526. 3.1.2

Herzberg, G. (1991), *Molecular Spectra and Molecular Structure*, vol. **II**, Krieger Publishing Company, Florida. 2

Hippler, H., R. Rahn, and J. Troe (1990), Temperature and pressure dependence of ozone formation rates in the range 1–1000 bar and 90–370 K, *J. Chem. Phys.*, **93**(9), 6560–6569. 1.2.2

Horváth, M., L. Bilitzky, and J. Hütner (1985), *Ozone*, vol. **20**, Elsevier. 3.3.2.1, 4.2.4

Irion, F. W., M. R. Gunson, C. P. Rinsland, Y. L. Yung, M. C. Abrams, A. Y. Chang, and A. Goldman (1996), Heavy ozone enrichments from ATMOS infrared solar spectra, *Geophys. Res. Lett.*, **23**, 2377–2380. 1.2.1

Ivanov, M. V., S. Y. Grebenshchikov, and R. Schinke (2004), Intra- and intermolecular energy transfer in highly excited ozone complexes, *J. Chem. Phys.*, **120**(21), 10,015–10,024. 1.2.3

Janssen, C. (1999), Symmetriespezifische productstudie zur ozonbildung im Sauerstoffisotopensystem $^{16}O/^{18}O$, PhD Thesis, Ruprecht-Karls Universität, Heidelberg. 4.1.2, 4.2.4.1, 4.3, 4.7

Janssen, C. (2004), Investigation and assessment of an oxygen isotope anomaly, Habilitationsschrift, Ruprecht Karls Universität. 4.2

Janssen, C. (2005), Intramolecular isotope distribution in heavy ozone $^{16}O^{18}O^{16}O$ and $^{16}O^{16}O^{18}O$, *J. Geophys. Res.*, accepted. 7

Janssen, C., J. Guenther, and D. Krankowsky (1999), Relative formation rates of $^{50}O_3$ and $^{52}O_3$ in ^{16}O–^{18}O, *J. Chem. Phys.*, **111**(16), 7179–7182. 1.2.2, 1.2, 1.2.3, 1.3, 1, 4.3, 6.1, 6.1, 6.1, 7

Janssen, C., J. Guenther, K. Mauersberger, and D. Krankowsky (2001), Kinetic origin of the ozone isotope effect: a critical analysis of enrichments and rate coefficients, *Phys. Chem. Chem. Phys.*, **3**, 4718–4721. 6.1, 6.1, 6.1, 6.1, 7

Janssen, C., J. Guenther, D. Krankowsky, and K. Mauersberger (2003), Temperature dependence of ozone rate coefficients and isotopologue fractionation in ^{16}O - ^{18}O oxygen mixtures, *Chem. Phys. Lett.*, **367**, 34–38. 1.2.2, *d*, 4.3, 4.6, 6.1

Johnson, D. G., K. W. Jucks, W. A. Traub, and K. V. Chance (2000), Isotopic composition of stratospheric ozone, *J. Geophys. Res.*, **105**(D7), 9025–9031. 1.2.1

Johnston, J. C., and M. H. Thiemens (1997), The isotopic composition of tropospheric ozone in three environments, *J. Geophys. Res.-Atmospheres*, **102**(D21), 25,395–25,404. 1.2.1

Johnston, J. C., T. Röckmann, and C. A. M. Brenninkmeijer (2000), CO_2 + O(^1D) isotopic exchange: Laboratory and modeling, *J. Geophys. Res.*, **105**(D12), 15.213–15.229. 6.2

Kaye, J. A., and D. F. Strobel (1983), Enhancement of heavy ozone in the Earth's atmosphere?, *J. Geophys. Res.*, **88**(C13), 8447–8452. 1.2.1, 1.2.2

Kerstel, E. R. T., G. Gagliardi, L. Gianfrani, H. A. J. Meijer, R. van Trigt, and R. Ramaker (2002), Determination of the ^{2}H/^{1}H, ^{17}O/^{16}O, and ^{18}O/^{16}O isotope ratios in water by means of tunable diode laser spectroscopy at 1.39 μm, *Spectrochim. Acta*, **58**, 2389–2396. 2

Klees, G. (1994), Erste Messung zur Isotopie des troposphärischen Ozons, PhD Thesis, Ruprecht-Karls-Universität, Heidelberg. 4.2.2

Krankowsky, D., F. Bartecki, G. G. Klees, K. Mauersberger, K. Schellenbach, and J. Stehr (1995), Measurement of heavy isotope enrichment in tropospheric ozone, *Geophysical Research Letters*, **22**(13), 1713–1716. 1.2.1

Krankowsky, D., P. Lämmerzahl, and K. Mauersberger (2000), Isotopic measurements os stratospheric ozone, *Geophys. Res. Lett.*, **27**(17), 2593–2595. 1.2.1, 6.2

Krohn, S. (1998), Untersuchung des Ozonisotopieeffekts bei niedrigen Drücken, Diplomarbeit, Ruprecht-Karls-Universität, Heidelberg. 4.1.2, 4.2.4.1

Lämmerzahl, P., T. Röckmann, C. A. M. Brenninkmeijer, D. Krankowsky, and K. Mauersberger (2002), Oxygen isotope composition of stratospheric carbon dioxide, *Geophysical Research Letters*, **29**(12), doi:10.1029/2001GL014343. 6.2

Levene, H. B., J. C. Nieh, and J. J. Valentini (1987), Ozone photodissociation dynamics, *J. Chem. Phys.*, **87**(5), 2583–2593. 4.2.1

Macko, P., P. Veis, and G. Cernogora (2004), Study of oxygen atom recombination on a Pyrex surface at different wall temperatures by means of time-resolved actinometry in a double pulse discharge technique, *Plasma Sources Sci. Technol.*, **13**, 251–262. 4.2.4

Maki, A. G., C. C. Chou, K. M. Evenson, L. R. Zink, and J. T. Shy (1994), Improved molecular constants and frequencies for the CO_2 laser from new high-J regular and hot-band frequency measurements, *J. Molec. Spectrosc.*, **167**, 211–224. A

Mantz, A. W. (1995), A review of spectroscopic applications of tunable semiconductor lasers, *Spectrochim. Acta*, **51**, 2211–2236. 2

Mauersberger, K. (1981), Measurement of heavy ozone in the stratosphere, *Geophys. Res. Lett.*, **8**(8), 935–937. 1.2.1

Mauersberger, K. (1987), Ozone isotope measurements in the stratosphere, *Geophys. Res. Lett.*, **14**(1), 80–83. 1.2.1

Mauersberger, K., J. Morton, B. Schueler, J. Stehr, and S. M. Anderson (1993), Multi-isotope study of ozone: Implications for the heavy ozone anomaly, *Geophys. Res. Lett.*, **20**, 1031–1034. 1.2.2, 1.1

Mauersberger, K., B. Erbacher, D. Krankowsky, J. Günther, and R. Nickel (1999), Ozone isotope enrichment: isotopomer-specific rate coefficients, *Science*, **283**, 370–372. 1.2.2, 1.2, *a*

Mauersberger, K., D. Krankowsky, and C. Janssen (2003), Oxygen isotope processes and transfer reactions, *Space Sci. Rev.*, **106**, 265–279. 1.2

McManus, J. B., and P. L. Kebabian (1990), Narrow optical interference fringes for certain setup conditions in multipass absorption cells of the Herriott type, *Applied Optics*, **29**(7), 898–900. 3.3.2

McManus, J. B., P. L. Kebabian, and M. S. Zahniser (1995), Astigmatic mirror multipass absorption cells for long-path-length spectroscopy, *Applied Optics*, **34**(18), 3336–3339. B

McManus, J. B., M. S. Zahniser, D. D. Nelson, L. R. Williams, and C. E. Kolb (2002), Infrared laser spectrometer with balanced absorption for measurement of isotopic ratios of carbon gases, *Spectrochim. Acta*, **58**, 2465–2479. 2, 3.3.2

Meier, A., and J. Notholt (1996), Determination of the isotopic abundances of heavy O_3 as observed in arctic ground-based FTIR-spectra, *Geophys. Res. Lett.*, **23**, 551–554. 1.2.1, 7

Meijer, H. A. J., R. E. M. Neubert, and G. H. Visser (2000), Cross contamination in dual inlet isotope ratio mass spectrometers, *International Journal of Mass Spectrometry*, **198**, 45–61. 4.1.2

Morgan, J. E., and H. I. Schiff (1964), Diffusion coefficients of O and N atoms in inert gases, *Canadian Journal of Chemistry-Revue Canadienne De Chimie*, **42**(10), 2300. *h*

Morton, J., B. Schueler, and K. Mauersberger (1989), Oxygen fractionation of ozone isotopes $^{48}O_3$ through $^{54}O_3$, *Chem. Phys. Lett.*, **154**(2), 143–145. 1.2.2

Morton, J., J. Barnes, B. Schueler, and K. Mauersberger (1990), Laboratory studies of heavy ozone, *J. Geophys. Res.*, **95**(D1), 901–907. 1.2.2, 4.2.2, 4.2.3, 4.2.4.1, 4.2.4.2, *b*, 4.3, 4.6, 4.3, 6.1, 6.1

Müller, T., S. S. Xantheas, H. Dachsel, R. J. Harrison, J. Nieplocha, R. Shepard, G. S. Kedziora, and H. Lischka (1998), A systematic ab initio investigation of the open and ring structures of ozone, *Chem. Phys. Lett.*, **293**, 72–80. 1.2.3

New Focus, Inc. (1995), *Models 5611 and 5612 User's Manual. Multipass Cell*, New Focus Inc., Santa Clara, CA or on the company homepage: http://www.newfocus.com/Manuals/561X_ManuaL_RevC.pdf. 3.1.2, B

Omidvar, K., and J. E. Frederick (1987), Atmospheric odd oxygen production of ordinary and isotopic molecular oxygen, *Planet. Space Sci.*, **35**, 769–784. 1.2.1

Perri, M. J., A. L. V. Wyngarden, K. A. Boering, J. J. Lin, and Y. T. Lee (2003), Dynamics of the $O(^1D)$ + CO_2 oxygen isotope exchange reaction, *J. Chem. Phys.*, **119**(16), 8213–8216. 6.2

Richard, E. C., K. K. Kelly, R. H. Winkler, R. Wilson, T. L. Thompson, R. J. McLaughlin, A. L. Schmeltekopf, and A. F. Tuck (2002), A fast-response near-infrared tunable diode laser absorption spectrometer for in situ measurements of CH_4 in the upper troposphere and lower stratosphere, *Appl. Phys. B.*, **75**, 183–194. 3.3.2

Richet, P., Y. Bottinga, and M. Javoy (1977), A review of hydrogen, carbon, nitrogen, oxygen, sulphur and chlorine stable isotope fractionation among gaseous molecules, *Ann. Rev. Earth Planet. Sci.*, **5**, 65–110. 6.1

Rinsland, C. P., V. M. Devi, J. M. Flaud, C. Camy-Peyret, M. A. Smith, and G. M. Stokes (1985), Identification of ^{18}O-isotopic lines of ozone in infrared ground-based solar absorption spectra, *J. Geophys. Res.*, **90**(D6), 10,719–10,725. 1.2.1

Rinsland, C. P., J.-M. Flaud, A. Perrin, M. Birk, G. Wagner, A. Goldman, A. Barbe, M.-R. D. Backer-Barilly, S. N. Mikhailenko, V. G. Tyuterev, M. A. H. Smith, V. M. Devi, D. C. Benner, F. Schreier, K. V. Chance, J. Orphal, and T. M. Stephen (2003), Spectroscopic parameters for ozone and its isotopes: recent measurements, outstanding issues, and prospects for improvements to HITRAN, *J. Quant. Spectrosc. Radiat. Transfer*, **82**, 207–218. A

Rothman, L. S., D. Jacquemart, A. Barbe, D. C. Benner, M. Birk, L. R. Brown, M. R. Carleer, C. Chackerian, K. Chance, L. H. Couderth, V. Dana, V. M. Devi, J.-M. Flaud, R. R. Gamache, A. Goldman, J. M. Hartmann, K. W. Jucks, A. G. Maki, J.-Y. Mandin, S. T. Massie, J. Orphal, A. Perrin, C. P. Rinsland, M. A. H. Smith, J. Tennyson, R. N. Tolchenov, R. A. Toth, J. V. Auwera, P. Varanasi, and G. Wagner (2005), The HITRAN 2004 molecular spectroscopic database, *J. Quant. Spectrosc. Radiat. Transfer*, **xx**, submitted. *b*, ,

Schellenbach, K. (1995), Aufbau einer transportablen Messstation zur Untersuchung der Isotopenverteilung in troposphärischem Ozon, Diplomarbeit, Ruprecht-Karls-Universität, Heidelberg. 4.1.2

Schinke, R., and P. Fleurat-Lessard (2005), The effect of zero-point energy differences on the isotope dependence of the formation of ozone: A classical trajectory study, *J. Chem. Phys.*, **122**(9). 4.3, 6.1, 7

Schueler, B., J. Morton, and K. Mauersberger (1990), Measurements of isotopic abundances in collected ozone samples, *Geophys. Res. Lett.*, **17**, 1295–1298. 1.2.1

Sehested, J., O. J. Nielsen, H. Egsgaard, N. W. Larsen, T. Pedersen, and L. K. Christensen (1995), First direct kinetic study of isotopic enrichment of ozone, *J. Geophys. Res.*, **100**(D10), 20,979–20,982. 1.2.2

Shaheen, R. (2005), A new approach to study the CO_2 + O(^1D) isotope exchange mechanism, PhD Thesis, Ruprecht-Karls Universität, Heidelberg. 6.2

Sheppard, M. G., and R. B. Walker (1983), Wigner method studies of ozone photo-dissociation, *Journal of Chemical Physics*, **78**(12), 7191–7199. 6.2

Siebert, R., R. Schinke, and M. Bittererová (2001), Spectroscopy of ozone at the dissociation threshold: Quantum calculations of bound and resonance states on a new global potential energy surface, *Phys. Chem. Chem. Phys.*, **3**, 1795–1798. 1.2.3

Siebert, R., P. Fleurat-Lessard, R. Schinke, M. Bittererová, and S. C. Farantos (2002), The vibrational energies of ozone up to the dissociation threshold: Dynamics calculations on an accurate potential energy surface, *J. Chem. Phys.*, **116**(22), 9749–9767. 1.2.3

Slanger, T. G., L. E. Jusinski, G. Black, and G. E. Gadd (1988), A new laboratory source of ozone and its potential atmospheric implications, *Science*, **241**(4868), 945–950. 4.2.4

Tanaka, T., and Y. Morino (1970), Coriolis interaction and anharmonic potential function of ozone from the microwave spectra in the excited vibrational states, *J. Molec. Spectrosc.*, **33**, 538–551. 2.1

Teffo, J.-L., L. Daumont, C. Claveau, A. Valentin, S. A. Tashkun, and V. I. Perevalov (2002), Infrared spectra of the $^{16}O^{12}C^{17}O$ and $^{16}O^{12}C^{18}O$ species of carbon dioxide: The region 500–1500 cm−1, *J. Molec. Spectrosc.*, **213**, 145–152. A

Thiemens, M. H. (1999), Mass-independent isotope effects in planetary atmosphere and the early solar system, *Science*, **7283**, 341–345. 1.2

Thiemens, M. H., and J. E. Heidenreich (1983), The mass-independent fractionation of oxygen: a novel isotope effect and its possible cosmochemical implications, *Science*, **219**(4588), 1073–1075. 1.2.2

Thiemens, M. H., and T. Jackson (1987), Production of isotopically heavy ozone by ultraviolet light photolysis of O_2, *Geophys. Res. Lett.*, **14**(6), 624–627. 1.2.2

Thiemens, M. H., and T. Jackson (1988), New experimental evidence for the mechanism for production of isotopically heavy O_3, *Geophys. Res. Lett.*, **15**(7), 639–642. 1.2.2

Thiemens, M. H., and T. Jackson (1990), Pressure dependency for heavy isotope enhancement in ozone formation, *Geophys. Res. Lett.*, **17**(6), 717–719. 1.2.2, 4.2.4.2

Tyuterev, V. G., S. Tashkun, P. Jensen, A. Barbe, and T. Cours (1999), Determination of the effective ground state potential energy function of ozone from high-resolution infrared spectra, *J. Mol. Spectrosc.*, **198**, 57–76. 1.2.3

Uehara, K., K. Yamamoto, T. Kikugawa, and N. Yoshida (2001), Isotope analysis of environmental substances by a new laser-spectroscopic method utilizing different pathlengths, *Sensors and Actuators*, **B 74**, 173–178. 2

Uehara, K., K. Yamamoto, T. Kikugawa, S. Toyoda, K. Tsuji, and N. Yoshida (2003), Precise isotope abundance ratio measurement of nitrous oxide using diode lasers, *Sensors and Actuators*, **B 90**, 250–255. 2

Valentini, J. J. (1987), Mass-independent isotopic fractionation in nonadiabatic molecular collisions, *J. Chem. Phys.*, **86**(12), 6757–6765. 1.2.3, 6.1

Wagner, G., M. Birk, and F. Schreier (2002), Spectroscopic database for ozone in the fundamental spectral regions, *J. Geophys. Res.*, **107**(D22). *a*

Wasson, J. T. (2000), Oxygen-isotopic evolution of the solar nebula, *Rev. Geophys.*, **38**(4), 491–512. 1.1

Wen, J., and M. Thiemens (1991), Experimental and theoretical study of isotope effects on ozone decomposition, *J. Geophys. Res.*, **96**(D6), 10.911–10.921. 1.3, 4.2.3, *a*

Wen, J., and M. H. Thiemens (1990), An apparent new isotope effect in a molecular decomposition and implications for nature, *Chem. Phys. Lett.*, **172**(5), 416–420. 1.2.2

Wen, J., and M. H. Thiemens (1993), Multi-isotope study of the $O(^1D)$ + CO_2 exchange and stratospheric consequences, *J. Geophys. Res.*, **98**, 12.801–12,808. 6.2, 6.2, 7

Werle, P. (1996), Spectroscopic trace gas analysis using semiconductor diode lasers, *Spectrochim. Acta*, **52**, 805–822. 2

Werle, P. (1998), A review of recent advances in semiconductor laser based gas monitors, *Spectrochim. Acta*, **54**, 197–236. 2

Werle, P., K. Maurer, R. Kormann, R. Mücke, F. D'Amato, T. Lancia, and A. Popov (2002), Spectroscopic gas analyzers based on indium-phosphide, antimonide and lead-salt diode-lasers, *Spectrochim. Acta*, **58**, 2361–2372. 2

Weston, R. E. (1999), Anomalous or mass-independent isotope effects, *Chem. Rev.*, **99**, 115–2136. 1.2

Wolf, S., M. Bitter, D. Krankowsky, and K. Mauersberger (2000), Multi-isotope study of fractionation effects in the ozone formation process, *J. Chem. Phys.*, **113**(7), 2684–2686. *c*

Woosley, S. E., and A. Heger (2003), The evolution and explosion of massive stars, *Rev. Mod. Phys.*, **74**, 1015–1071. 1.1

Worsnop, D. R., D. D. Nelson, and M. S. Zahniser (1993), Chemical kinetic studies of atmospheric reactions using tunable diode laser spectroscopy, in *Optical Methods in Atmospheric Chemistry; Proceedings of the Meeting, Berlin, Germany, 1992*, pp. 18–33. 3.3.2

Woywod, C., M. Stengle, W. Domcke, H. Flöthmann, and R. Schinke (1997), Photodissociation of ozone in the chappuis band. I. Electronic structure calculations, *J. Chem. Phys.*, **107**(18), 7282–7295. 2

Xie, D., H. Guo, and K. A. Peterson (2000), Accurate *ab initio* near-equilibrium potential energy and dipole moment functions of the ground electronic state of ozone, *J. Chem. Phys.*, **112**(19), 8378–8386. 1.2.3

Yamamoto, K., and N. Yoshida (2002), High-precision isotopic ratio measurement system for methane ($^{12}CH_3D/^{12}CH_4$,$^{13}CH_4/^{12}CH_4$) by using near-infrared diode laser absorption spectroscopy, *Spectrochim. Acta*, **58**, 2699–2707. 2

Yamashita, K., K. Morokuma, F. Le Quéré, and C. Leforestier (1992), New ab initio potential surfaces and three-dimensional quantum dynamics for transition state spectroscopy in ozone photodissociation, *Chem. Phys. Lett.*, **191**(6), 515–520. 1.2.3

Young, E. D., A. Galy, and H. Nagahara (2002), Kinetic and equilibrium mass-dependent isotope fractionation laws in nature and their geochemical and cosmochemical significance, *Geochimica et Cosmochimica Acta*, **66**(6), 1095–1104. 2

Yung, Y. L., W. B. DeMore, and J. P. Pinto (1991), Isotopic exchange between carbon dioxide and ozone via $O(^1D)$ in the stratosphere, *Geophys. Res. Lett.*, **18**(1), 13–16. 6.2, 6.2

Acknowledgements

I would like to express my sincere gratitude and appreciation to my supervisor Dr. Christof Janssen for his guidance, continued interest and inspiration throughout the course of this work. A special thanks for the constructive criticism and the helpful discussions. To work with him was a true privilege, and I am enormously grateful for the immense support, the patience and for everything I learned from him. I am also very thankful for his friendship and for the excellent working environment.

There are many other people to whom I owe a debt of thanks for their support over the last three years:

Prof. Dr. Konrad Mauersberger for his willingness to take me into his research group and for the wonderful research opportunity at Heidelberg, the nicest city that I have ever seen. Further special thanks for his personal financial support that provided me the possibility to live in a pleasant environment during my stay. His personality was an invaluable guide for me.

Prof. Dr. Wolfgang Krätschmer for his enjoyable company at lunchtimes that gave me the occasion to greatly enrich my knowledge not only in physics, but in all the possible fields of life. He was an open encyclopedia for me. From the several stimulating discussions we had, I realized that sometimes the simple questions are the most difficult to answer. Furthermore, it was a nice experience that a good joke at the middle of the day can do miracles. Even though in his opinion all the Hungarians are coming from the Mars, we still could most of the time understand each other. Also a special thanks to his wife, Zsuzsanna who made possible to have my wife along with me. I am very grateful for this support.

Dr. Thomas Röckmann for his invitation to the interview and presenting me to my future supervisor. Furthermore, I sincerely acknowledge his motivating attitude and his firm support at a conference we participated.

Prof. Dr. Ulrich Platt for being my second referee.

I am also indebted to the support of the mechanic shop and the glassblowing team to build and realize all my wishes in the shortest time possible. This thesis could not have been done without their invaluable assistance and their highly professional work. Special thanks to Frank Kleinbongardt, Rainer Runck and Erich Borger. I am also thankful to our technician Joachim Janicke for his help through my research. For the very quick assistance in the scientific literature I am very grateful to our librarian Gernot Vogt.

During my stay in Heidelberg I met a number of people who created an enjoyable environment at the institute as well as in Germany. Thanks to all my colleagues: Marc Braß, Peter Franz and in particular thanks to Robina Shaheen for performing the IRMS measurements and providing the ozone sample from her CO_2 experiment.

Special thanks to Dmitry Strelnikov for the considerable time we spent together discussing about physics (and not only) beside a glass of beer or wine. I am also very grateful to Peter Budz, who brought me to many interesting places and gave me useful hints.

The Max-Planck-Gesellschaft is acknowledged for providing me a scholarship for the Ph.D. research. It was a valuable time and a great experience to study in Germany that I will never forget.

Last but not least, I want to express my deepest gratitude to my wife Judit for her encouragement, constant support, understanding and love that I received from her.

Finally, I am mostly grateful to my parents. Without their support and sacrifice I would not have reached this point.